THE UNIVERSITY of EDINBURGH

Edinburgh Research Explorer

Efficient Analytical Calculation of Non-line-of-sight Channel Impulse Response in Visible Light Communications

Citation for published version:
Chen, C, Basnayaka, D, Wu, X & Haas, H 2017, 'Efficient Analytical Calculation of Non-line-of-sight Channel Impulse Response in Visible Light Communications', *Journal of Lightwave Technology*. https://doi.org/10.1109/JLT.2017.2786459

Digital Object Identifier (DOI):
10.1109/JLT.2017.2786459

Link:
Link to publication record in Edinburgh Research Explorer

Document Version:
Peer reviewed version

Published In:
Journal of Lightwave Technology

General rights
Copyright for the publications made accessible via the Edinburgh Research Explorer is retained by the author(s) and / or other copyright owners and it is a condition of accessing these publications that users recognise and abide by the legal requirements associated with these rights.

Take down policy
The University of Edinburgh has made every reasonable effort to ensure that Edinburgh Research Explorer content complies with UK legislation. If you believe that the public display of this file breaches copyright please contact openaccess@ed.ac.uk providing details, and we will remove access to the work immediately and investigate your claim.

Download date: 25. Apr. 2024

Efficient Analytical Calculation of Non-Line-of-Sight Channel Impulse Response in Visible Light Communications

Cheng Chen, *Student Member, IEEE*, Dushyantha A. Basnayaka, *Member, IEEE*, Xiping Wu, *Member, IEEE*, and Harald Haas, *Senior Member, IEEE*

***Abstract*—This study provides an analytical method to calculate the non-line-of-sight (NLoS) channel impulse response (CIR) in visible light communication (VLC) systems based on intensity modulation and direct detection (IM/DD). In this method, the NLoS channel is decomposed into a number of components with different propagation categories. These propagation categories are defined according to the number of reflections and the reflective surfaces that the light undergoes. The CIR corresponding to each light propagation category is analysed, and the overall NLoS CIR is approximated by the combination of the calculated CIR components in different propagation categories. The proposed method poses the major advantage of offering accurate results with very low computational complexity. Typically, a NLoS CIR with a time resolution of 0.1 ns can be generated within a second in MATLAB. Furthermore, the derived analytical results could be used as an analytical tool for the VLC channel characterisation study in future research.**

***Index Terms*—Channel impulse response, computational complexity, non-line-of-sight channel (NLoS), visible light communications.**

I. Introduction

With the emergence of 'smart' devices and the increase in wireless Internet access demand, the existing radio frequency (RF) spectrum resources will no longer fulfil the requirement of the future wireless data traffic. In order to avoid the potential spectrum crisis, many technologies using higher frequency spectrum resources have been considered by researchers. Visible light communication (VLC) is one such technique. The main idea of VLC is to convert the existing light sources into wireless access points to provide wireless communication functionality [1]. Many experimental studies have demonstrated that single-link light-emitting diode (LED)-based VLC systems can achieve data rates in the scope of Gbps [2], [3]. In addition to the feature of high transmission capability, many unique characteristics of VLC, such as improved security, license-free spectrum, make it a promising technology for various future applications.

Many studies on indoor optical wireless have shown that the effects of a non-line-of-sight (NLoS) channel also plays an important role in VLC systems [4]. In RF communications (microwave, millimetre-wave), the NLoS paths are normally formed by the effects of specular reflections, diffractions by surrounding objects. Therefore, the channel impulse response (CIR) of the signal via these NLoS paths shows multiple 'spikes' with discrete delays. The strength of these 'spikes' is dominated by the transmitter-receiver separation, which can normally be characterised by a free-space path loss (FSPL)-based model [5]. In contrast, the NLoS channels in VLC systems are normally caused by diffused reflections due to the smaller wavelength of visible light. This phenomenon creates a countless number of reflection paths, and the corresponding CIR shows as a continuous waveform. The characteristics of this continuous CIR depends not only on transmitter-receiver separation, but also on many other parameters such as orientation and reflectivity. Consequently, a simple FSPL model is unable to characterise the NLoS channel.

Low-cost LEDs and photodiodes (PDs) are typically used in both wireless infrared (IR) communication systems and VLC systems. In addition, the signal propagation characteristics in wireless IR and VLC systems are similar as both systems use adjacent optical spectrum. Consequently, a number of methods developed for simulating wireless IR communication channels can be used for VLC studies [6], [7]. A widely used deterministic NLoS CIR calculation method has been proposed in [4]. In this method, a cuboid room with internal surfaces causing diffused reflections is considered. The internal surfaces are divided into a large number of small reflecting elements. With the given locations and orientations of the transmitter and receiver, an accurate CIR result can be obtained by calculating the interaction between each pair of elements. The main drawback of this approach is its extremely high computational complexity. It takes several days to calculate a CIR result for a small room considering up to 3rd order reflections with a moderate time resolution. In order to reduce the computation time, improved methods based on the DUSTIN algorithm [8] and the Monte Carlo simulation [9] have been proposed. Both methods reduce the computation time significantly. Especially for

Manuscript received August 26, 2016; revised June 27, 2017 and November 15, 2017; accepted December 2, 2017. This work was supported by the Engineering and Physical Sciences Research Council (EPSRC) under Grant EP/L020009/1: Towards Ultimate Convergence of All Networks (TOUCAN). The work of H. Haas was supported by EPSRC under Established Career Fellowship Grant EP/K008757/1. *(Corresponding author: Cheng Chen.)*

The authors are with the Li-Fi Research and Development Centre, Institute for Digital Communications, The University of Edinburgh, Edinburgh EH9 3JL, U.K. (e-mail: cheng.chen@ed.ac.uk; d.basnayaka@ed.ac.uk; xiping.wu@ed.ac.uk; h.haas@ed.ac.uk).

Color versions of one or more of the figures in this paper are available online at http://ieeexplore.ieee.org.

Digital Object Identifier 10.1109/JLT.2017.2786459

0733-8724 © 2017 IEEE. Personal use is permitted, but republication/redistribution requires IEEE permission.
See http://www.ieee.org/publications_standards/publications/rights/index.html for more information.

IEEE Proof

the Monte Carlo method, an accurate CIR result can be obtained within a period of several minutes. A physical model of the IR channel using a sphere environment approximation has been proposed in [10] to approximate the frequency response of NLoS channels. It has been pointed out in [11] that since a typical incoherent visible light source has a broad optical spectrum, the methods developed in wireless IR communications cannot be directly used in VLC channel calculation. The dependency on light wavelength is considered in the deterministic CIR calculation method for the CIR calculation in VLC [11]. User mobility is taken into account in [12]. VLC channel characterisations based on the commercial optical design software Zemax is considered in [13]. Most of the aforementioned studies of VLC channel modelling offer results for special configurations, where generalisations are not straightforward.

In some VLC studies, such as multiple-input multiple-output (MIMO) in VLC [14] or networked VLC [15], a large number of channel samples are required to evaluate the system performance. If the deterministic or Monte Carlo method is used to generate the channel with NLoS components, it would take a considerable amount of time over many years. The channel model considering only line-of-sight (LoS) propagation is widely used because the VLC channel is generally dominated by the LoS path and the calculation has a very low computational complexity. An analytical closed-form expression for a NLoS CIR with a ceiling-bounce model in a diffused IR link has been derived in [16]. Motivated by this approach, in this study, we extend the work in [16] and propose an analytical method to calculate the NLoS CIR for VLC links. The current paper is an extended version of the previous study in [17]. Firstly, we decompose the complicated NLoS channel into a number of components with less-complicated light propagation categories. These propagation categories are defined according to the number of reflections and the reflective surfaces that the light undergoes. Secondly, the analysis of the channel with each category is carried out, and the corresponding CIR analytical expressions are obtained. Finally, the overall CIR is approximated as a superposition of these CIRs for each category. It is shown in this paper that the proposed method provides an efficient tight approximation for NLoS VLC CIRs considering up to 2nd order reflections.

The remainder of this paper is arranged as follows. The analysis methodology presented in this study is introduced in Section II. A preliminary single reflection CIR calculation is introduced in Section III. The detailed analysis of the component NLoS CIRs and the corresponding analytical results are presented in Section IV. The final approximated overall NLoS CIR calculation is presented in Section V. In addition, the calculation accuracy and computation time is evaluated and compared with the state-of-the-art method in this section. Conclusions are drawn in Section VI.

II. Non-Line-of-Sight Channel Analysis Methodology

In this section, the methodology of the proposed approach to analyse the NLoS channel in typical indoor environments such as cuboid rooms is presented. Multi-path reflections caused by internal surfaces inflict major NLoS channel components. It is assumed that the room's internal surfaces cause diffused reflections with fixed reflectance. In addition, a transmitter and a receiver are defined with specified locations. In this study, we are interested in calculating the normalised optical CIR. In the CIR calculation, we consider the detected optical power at each time instant on the receiver PD detector with a unity optical power radiated from the transmitter optical source. Without loss of generality, the optical CIR is normalised by time. This metric has also been used in many other publications [4], [18]. Note that an incoherent light source is assumed to be used. Therefore, the power of the optical signals can be incoherently added in the CIR calculation as the phases of optical signals are uncorrelated.

For the convenience of analysis, the entire NLoS CIR can be decomposed into multiple components with respect to the number of reflections occurred as:

$$h_{\mathrm{NLoS}}(t) = \sum_{\mathrm{i}=1}^{\infty} h^{[\mathrm{i}]}(t), \tag{1}$$

where $h^{[\mathrm{i}]}(t)$ represents the component CIR with light undergoing exactly i reflections. Despite the decomposition according to the number of reflections, the complexity of each component is still too high to conduct tractable analysis. In order to further decrease the analytical complexity, each component CIR $h^{[i]}(t)$ is further decomposed according to the light propagation category. A number of major light propagation categories are considered in this study.

In the case of $h^{[1]}(t)$, there is only one propagation category: light travels from the transmitter to one of the four walls, and after the reflection it continues to propagate to the receiver, as shown in Fig. 1(a). This light propagation category is called the transmitter-to-wall-to-receiver (TWR). For the channel of this category, the signal only interacts with a single surface. Consequently, the relationship between the geometric characteristics and the time delay characteristics of the channel is tractable for analysis as demonstrated in [16]. In the case of $h^{[2]}(t)$, light propagation between different surfaces exists. The different combinations of these propagations between different surfaces lead to four light propagation categories as shown in Fig. 1(b), (c), (d) and (e). For example, in one of the categories, the emitted light from the transmitter propagates via the floor and ceiling and incidents to the receiver. For convenience, this category is called the transmitter-to-floor-to-ceiling-to-receiver (TFCR). Similarly, the other three categories are the transmitter-to-wall-to-ceiling-to-receiver (TWCR), the transmitter-to-wall-to-wall-to-receiver (TWWR) and the transmitter-to-floor-to-wall-to-receiver (TFWR) categories. The analytical complexity of these categories is higher than that of TWR as the CIR calculation of these categories requires integrations over two surfaces. However, it is demonstrated that via appropriate approximations and simplifications, analytical CIR expressions can be obtained for several dominant categories. The resulting expressions have one or two one-dimensional (1-D) integrations with finite limits. The channel categories due to higher order reflections can also be defined in a similar manner, but are omitted due to the exponential growth of analytical complexity as the order of

IEEE Proof

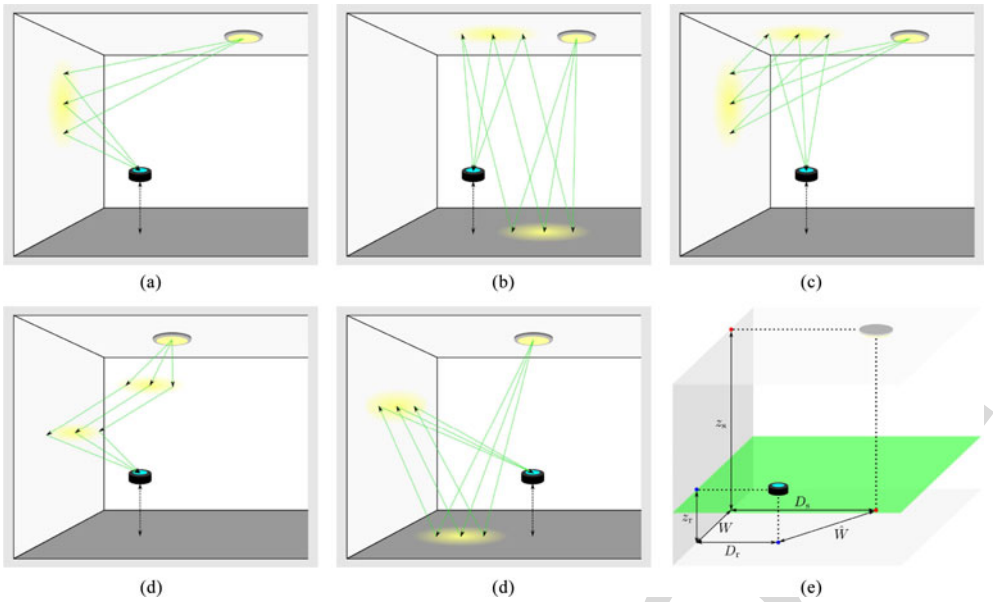

Fig. 1. (a) Light propagation in transmitter-to-wall-to-receiver case. (b) Light propagation in transmitter-to-floor-to-ceiling-to-receiver case. (c) Light propagation in transmitter-to-wall-to-ceiling-to-receiver case. (d) Light propagation in transmitter-to-wall-to-wall-to-receiver case. (e) Light propagation in transmitter-to-floor-to-wall-to-receiver case. (f) The notations of important geometric parameters.

reflections increases. Fortunately, it is shown in the final results that the omission of these higher order reflection components causes an acceptable loss in accuracy.

Ideally, the entire NLoS CIR should be the superposition of the CIR components considering all propagation categories. However, the channel with some categories is so complex that the corresponding expression is unavailable. Therefore, the superposition of the CIRs with part of the categories that dominate the NLoS channel is used to approximate the overall NLoS CIR. In this paper, the expressions for the CIR with TWR, TFCR and TWCR categories are derived and used to estimate the NLoS CIR. For the case of TFWR, the channel interacts with the wall and the floor. Therefore, the CIR is only perceivable when the link is next to one of the walls. In addition, the reflectivity of floor is typically low (0.2 to 0.4 [19]), which further decreases the significance of the channel of TFWR category. For the case of TWWR, the CIR is only perceivable when the link is next to one of the room corners. As long as the room is not small, this condition can be treated as a minor case. The power of the channels caused by high order reflections is expected to be low due to the significant path loss. Because of these reasons, the omission of the TFWR channel, the TWWR channel and other channels due to higher order reflections are expected to cause minor error in the NLoS CIR estimation. The analysis of the reflection and obstruction caused by other opaque objects, such as human bodies or furniture, is complicated, and many characteristics of these effects have not been investigated yet. Therefore, the impact of these issues are not considered.

III. Preliminary

In this section, a NLoS channel with a single diffused reflection by an infinite plane is considered. A closed-form expression for calculating the impulse response of this link in a special case is presented in [16]. However, the CIR analytical result for the general case will be frequently used in the CIR analysis of various categories in Section IV in this paper. For the convenience of the following analysis, we extend the work in [16] and present the expression for the general case here.

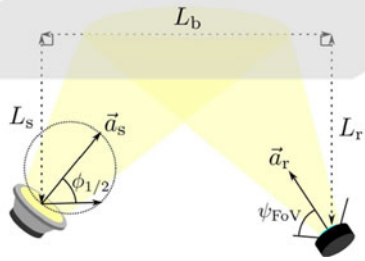

Fig. 2. The deployment of a single reflection light propagation channel.

Fig. 2 shows the setup for a single reflection channel. A light source with a Lambertian emission order of m and an orientation of $\vec{o}_s = [\tilde{x}_s, \tilde{y}_s, \tilde{z}_s]$ is L_s away from the plane. The Lambertian emission order m determines the radiation pattern of the light source, which is related to the light source half-power semiangle $\phi_{1/2}$ by $m = -1/\log_2(\cos(\phi_{1/2}))$. A receiving element with a physical area of A_r and an orientation of $\vec{o}_r = [\tilde{x}_r, \tilde{y}_r, \tilde{z}_r]$ is L_r away from the plane. Both the light source and the receiving element have the projection points on the plane. The distance between the two projection points is L_b. The effective reflectivity of the surface is ρ. The field of view (FoV) of the receiving element is ψ_{FoV}. The CIR for this single reflection link is concluded in the following proposition.

Proposition 1: With specified values for m, A_r, ρ, L_s, L_r, L_b, $\vec{o}_s$, $\vec{o}_r$ and ψ_{FoV}, the impulse response for a single reflection

channel can be calculated as:

$$h^{\vec{o}_s,\vec{o}_r}_{\{m,A_r,\rho,L_s,L_r,L_b,\psi_{\mathrm{FoV}}\}}(t) = \frac{\rho(m+1)L_sL_rA_r}{2\pi^2} \times \mathcal{U}\left(t-\frac{L_0}{c}\right)\int_0^{2\pi} \mathfrak{r}_\theta(t)\mathfrak{f}(\mathfrak{r}_\theta(t),\theta)\frac{\mathrm{d}\mathfrak{r}_\theta(t)}{\mathrm{d}t}\mathrm{d}\theta, \quad (2)$$

where

$$\mathfrak{f}(r,\theta) = \left(r\left(\tilde{x}_s\cos\theta+\tilde{y}_s\sin\theta\right)+\frac{L_sL_b\tilde{x}_s}{L_s+L_r}+L_s\tilde{z}_s\right)^m \times \left(r\left(\tilde{x}_r\cos\theta+\tilde{y}_r\sin\theta\right)-\frac{L_rL_b\tilde{x}_r}{L_s+L_r}+L_r\tilde{z}_r\right)\mathbf{1}_{\mathrm{FoV}} \times \left(r^2+\frac{2L_sL_br\cos\theta}{L_s+L_r}+L_s^2+\frac{L_s^2L_b^2}{(L_s+L_r)^2}\right)^{-\frac{m+3}{2}} \times \left(r^2-\frac{2L_rL_br\cos\theta}{L_s+L_r}+L_r^2+\frac{L_r^2L_b^2}{(L_s+L_r)^2}\right)^{-2}, \quad (3)$$

$$\mathfrak{r}_\theta(t) = \frac{ct\sqrt{\mathfrak{c}_\theta(t)}-\left(c^2t^2-L_0^2\right)(L_s-L_r)L_b\cos\theta}{2\left(c^2t^2-L_b^2\cos^2\theta\right)(L_s+L_r)}, \quad (4)$$

$$\frac{\mathrm{d}\mathfrak{r}_\theta(t)}{\mathrm{d}t} = \frac{2c^2tL_b\cos\theta\,(L_s-L_r)\left(L_b^2\cos^2\theta-L_0^2\right)}{2(L_s+L_r)\left(c^2t^2-L_b^2\cos^2\theta\right)^2} - \frac{c\left(c^2t^2+L_b^2\cos^2\theta\right)\sqrt{\mathfrak{c}_\theta(t)}}{2(L_s+L_r)\left(c^2t^2-L_b^2\cos^2\theta\right)^2} + \frac{c^3t^2\left(L_s-L_r\right)^2\left(c^2t^2-L_0^2\right)}{(L_s+L_r)\left(c^2t^2-L_b^2\cos^2\theta\right)\sqrt{\mathfrak{c}_\theta(t)}} + \frac{2c^3t^2L_sL_r\left(2c^2t^2-L_0^2-L_b^2\cos^2\theta\right)}{(L_s+L_r)\left(c^2t^2-L_b^2\cos^2\theta\right)\sqrt{\mathfrak{c}_\theta(t)}}, \quad (5)$$

$$L_0 = \sqrt{L_b^2+(L_s+L_r)^2}, \quad (6)$$

$$\mathfrak{c}_\theta(t) = 4L_sL_r\left(c^2t^2-L_b^2\cos^2\theta\right)\left(c^2t^2-L_0^2\right) + \left(L_s-L_r\right)^2\left(c^2t^2-L_0^2\right)^2. \quad (7)$$

Proof: The basic idea of this proposition is given as follows. Each light ray is reflected by a point on the reflection plane. The location of the point is defined by a polar coordinate system (r,θ). Firstly, the differential of the channel gain via each path is calculated. Then, the light signals via the paths with the same length arrive at the receiver at the same time. The accumulation of these signals form the response at a certain time delay. The expression (3) is proportional to the channel gain via each path. The expression (4) corresponds to the reflection points that lead to the paths with the same time delay. Expression (6) corresponds to the shortest reflection path. More details about the derivation of Proposition 1 is given in Appendix A.

In Proposition 1, c represents the speed of light, $\mathcal{U}(u)$ is the the unit step function, and $\mathbf{1}_{\mathrm{FoV}}$ is an indicator function, which guarantees only the signals propagating within the FoV of receiver and light source coverage contribute to the CIR. The indicator function $\mathbf{1}_{\mathrm{FoV}}$ equals 1 if it satisfies the following conditions:

$$\frac{r(\tilde{x}_r\cos\theta+\tilde{y}_r\sin\theta)-\frac{\tilde{x}_rL_rL_b}{L_s+L_r}+\tilde{z}_rL_r}{\sqrt{r^2-\frac{2L_rL_br\cos\theta}{L_s+L_r}+L_r^2+\frac{L_r^2L_b^2}{(L_s+L_r)^2}}} \geq \cos\psi_{\mathrm{FoV}}, \quad (8)$$

$$r(\tilde{x}_r\cos\theta+\tilde{y}_r\sin\theta)+\frac{\tilde{x}_sL_sL_b}{L_s+L_r}+\tilde{z}_sL_s \geq 0, \quad (9)$$

where (8) is the condition that the incident angle is within the receiver FoV and (9) is the condition that the radiant angle is within the coverage of the light source. Note that the orientation vectors $\vec{o}_s$ and $\vec{o}_r$ are defined based on a reflection plane orientation of $[0,0,-1]$ as shown in Fig. 16 in Appendix A.

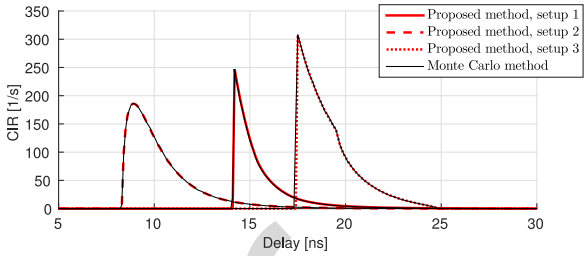

Fig. 3. Single reflection CIR results calculated using (2) and the Monte Carlo method. Configurations: $A_r = 1$ cm^2, $\rho = 0.65$. Setup 1: $\phi_{1/2} = 60°$, $\psi_{\mathrm{FoV}} = 90°$ $L_s = 2$ m, $L_r = 1$ m, $L_b = 3$ m, $\vec{o}_s = [1,0,0]$ and $\vec{o}_r = [-1,0,0]$. Setup 2: $\phi_{1/2} = 40°$, $\psi_{\mathrm{FoV}} = 90°$ $L_s = 1$ m, $L_r = 1$ m, $L_b = 1.5$ m, $\vec{o}_s = [0,0,1]$ and $\vec{o}_r = [0,1,0]$. Setup 3: $\phi_{1/2} = 60°$, $\psi_{\mathrm{FoV}} = 45°$ $L_s = 3$ m, $L_r = 2$ m, $L_b = 1.5$ m, $\vec{o}_s = [0,0,1]$ and $\vec{o}_r = [0,0,1]$.

A. Comparison With Monte Carlo Simulation Results

Fig. 3 shows three example CIRs calculated using the proposed method (2) and that using the Monte Carlo method [9] with various configurations. In the Monte-Carlo simulation, 5×10^7 iterations have been carried out for each result in this study, which is sufficient to obtain accurate results [9]. The size and the reflectance of the environment is defined in a way that is similar to the ideal condition specified for the analytical model. For example, in the single reflection channel model defined in this section, a single reflective plane with infinite size is assumed. In order to approximate this condition, a sufficiently large ceiling plane of size 50 m $\times$ 50 m is defined and the reflectivity of the remaining surfaces are set to zero. The agreement between the curves generated using (2) and that simulated using the Monte Carlo method proved the calculation accuracy of the proposed method with various link configurations.

B. Comparison With Experimental Results

In this subsection, an experiment is presented to validate the single reflection CIR analytical result. In this experiment, a LED torch (light source) and a positive-intrinsic-negative (PIN) diode detector (receiving element) are deployed next to a large board with light reflective paper causing diffused reflections, as shown in Fig. 4. Note that the measurement system used has a limited power budget to overcome the effects of noise at the detector. Therefore, we tried to adjust the experiment setup geometry to achieve a NLoS link with a higher channel gain. Both the light

IEEE Proof

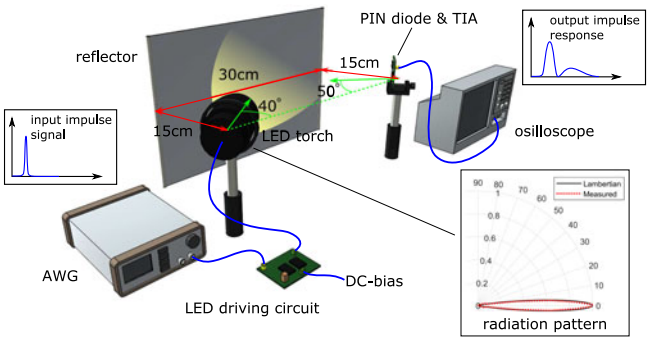

Fig. 4. Single reflection CIR calculation validation experiment setup.

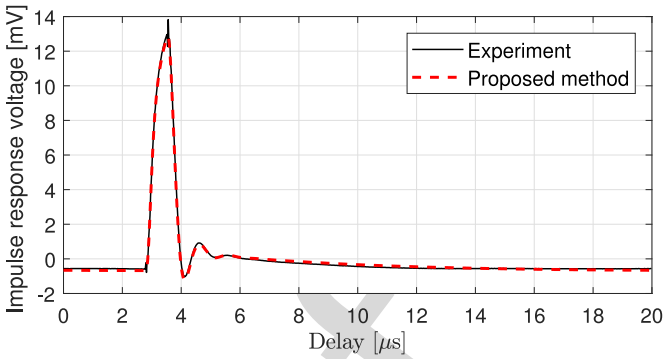

Fig. 5. Single reflection CIR results calculated using (2) and obtained in the experiment. The result calculated using (2) has been convolved with the impulse response of the measurement system.

source and the detector are positioned 15 cm away from the reflector ($L_s = L_s = 0.15$ m). The separation between the source and detector projections on the reflector is 30 cm ($L_b = 0.3$ m). The source and the detector are orientated to the same area on the reflector. Specifically, the angle between the source orientation vector $\vec{o}_s = [0.766, 0, 0.643]$ and the source / detector LoS path is 40°, as shown in Fig. 4. The angle between the detector orientation vector $\vec{o}_r = [-0.643, 0, 0.766]$ and the LoS path is 50°. The reflectance of the paper board used is 0.97 [20]. The used LED torch has a narrow beamwidth. The measured radiation pattern is presented in the bottom-right sub-plot in Fig. 4. A Lambertian pattern with a half-power semiangle of $\phi_{1/2} = 5.3°$ offers a good approximation to the measured pattern as shown in Fig. 4. Due to the use of an optical concentrator, the FoV of the PIN diode detector is decreased to 20°. Despite the fact that there is no obstruction between the source and the detector, there is no LoS transmission path in this setup due to the narrow beam of the source and the small FoV of the detector. In the experiment, an arbitrary waveform generator (AWG) is used to generate an analogue impulse signal with a pulse width of 800 ns. Via a LED driving circuit, the impulse signal is amplified and converted to a positive unipolar waveform. After the electrical-to-optical conversion via the light source and transmission through the NLoS channel, the optical signal is received by the detector and converted to a current signal. Afterwards, the current signal is amplified by a transimpedance amplifier (TIA) and the impulse response waveform is captured by an oscilloscope.

The experimental result of the single reflection channel is presented in Fig. 5. In order to mitigate the effect of noise, the oscilloscope is operated in the averaging mode. This means that the presented result is the average of 16384 detected responses. Note that the obtained experimental result also includes the impulse response of the measurement system (AWG, LED, PD, TIA). Therefore, when comparing the experimental result with the analytical result, the CIR calculated using (2) should be convolved with the impulse response of the measurement system. The measurement system impulse response can be obtained via the following process: 1) firstly, we conduct a LoS CIR measurement with the source and the detector facing each other. The separation between the source and the detector is 30 cm. The measured CIR result is denoted as $\hbar_{\mathrm{LoS}}(t)$. 2) then, we analytically calculate the LoS path loss G_{LoS}. 3) finally, the measurement system impulse response can be found as: $\hbar_{\mathrm{ms}}(t) = \hbar_{\mathrm{LoS}}(t)/G_{\mathrm{LoS}}$. The convolution of $\hbar_{\mathrm{ms}}(t)$ and the analytical result calculated using (2) is also shown in Fig. 5. It shows a close match with the experimental result, which validates the proposed method using (2). Also note that the presented results in Fig. 5 are the captured voltage signal in the AC coupling mode, where the DC component is removed from the captured signal. Therefore, the results have negative values.

IV. Detailed Analysis of Component Non-Line-of-Sight Channel Impulse Response

In this section, the CIR analysis for the channel with TWR, TFCR and TWCR categories are presented. A cuboid room with a size of $l_x \times l_y \times l_z$ is defined. The considered orientation of the light source in this study is towards the floor as this is the most common light deployment in practice. The considered orientation of the receiver PD detector is towards the ceiling. The reason for this is two-fold. Firstly, the proposed method aims at providing an efficient CIR calculation for other VLC research, and a detector orientation of directing upwards is used in many VLC studies. In addition, this configuration leads to CIR results with reasonable complexity, which is one of the research objective of this study. In practice, the fixed direction of PD detector can be achieved by using a mechanical design or by installing multiple PD detectors with different orientations on the receiver.

For the convenience of description, a number of parameters related to the positions of the transmitter and the receiver are defined. As shown in Fig. 1(f), the ceiling, the floor and one of the walls are used as references. z_s denotes the distance from the transmitter (ceiling) to the floor plane; z_r denotes the distance from the receiver to the floor plane; D_s denotes the distance from the transmitter to the wall plane; D_r denotes the distance from the receiver to the wall plane; the transmitter and the receiver have projections on the line where the floor plane and the wall plane intersect, and the distance between these two projection points is denoted as W; considering the projections of the transmitter and the receiver on the floor plane, the distance between these two projection points are denoted as $\hat{W}$. These parameters are also illustrated in Fig. 1(f).

IEEE Proof

TABLE I
DEFAULT CONFIGURATION OF THE SYSTEM PARAMETERS

Parameter	Symbol	Value
PD area / receiving area	A_{pd} / A_{r}	1 cm^2
Wall effective reflectance	ρ_{w}	0.65
Ceiling effective reflectance	ρ_{c}	0.8
Floor effective reflectance	ρ_{f}	0.3
Room height	z_{s}	3 m
Time delay step	Δt	0.1 ns

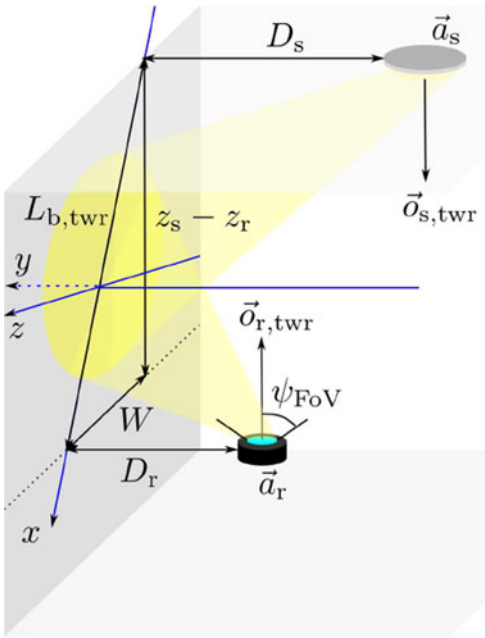

Fig. 6. Light propagation geometry in TWR category. Setup 1

The configurations of the parameters listed in Table I are used if they are not specified. Note that the selected reflectivity is based on the requirement on the reflectance of indoor internal surfaces, which is specified in [19].[1]

A. Transmitter-to-Wall-to-Receiver Channel Impulse Response (TWR)

The channel with TWR category undergoes a single reflection bounced by a wall plane, which can be treated as a special case single reflection channel as shown in Fig. 6. Therefore, the CIR of TWR category is a direct application of Proposition 1 and can be readily calculated using (2). Fig. 6 shows that the input values for L_s, L_r and L_b should be D_s, D_r and $L_{b,\mathrm{twr}} = \sqrt{W^2 + (z_s - z_r)^2}$, respectively. By comparing the geometry shown in Fig. 6 and that shown in Fig. 2, it can be found that the segment between the projections of the transmitter and the receiver is tilted relative to the floor plane. As described in Section III, the orientation vectors of the transmitter and the receiver is defined based on the Cartesian coordinate system with the x direction parallel to that segment. Therefore, this tilting leads to a transformation of the transmitter and receiver orientation vectors. Note that both the orientations of the transmitter and the receiver are parallel to the wall plane. In addition,

[1]Ceiling: 0.7 to 0.9, walls 0.5 to 0.8, floor: 0.2 to 0.4.

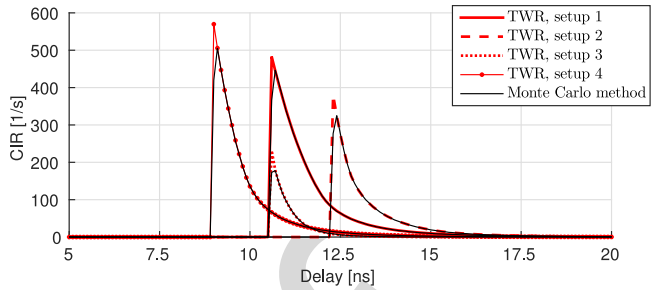

Fig. 7. NLoS CIR results with TWR category. Setup 1: $\phi_{1/2} = 60°$, $\psi_{\mathrm{FoV}} = 90°$, $D_s = 1$ m, $D_r = 1$ m, $W = 1$ m and $z_r = 0.75$ m. Compared to the configuration in setup 1, D_s, D_r, W are modified to 0.5, 2, 1.5 m in setup 2, $\phi_{1/2}$, ψ_{FoV} are modified to $40°$, $45°$ in setup 3, and z_r is modified to 0.75 m in setup 4.

the tilting of the orientations depends on the ratio between W and $z_s - z_r$. Consequently, the transformed orientation vectors should be:

$$\vec{o}_{s,\mathrm{twr}} = \left[\frac{z_s - z_r}{L_{b,\mathrm{twr}}}, \frac{W}{L_{b,\mathrm{twr}}}, 0\right], \tag{10}$$

$$\vec{o}_{r,\mathrm{twr}} = \left[-\frac{z_s - z_r}{L_{b,\mathrm{twr}}}, -\frac{W}{L_{b,\mathrm{twr}}}, 0\right]. \tag{11}$$

Therefore, the expression for the CIR with TWR category can be calculated as:

$$h^{[1]}_{\mathrm{twr}}(t) = \hbar^{\vec{o}_{s,\mathrm{twr}},\vec{o}_{r,\mathrm{twr}}}_{\{m,A_{\mathrm{pd}},\rho_w,D_s,D_r,L_{b,\mathrm{twr}},\psi_{\mathrm{FoV}}\}}(t), \tag{12}$$

where ρ_w denotes the reflectance of the wall and A_{pd} denotes the physical area of the receiver PD detector.

Fig. 7 shows a number of CIRs in the TWR category with different setups calculated using (12). The corresponding CIR results generated using the Monte Carlo method are also presented in Fig. 7. The agreement between the CIR results generated by different methods validates the CIR calculation expression in TWR category (12).

B. Transmitter-to-Floor-to-Ceiling-to-Receiver Channel Impulse Response (TFCR)

In the TFCR channel category, the light undergoes two reflections bounced by ceiling and floor, respectively. In order to find the CIR expression for this NLoS category, a point located at $\vec{a}_b$ on the ceiling is considered as shown in Fig. 8. For the convenience of calculation, the whole space is defined by a three-dimensional (3-D) cylinder coordinate system r-θ-z. The origin is defined at the point right below the receiver on the floor. Thus, the coordinates of the point $\vec{a}_b$ can be defined as $[r, \theta, z_s]$. Firstly, we treat point $\vec{a}_b$ as a 'detector' and consider a single reflection channel from the transmitter bounced by the floor to point $\vec{a}_b$, which is defined as transmitter-to-floor-to-ceiling point (TFC) channel. In this case, the 'detector' is facing the floor and has an infinitely small physical area of $\mathrm{d}A$. Intuitively, the differential of the TFC CIR can be calculated using (2) as:

$$\mathrm{d}h^{\vec{a}_b}_{\mathrm{tfc}}(t) = \hbar^{[0,0,1],[0,0,1]}_{\{m,\mathrm{d}A,\rho_f,z_s,z_s,\tilde{r},90°\}}(t), \tag{13}$$

where ρ_f denotes the reflectance of the floor and $\tilde{r}$ is the length of the segment between the projections of transmitter and receiver

IEEE Proof

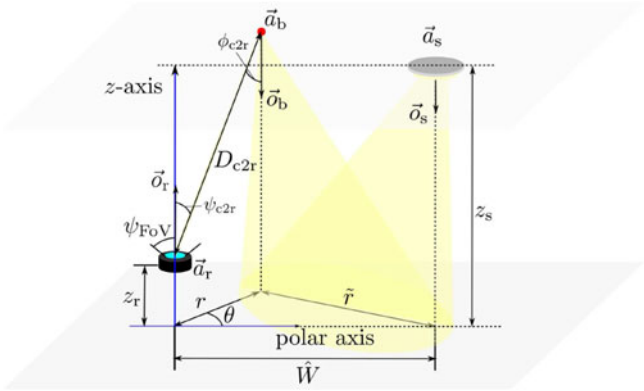

Fig. 8. Light propagation geometry in TFCR channel.

on the floor, which can be calculated using the law of Cosine as:

$$\tilde{r} = \sqrt{r^2 + \hat{W}^2 - 2r\hat{W}\cos\theta}. \tag{14}$$

the area differential $\mathrm{d}A$ can be converted to $r\mathrm{d}r\mathrm{d}\theta$ in a cylinder coordinate system. Assume that the reflectivity of the ceiling is ρ_c. After the light signal reaches point $\vec{a}_b$, ρ_c of the incident optical power is reflected and a fraction of the reflected power is incident to the receiver. In addition, the transmission from point $\vec{a}_b$ to the receiver leads to a further delay of $\tau_{c2r}^{\vec{a}_b}$. Therefore, the CIR from the transmitter bounced by the floor and ceiling point $\vec{a}_b$ to the receiver can be found as:

$$\mathrm{d}h_{\mathrm{tfcr}}^{\vec{a}_b}(t) = \rho_c G_{c2r}^{\vec{a}_b}\mathrm{d}h_{\mathrm{tfc}}^{\vec{a}_b}\left(t - \tau_{c2r}^{\vec{a}_b}\right), \tag{15}$$

where $G_{c2r}^{\vec{a}_b}$ corresponds to path loss of the transmission from point $\vec{a}_b$ to the receiver. In conjunction with the receiver position of $(0, 0, z_r)$, the path loss can be found as [21]:

$$G_{c2r}^{\vec{a}_b} = \frac{A_{\mathrm{pd}}\mathbf{1}_{\mathrm{FoV}}^{c2r}\cos\phi_{c2r}\cos\psi_{c2r}}{\pi D_{c2r}^2} = \frac{(z_s - z_r)^2 A_{\mathrm{pd}}\mathbf{1}_{\mathrm{FoV}}^{c2r}}{\pi D_{c2r}^4}, \tag{16}$$

where D_{c2r} is the Euclidean distance between point $\vec{a}_b$ and the receiver, and the indicator function $\mathbf{1}_{\mathrm{FoV}}^{c2r}$ determines whether the incident signal is within the FoV of the receiver. It is defined that $\mathbf{1}_{\mathrm{FoV}}^{c2r} = 1$, if the incident angle ψ_{c2r} to the receiver is smaller than the receiver FoV, which corresponds to the condition that $\cos\psi_{c2r} = (z_s - z_r)/D_{c2r} \geq \cos\psi_{\mathrm{FoV}}$. Otherwise, $\mathbf{1}_{\mathrm{FoV}}^{c2r} = 0$. With the defined coordinate system, the distance D_{c2r} can be calculated as $D_{c2r} = \sqrt{r^2 + (z_s - z_r)^2}$. Then, the delay can be calculated as $\tau_{c2r}^{\vec{a}_b} = D_{c2r}/c$. Note that (15) only accounts for the channel via point $\vec{a}_b$. In order to get the entire CIR for the TFCR category, the channels via all points on the ceiling should be considered. This leads to an integration over the whole ceiling plane. By inserting (13), (16) into (15) and carrying out the integration over the ceiling plane, the CIR for the TFCR category can be found as:

$$h_{\mathrm{tfcr}}^{[2]}(t) = \int_{-\pi}^{\pi}\int_{0}^{\infty}\frac{\rho_c(z_s - z_r)^2 A_{\mathrm{pd}}\mathbf{1}_{\mathrm{FoV}}^{c2r}}{\pi D_{c2r}^4} \times \hbar_{\{m,r\mathrm{d}r\mathrm{d}\theta,\rho_f,z_s,z_s,\tilde{r},90^\circ\}}^{[0,0,1],[0,0,1]}\left(t - \frac{D_{c2r}}{c}\right), \tag{17}$$

which can be directly calculated using the standard numerical method. However, the computation complexity is very high as it requires solving three numerical integrations.

In order to reduce the computational complexity of the CIR calculation, a simpler approximated expression can be used as a substitution of the exact expression with a minor loss in accuracy. In a special case of $\tilde{r} = 0$, expression (13) can be significantly simplified. It has been found that expression (13) can be approximated by this simplified spacial case expression with appropriate scaling as:

$$\begin{aligned}\mathrm{d}h_{\mathrm{tfc}}^{\vec{a}_b}(t) &\approx \mathcal{F}_{\mathrm{tfc}}\mathcal{U}\left(t - \frac{D_{\mathrm{tfc},\vec{a}_b}}{c}\right)\hbar_{\{m,r\mathrm{d}r\mathrm{d}\theta,\rho_f,z_s,z_s,0,90^\circ\}}^{[0,0,1],[0,0,1]}(t)\\ &= \frac{(m+1)r\mathrm{d}r\mathrm{d}\theta\rho_f z_s^{m+3}\mathcal{F}_{\mathrm{tfc}}}{\pi(c/2)^{m+5}t^{m+6}}\mathcal{U}\left(t - \frac{D_{\mathrm{tfc},\vec{a}_b}}{c}\right),\end{aligned} \tag{18}$$

where $D_{\mathrm{tfc},\vec{a}_b} = \sqrt{4z_s^2 + \tilde{r}^2}$ is the length of the shortest path in the single reflection channel from transmitter via the floor to point $\vec{a}_b$, the unit step function is used to make sure the CIR has non-zero value only after the minimum delay and $\mathcal{F}_{\mathrm{fcr}}$ represents the scaling factor. Many potential functions for $\mathcal{F}_{\mathrm{tfc}}$ can be found by using curve-fitting tool. Here, we have chosen the following function for the scaling factor:

$$\mathcal{F}_{\mathrm{fcr}} = \beta_{\mathrm{tfc}}\frac{\tilde{r}^2}{z_s^2} + 1, \tag{19}$$

where the factor β_{tfc} is related to the Lambertian emission order m, and a suitable function for β_{tfc} is found to be $0.006242(m + 0.2578)^2 + 0.1328$. The approximation by using the scaling factor (19) is found to be accurate in the region of interest. In addition, this scaling factor provide an opportunity to further simplify the final CIR expression, which will be shown in the following derivations. The details and accuracy of this approximation has been demonstrated in Appendix B. By inserting (18) into (17), the CIR expression for the TFCR category can be simplified as:

$$h_{\mathrm{tfcr}}^{[2]}(t) = \int_{-\pi}^{\pi}\int_{0}^{\infty}\frac{2^{m+5}A_{\mathrm{pd}}c\rho_f\rho_c(m+1)z_s^{m+3}r}{\pi^2(z_s - z_r)^{-2}\left(r^2 + (z_s - z_r)^2\right)^2} \times \frac{\mathcal{F}_{\mathrm{tfc}}\mathbf{1}_{\mathrm{FoV}}^{c2r}\mathcal{U}\left(t - \frac{D_{\mathrm{tfcr},\vec{a}_b}}{c}\right)\mathrm{d}r\mathrm{d}\theta}{\left(ct - \sqrt{r^2 + (z_s - z_r)^2}\right)^{m+6}}, \tag{20}$$

where the term $D_{\mathrm{tfcr},\vec{a}_b}$ denotes the length of the shortest propagation path via point $\vec{a}_b$ in the TFCR channel. Its value can be calculated as:

$$\begin{aligned}D_{\mathrm{tfcr},\vec{a}_b} = &\sqrt{4z_s^2 + r^2 + \hat{W}^2 - 2r\hat{W}\cos\theta}\\ &+ \sqrt{r^2 + (z_s - z_r)^2}.\end{aligned} \tag{21}$$

The term with unit step function in (20) indicates that $h_{\mathrm{tfcr}}^{[2]}(t)$ is non-zero only when $ct \geq D_{\mathrm{tfcr},\vec{a}_b}$, which leads to the following

IEEE Proof

inequality:

$$\left(c^2t^2-\hat{W}^2\cos^2\theta\right)r^2+c^2t^2\left(z_s-z_r\right)^2 -\left(c^2t^2-\hat{W}^2-\left(z_s+z_r\right)\left(3z_s-z_r\right)\right)\hat{W}\cos\theta r -\frac{1}{4}\left(c^2t^2-\hat{W}^2-\left(z_s+z_r\right)\left(3z_s-z_r\right)\right)^2\leq 0. \quad (22)$$

With the satisfaction of (22), the integration limits in (20) can be changed to finite values, and the unit step function in (20) can be changed to $\mathcal{U}(t-D_{\mathrm{tfcr,min}}/c)$, where $D_{\mathrm{tfcr,min}}=\sqrt{(3z_s-z_r)^2+\hat{W}^2}$. Thus, (20) can be further modified as:

$$h^{[2]}_{\mathrm{tfcr}}(t)=\int_{\mathfrak{r}_1}^{\mathfrak{r}_2}\int_0^{\vartheta}\frac{2^{m+6}A_{\mathrm{pd}}c\rho_f\rho_c(m+1)z_s^{m+3}r\mathcal{F}_{\mathrm{tfc}}\mathbf{1}^{c2r}_{\mathrm{FoV}}}{\pi^2(z_s-z_r)^{-2}\left(ct-\sqrt{r^2+(z_s-z_r)^2}\right)^{m+6}} \times\frac{\mathcal{U}\left(t-\frac{D_{\mathrm{tfcr,min}}}{c}\right)\mathrm{d}\theta\mathrm{d}r}{\left(r^2+(z_s-z_r)^2\right)^2}. \quad (23)$$

Note that in the modification (23), the expression is multiplied by a factor of 2, and the lower limit of the integral with θ is change to 0. This is because expression (20) is reflection symmetric with respect to the x-axis. The integration limits $\mathfrak{r}_1$ and $\mathfrak{r}_2$ in (23) can be calculated by solving the inequality (22) with r as the unknown variable. The boundary values of r can be found as:

$$r_1=\frac{\hat{W}\left(c^2t^2-\mathfrak{c}_{\mathrm{tfcr},1}\right)-ct\sqrt{\mathfrak{c}_{\mathrm{tfcr},2}}}{2\left(c^2t^2-\hat{W}^2\right)}, \quad (24)$$

$$r_2=\frac{\hat{W}\left(c^2t^2-\mathfrak{c}_{\mathrm{tfcr},1}\right)+ct\sqrt{\mathfrak{c}_{\mathrm{tfcr},2}}}{2\left(c^2t^2-\hat{W}^2\right)}, \quad (25)$$

where $\mathfrak{c}_{\mathrm{tfcr},1}=\hat{W}^2+(z_s+z_r)(3z_s-z_r)$ and $\mathfrak{c}_{\mathrm{tfcr},2}=(c^2t^2-\mathfrak{c}_{\mathrm{tfcr},1})^2-4(z_s-z_r)^2(c^2t^2-\hat{W}^2)$. Then, the solution to the integration limits are $\mathfrak{r}_1=\max(r_1,0)$ and $\mathfrak{r}_2=r_2$. The integration limit ϑ can also be calculated by solving the same equation originated from (22) with θ as the unknown. The solution to the limit ϑ is found as:

$$\vartheta=\begin{cases}\arccos\left(\dfrac{2ct\sqrt{r^2+(z_s-z_r)^2}-c^2t^2+\mathfrak{c}_{\mathrm{tfcr},1}}{2r\hat{W}}\right) & :r\geq -r_1\\ \pi & :r<-r_1\end{cases}, \quad (26)$$

The approximation in (18) makes (23) a simple function of θ. This creates an opportunity to solve the integral with respect to θ, thereby further simplifying (23). Therefore, the final CIR expression for the TFCR category can be written in a form with a 1-D integral as (27).

$$h^{[2]}_{\mathrm{tfcr}}(t)=\frac{2^{m+6}cA_{\mathrm{pd}}\rho_f\rho_c(m+1)}{\pi^2\left(z_s-z_r\right)^{-2}z_s^{-m-1}}\mathcal{U}\left(t-\frac{D_{\mathrm{tfcr,min}}}{c}\right) \int_{\mathfrak{r}_1}^{\mathfrak{r}_2}\frac{\vartheta\left(\beta_{\mathrm{tfc}}\left(r^2+\hat{W}^2-\frac{2r\hat{W}\sin\vartheta}{\vartheta}\right)+z_s^2\right)r\mathbf{1}^{c2r}_{\mathrm{FoV}}\mathrm{d}r}{\left(r^2+(z_s-z_r)^2\right)^2\left(ct-\sqrt{r^2+(z_s-z_r)^2}\right)^{m+6}} \quad (27)$$

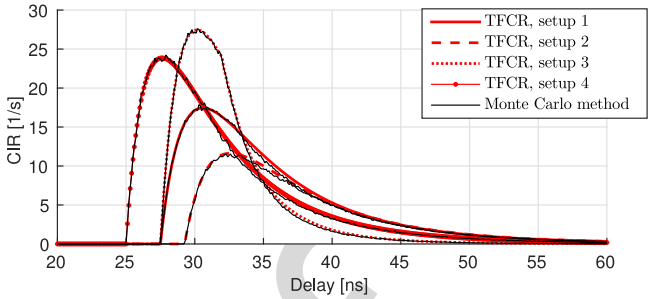

Fig. 9. NLoS CIR results with TFCR category. Setup 1: $\phi_{1/2}=60°$, $\psi_{\mathrm{FoV}}=90°$, $\hat{W}=0$ m and $z_r=0.75$ m. Compared to the configuration in setup 1, $\hat{W}$ is modified to 3 m in setup 2, $\phi_{1/2}$, ψ_{FoV} are modified to $40°$, $45°$ in setup 3, and z_r is modified to 1.5 m in setup 4, respectively. The configuration of the remaining parameters are listed in Table I.

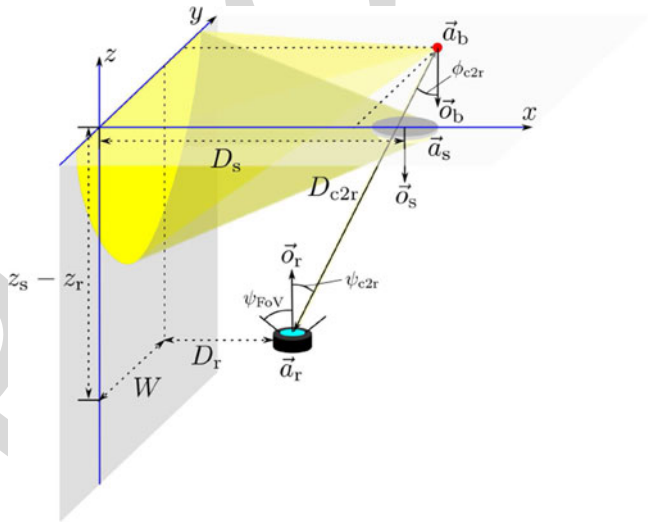

Fig. 10. Light propagation geometry in TWCR channel.

Fig. 9 shows a number of CIRs of the TFCR category with different setups calculated using (27). In addition, the corresponding CIR results generated using the Monte Carlo method are also presented in Fig. 9. The agreement between the CIR results generated by different methods validate the CIR calculation expression in TFCR category (27).

C. Transmitter-to-Wall-to-Ceiling-to-Receiver Channel Impulse Response (TWCR)

In the TWCR category, the ceiling and wall are considered as shown in Fig. 10. The boundary of the ceiling and wall planes is the line of their intersection, and these two planes extend

IEEE Proof

infinitely to other directions. Again, a point located at $\vec{a}_b$ on the ceiling is considered, as shown in Fig. 10. This time the space is defined by a 3-D Cartesian coordinate system x-y-z. The origin is defined at the projection point of the transmitter on the wall plane. Thus, the coordinate of the ceiling point $\vec{a}_b$ is defined at $(x, y, 0)$. Similar to the CIR calculation for the TFCR category, a single reflection channel from the transmitter to the ceiling point $\vec{a}_b$ is considered, except that the channel is resulted from the reflection by the wall plane. It is defined as transmitter-to-wall-to-ceiling point (TWC) channel. Again the corresponding CIR can be calculated using (2) as:

$$\mathrm{d}h^{\vec{a}_b}_{\mathrm{twc}}(t) = \hbar^{[0,1,0],[0,1,0]}_{\{m,\mathrm{d}A,\rho_w,D_s,x,|y|,90^\circ\}}(t). \tag{28}$$

In a Cartesian coordinate system, the detection area differential $\mathrm{d}A$ can be converted to $\mathrm{d}x\mathrm{d}y$. Next, the LoS transmission from the ceiling bouncing point $\vec{a}_b$ to the receiver is considered, which introduces a further attenuation and an extra delay on top of the TWC channel. The resulting CIR can be found as:

$$\mathrm{d}h^{\vec{a}_b}_{\mathrm{twcr}}(t) = \rho_c G^{\vec{a}_b}_{c2r}\,\mathrm{d}h^{\vec{a}_b}_{\mathrm{twc}}\left(t - \tau^{\vec{a}_b}_{c2r}\right), \tag{29}$$

which is the same as (15) except the category of the single reflection channel. The LoS path loss $G^{\vec{a}_b}_{c2r}$ is again calculated using (16). The additional delay is again $\tau^{\vec{a}_b}_{c2r} = D_{c2r}/c$. However, due to the use of a different coordinate system, the calculation of the Euclidean distance follows the expression below:

$$D_{c2r} = \sqrt{(z_s - z_r)^2 + (x - D_r)^2 + (y - W)^2}. \tag{30}$$

In order to calculate the final CIR for the TWCR category, all of the paths reflected by the ceiling are considered, which leads to an integration of (29) over the ceiling plane as:

$$h^{[2]}_{\mathrm{twcr}}(t) = \int_{-\infty}^{\infty}\int_{0}^{\infty} \frac{\rho_c (z_s - z_r)^2 A_{\mathrm{pd}} \mathbf{1}^{c2r}_{\mathrm{FoV}}}{\pi D^4_{c2r}} \times \hbar^{[0,1,0],[0,1,0]}_{\{m,\mathrm{d}x\mathrm{d}y,\rho_w,D_s,x,|y|,90^\circ\}}\left(t - \frac{D_{c2r}}{c}\right). \tag{31}$$

In order to reduce the complexity of (31), we can use a simpler approximated expression for (28). It has been found that the special case of $y = 0$ m in the calculation of (28) leads to a simpler and closed form expression. Similar to the approximation in (18), the following expression with magnitude scaling and minimum delay control is used to approximate the exact CIR (28):

$$\mathrm{d}h^{\vec{a}_b}_{\mathrm{twc}}(t) \approx \mathcal{F}_{\mathrm{twc}}\hbar^{[0,1,0],[0,1,0]}_{\{m,\mathrm{d}x\mathrm{d}y,\rho_w,\hat{D}_s,\hat{x},0,90^\circ\}} = \frac{\rho_w \hat{D}_s \hat{x} \mathcal{B}\left(\frac{m+2}{2},\frac{m+2}{2}\right) \mathfrak{r}^2_{\mathrm{twc}}(t) \mathcal{F}_{\mathrm{twc}} \mathcal{U}\left(t - \frac{D_{\mathrm{twc},\vec{a}_b}}{c}\right)\mathrm{d}x\mathrm{d}y}{\frac{\pi^2 t}{2^m(m+1)}\left(1 + \frac{\hat{D}^2_s}{\mathfrak{r}^2_{\mathrm{twc}}(t)}\right)^{\frac{m-1}{2}}\left(\frac{c^2t^2}{4} - \frac{\left(\hat{D}^2_s - \hat{x}^2\right)^2}{4c^2t^2}\right)^3}, \tag{32}$$

where $D_{\mathrm{twc},\vec{a}_b} = \sqrt{(D_s + x)^2 + y^2}$ is the length of the shortest path in the single reflection channel from the transmitter via the wall to point $\vec{a}_b$, $\mathcal{B}(u_1, u_2)$ is the β-function that is defined as: $\mathcal{B}(u_1, u_2) = \int_0^1 v^{u_1-1}(1-v)^{u_2-1}\mathrm{d}v$, and

$$\mathfrak{r}^2_{\mathrm{twc}}(t) = \frac{c^2t^2}{4} + \frac{\left(\hat{D}^2_s - \hat{x}^2\right)^2}{4c^2t^2} - \frac{\hat{D}^2_s + \hat{x}^2}{2}. \tag{33}$$

In the approximated expression (32), $\mathcal{F}_{\mathrm{twc}}$ is the scaling factor. Suitable functions for $\mathcal{F}_{\mathrm{twc}}$ can be obtained by using curve fitting tools. The following function is one of them:

$$\mathcal{F}_{\mathrm{twc}} = \left(1 + \frac{y^2 + \beta_{\mathrm{twc},1}\frac{y^3|x-D_s|^3}{(x+D_s)^4}}{(x + \beta_{\mathrm{twc},2}D_s)^2}\right)^{-\frac{1}{2}}, \tag{34}$$

where $\beta_{\mathrm{twc},1} = 0.8125$ and $\beta_{\mathrm{twc},2} = 0.8088\mathrm{e}^{-0.6878m} + 0.5304\mathrm{e}^{-0.007006m}$ are found to provide an accurate approximation. Note that expression (2) has been used in both (28) and (32). The values for L_s and L_r are D_s and x in (28). However, they have been substituted with $\hat{D}_s$ and $\hat{x}$ in (32). This is because a simple linear scaling by $\mathcal{F}_{\mathrm{twc}}$ cannot provide an approximation with sufficient accuracy. The values for L_s and L_r have to be manipulated based on the parameter D_s, x, y and m in order to achieve an accurate approximation. In addition, the minimum delay control is realised by this step. The following functions for $\hat{D}_s$ and $\hat{x}$ are found to provide accurate approximations:

$$\hat{D}_s = \beta_{\mathrm{twc},3} D_{\mathrm{twc},\vec{a}_b}, \tag{35}$$

$$\hat{x} = (1 - \beta_{\mathrm{twc},3}) D_{\mathrm{twc},\vec{a}_b}, \tag{36}$$

where $\beta_{\mathrm{twc},3} = D_s((D_s + x)^2 + 4y^2(m^{0.045} - 1))^{-\frac{1}{2}}$ is found to provide an accurate approximation. Note that the approximation in (32) is more complex than that in (18). This is because the factors in approximation (32) are functions of four parameters D_s, x, y and m. In contrast, the factors in (18) are functions of two parameters m and $\tilde{r}$ only. The details and accuracy of the approximation (32) are provided in Appendix C.

Thus, by inserting (32) into (31), the CIR expression for the TWCR category can be calculated as:

$$h^{[2]}_{\mathrm{twcr}}(t) = \int_{-\infty}^{\infty}\int_{0}^{\infty} \frac{2^m \rho_w \rho_c A_{\mathrm{pd}} \hat{D}_s \hat{x} \mathcal{B}\left(\frac{m+2}{2},\frac{m+2}{2}\right) \mathbf{1}^{c2r}_{\mathrm{FoV}}}{\frac{\pi^3 D^4_{c2r}\left(t - \frac{D_{c2r}}{c}\right)}{(m+1)(z_s - z_r)^2}\left(1 + \frac{\hat{D}^2_s}{\mathfrak{r}^2_{\mathrm{twc}}\left(t - \frac{D_{c2r}}{c}\right)}\right)^{\frac{m-1}{2}}} \times \frac{\mathfrak{r}^2_{\mathrm{twc}}\left(t - \frac{D_{c2r}}{c}\right)\mathcal{F}_{\mathrm{twc}}\mathcal{U}\left(t - \frac{D_{\mathrm{twcr},\vec{a}_b}}{c}\right)\mathrm{d}x\mathrm{d}y}{\left(\frac{(ct - D_{c2r})^2}{4} - \frac{\left(\hat{D}^2_s - \hat{x}^2\right)^2}{4(ct - D_{c2r})^2}\right)^3}, \tag{37}$$

where $D_{\mathrm{twcr},\vec{a}_b}$ denotes the length of the shortest propagation path via point $\vec{a}_b$ in the TWCR channel. Its value can be calculated as:

$$D_{\mathrm{twcr},\vec{a}_b} = \sqrt{(z_s - z_r)^2 + (x - D_r)^2 + (y - W)^2} + \sqrt{(D_s + x)^2 + y^2}. \tag{38}$$

The unit step function in (37) indicates that $h^{[2]}_{\mathrm{twcr}}(t)$ is non-zero only when $ct \geq D_{\mathrm{twcr},\vec{a}_b}$, which leads to the following

IEEE Proof

inequality:

$$\left(c^2t^2-W^2\right)y^2-W\left(c^2t^2+2\left(D_s+D_r\right)x-\left(z_s-z_r\right)^2-W^2-D_r^2+D_s^2\right)y+c^2t^2\left(D_s+x\right)^2-\frac{1}{4}\left(c^2t^2-W^2+2\left(D_s+D_r\right)x-\left(z_s-z_r\right)^2-D_r^2+D_s^2\right)^2\geq 0. \quad (39)$$

With the satisfaction of (39), the integration limits in (37) should be changed to finite values, and the term with the unit step function in (37) can be replaced by $\mathcal{U}(t-D_{\mathrm{twcr,min}}/c)$, where $D_{\mathrm{twcr,min}}$ is the length of the shortest propagation path in the TWCR channel. It can be calculated as:

$$D_{\mathrm{twcr,min}}=\sqrt{W^2+\left(D_s+\sqrt{\left(z_s-z_r\right)^2+D_r^2}\right)^2}. \quad (40)$$

Thus, (37) can be further modified as (41) shown at bottom of this page. The integration limits $\mathfrak{y}_1$ and $\mathfrak{y}_2$ in (41) can be calculated by solving the equation originated from inequality (39) with y as the unknown variable. The solutions to $\mathfrak{y}_1$ and $\mathfrak{y}_2$ can be found as:

$$\mathfrak{y}_2=\frac{W\left(c^2t^2-\mathfrak{c}_{\mathrm{twcr},1}+2\left(D_s+D_r\right)x\right)+ct\sqrt{\mathfrak{c}_{\mathrm{twcr},2}}}{2\left(c^2t^2-W^2\right)}, \quad (42)$$

$$\mathfrak{y}_1=\frac{W\left(c^2t^2-\mathfrak{c}_{\mathrm{twcr},1}+2\left(D_s+D_r\right)x\right)-ct\sqrt{\mathfrak{c}_{\mathrm{twcr},2}}}{2\left(c^2t^2-W^2\right)}, \quad (43)$$

where $\mathfrak{c}_{\mathrm{twcr},1}=(z_s-z_r)^2+W^2+D_r^2-D_s^2$ and $\mathfrak{c}_{\mathrm{twcr},2}=(c^2t^2-\mathfrak{c}_{\mathrm{twcr},1}+2(D_s+D_r)x)^2-4(c^2t^2-W^2)(D_s+x)^2$. To ensure the existence of the real-value solution to $\mathfrak{y}_1$ and $\mathfrak{y}_2$, the term $\mathfrak{c}_{\mathrm{twcr},2}$ have to be greater than zero, which leads to the solution to the integration limit $\mathfrak{x}$:

$$\mathfrak{x}=\frac{\left(\sqrt{c^2t^2-W^2}-D_s\right)^2-\left(z_s-z_r\right)^2-D_r^2}{2\left(\sqrt{c^2t^2-W^2}-D_s-D_r\right)}. \quad (44)$$

Fig. 11 shows a number of CIRs of the TWCR category with different configurations calculated using (41). In addition, the corresponding results generated using the Monte Carlo method are also provided for comparison. The agreement between the CIR results generated by different methods validate the CIR calculation expression for the TWCR category (41).

V. Overall Non-Line-of-Sight Channel Impulse Response

In conjunction with the analytical results for component CIRs in different light propagation categories, the overall CIR can be accurately approximated. Note that the TWR, TWCR component CIRs are with respect to a single wall. Since there are four walls in a typical room, the overall NLoS is the superposition of four TWR, four TWCR and one TFCR component CIRs. In order to calculate each component CIR, the related geometric parameters should be calculated based on the given information. The known information includes the room dimension $l_x\times l_y\times l_z$, the position of the transmitter $\vec{a}_s=[x_s,y_s,z_s]$ and the position of the receiver $\vec{a}_r=[x_r,y_r,z_r]$, as shown in Fig. 12. The geometric parameters that requires calculation include $D_{s,n}, D_{r,n}, W_n, \hat{W}$. Note that the subscript $n=1,2,3,4$ is used to distinguish the same type of parameters with respect to different walls. The cases with $n=1$ and $n=2$ correspond to the wall with $y=0$ and $y=l_y$, respectively. The cases with $n=3$ and $n=4$ correspond to the wall with $x=0$ and $x=l_x$, respectively. The calculation of these parameters can be straightforwardly inferred from Fig. 12 using Euclidean geometry. The equations for the calculation are concluded in Table II.

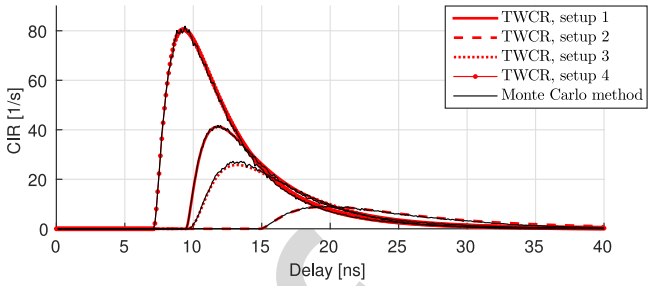

Fig. 11. NLoS CIR results with TWCR category. Setup 1: $\phi_{1/2}=60°$, $\psi_{\mathrm{FoV}}=90°$, $D_s=0.5$ m, $D_r=0.5$ m, $W=0.5$ m and $z_r=0.75$ m. Compared to the configuration in setup 1, D_s, D_r, W are modified to 1, 2, 2 m in setup 2, $\phi_{1/2}$, ψ_{FoV} are modified to $40°$, $45°$ in setup 3, and z_r is modified to 1.5 m in setup 4, respectively. The configuration of the remaining parameters are listed in Table I.

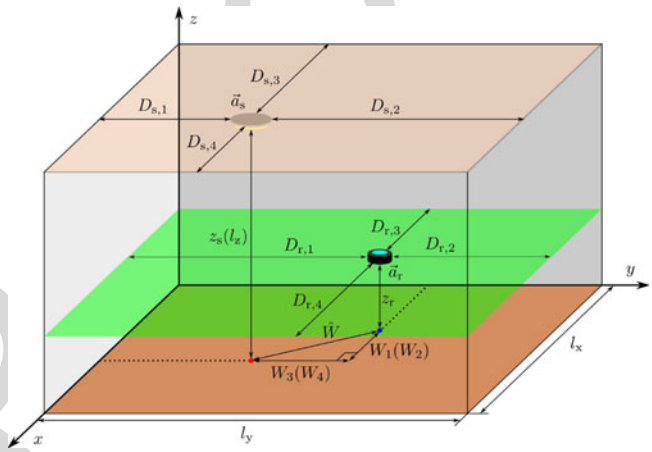

Fig. 12. A cuboid room of size $l_x\times l_y\times l_z$ with transmitter and receiver location of $\vec{a}_s$ and $\vec{a}_r$, respectively.

$$h^{[2]}_{\mathrm{twcr}}(t)=\frac{2^m\rho_w\rho_c A_{\mathrm{pd}}\mathcal{B}\left(\frac{m+2}{2},\frac{m+2}{2}\right)}{\pi^3(m+1)^{-1}\left(z_s-z_r\right)^{-2}}\int_{\mathfrak{y}_1}^{\mathfrak{y}_2}\int_0^{\mathfrak{x}}\frac{\mathbf{1}^{c2r}_{\mathrm{FoV}}\hat{D}_s\hat{x}\mathfrak{r}^2_{\mathrm{twc}}\left(t-\frac{D_{c2r}}{c}\right)\mathcal{F}_{\mathrm{twc}}\mathcal{U}\left(t-\frac{D_{\mathrm{twcr,min}}}{c}\right)\mathrm{d}x\mathrm{d}y}{D^4_{c2r}\left(t-\frac{D_{c2r}}{c}\right)\left(1+\frac{\hat{D}_s^2}{\mathfrak{r}^2_{\mathrm{twc}}\left(t-\frac{D_{c2r}}{c}\right)}\right)^{\frac{m-1}{2}}\left(\frac{\left(ct-D_{c2r}\right)^2}{4}-\frac{\left(\hat{D}_s^2-\hat{x}^2\right)^2}{4\left(ct-D_{c2r}\right)^2}\right)^3} \quad (41)$$

IEEE Proof

TABLE II
CALCULATION OF GEOMETRIC PARAMETERS

n	1	2	3	4
$D_{\mathrm{s},n}$	y_s	$l_\mathrm{y}-y_\mathrm{s}$	x_s	$l_\mathrm{x}-x_\mathrm{s}$
$D_{\mathrm{r},n}$	y_r	$l_\mathrm{y}-y_\mathrm{r}$	x_r	$l_\mathrm{x}-x_\mathrm{r}$
W_n	$\lvert x_\mathrm{s}-x_\mathrm{r}\rvert$		$\lvert y_\mathrm{s}-y_\mathrm{r}\rvert$	
$\hat{W}$	$\sqrt{(x_\mathrm{s}-x_\mathrm{r})^2+(y_\mathrm{s}-y_\mathrm{r})^2}$			

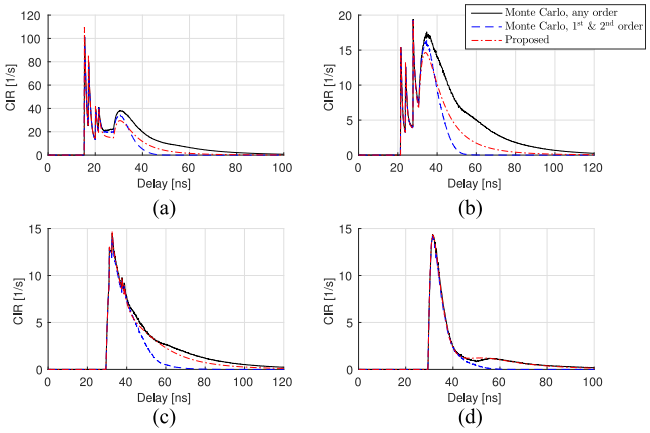

Fig. 13. NLoS CIR results with different configurations. The sub-plot (a), (b), (c) and (d) correspond to the link setup 1, 2, 3 and 4, respectively. In addition to the results generated using the proposed method, those generated using the Monte Carlo method considering any order of reflections and considering 1st and 2nd order reflections are also presented.

TABLE III
LINK CONFIGURATIONS CORRESPOND TO THE NLoS CIR RESULTS SHOWN IN FIG. 13

Parameter	Room size [m]	Transmitter coordinate [m]	Receiver coordinate [m]
Setup 1	$5\times5\times3$	$[2.5, 2.5, 3]$	$[2\ 1.5\ 0.75]$
Setup 2	$5\times8\times3$	$[2, 2, 3]$	$[2.5, 6, 0.75]$
Setup 3	$10\times10\times3$	$[4, 4, 3]$	$[5, 7, 0.75]$
Setup 4	$10\times10\times3$	$[4, 4, 3]$	$[5, 7, 0.75]$

Then, the overall NLoS CIR can be calculated as the sum of the nine component CIRs as:

$$h_{\mathrm{NLoS}}(t) \approx \sum_{n=1}^{4} h_{\mathrm{twr}}^{[1],\{D_{s,n},D_{r,n},W_n\}}(t) + h_{\mathrm{tfcr}}^{[2],\{\hat{W}\}}(t) + \sum_{n=1}^{4} h_{\mathrm{twcr}}^{[2],\{D_{s,n},D_{r,n},W_n\}}(t), \tag{45}$$

where $h_{\mathrm{twr}}^{[1],\{D_{s,n},D_{r,n},W_n\}}(t)$, $h_{\mathrm{tfcr}}^{[2],\{\hat{W}\}}(t)$ and $h_{\mathrm{twcr}}^{[2],\{D_{s,n},D_{r,n},W_n\}}(t)$ can be calculated using (12), (27) and (41), respectively.

A. Channel Impulse Response and Frequency Response Results

Fig. 13 shows the NLoS CIR results based on (45) in comparison to the results from using the Monte Carlo method. The setups of the analytical calculations and corresponding simulations are listed in Table III. A small square room and a longer rectangular room are considered in setup 1 and setup 2, respectively. A much larger room is considered in setup 3 and setup 4. A half-power semi-angle of $\phi_{1/2}=60^\circ$ and a receiver FoV of $\psi_{\mathrm{FoV}}=90^\circ$ are used in setup 1, 2 and 3. In setup 4, $\phi_{1/2}=40^\circ$ and $\psi_{\mathrm{FoV}}=45^\circ$. In setup 1, the transmitter and the receiver are close to each other, the size of the room is relatively small, and the link is sufficiently close to the walls. Consequently, the overall magnitude of the NLoS CIR is relatively higher, and the responses due to 1st order reflections dominate the NLoS CIR, especially for the responses with short delays. In setup 2, the increased indoor space and the increased transmitter receiver separation leads to a NLoS CIR with a decreased magnitude. In setups 3 and 4, the considered transmitter/receiver positions are further away from the walls. Consequently, the magnitude of the CIRs due to 1st order reflections decreases significantly. Compared to setup 3, smaller transmitter half-power semiangle $\phi_{1/2}$ and receiver FoV ψ_{FoV} are used in setup 4. Consequently, the magnitude of responses with longer delays is decreased. This is because the majority of the detected signal with a long delay is launched from the transmitter in a very large radiant angle, and very little optical power is radiated in the side directions of the transmitter with a small $\phi_{1/2}$. In addition, a signal with a long delay is also likely to reach the receiver with a very large incident angle, which cannot be detected by a receiver with a small ψ_{FoV}.

The accuracy of the approximation using the proposed method varies with the time delay. For the responses with short delays (roughly the first 10 ns), the proposed method offers excellent accuracy. For the responses with medium delay (roughly another 10 ns after the short delay), the proposed method underestimates the CIR due to the omission of the response caused by part of the 2nd reflections with TWWR, TFWR categories and higher order reflections. For the responses with a long delay, the proposed method over-estimate the CIR compared to the results generated using the Monte Carlo method considering the 1st and 2nd order reflections. This is because the proposed CIR calculation method with each propagation category omits the effects of the boundary of the surfaces, which introduces extra responses with a long delay. However, this over-estimation is lower than the responses caused by higher order reflections. From a different point of view, it slightly compensates the omission of the higher order reflections. In addition, the approximation accuracy is also related to the size of the room. The proposed method offers a better approximation in a large indoor environment (setup 3 and setup 4) compared to the cases in a smaller indoor environment (setup 3 and setup 4).

Fig. 14 shows the corresponding magnitude response of the NLoS channels. It can be observed that with the presence of a LoS path between the transmitter and the receiver, the accuracy of the approximation using the proposed method varies with frequency. For the magnitude response with extremely low frequency (<5 MHz), the proposed method underestimates the response relative to the case with the Monte Carlo method considering any order of reflections. However, comparing with the Monte Carlo method considering the 1st and 2nd order reflections, the proposed method offers a similar magnitude response. For the magnitude response with low frequency (5–50 MHz), the three curves are close to each other with a slight mismatch.

IEEE Proof

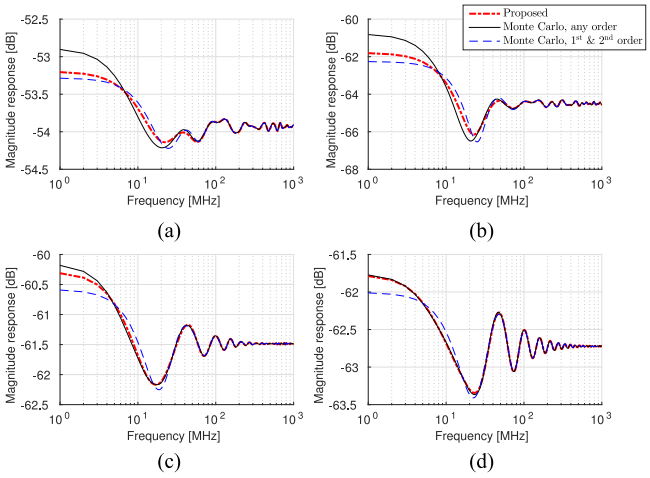

Fig. 14. NLoS magnitude response results with different configurations. The sub-plot (a), (b), (c) and (d) correspond to the link setup 1, 2, 3 and 4, respectively.

TABLE IV
SETUP CONFIGURATIONS IN THE COMPUTATION TIME EVALUATION

Parameter	Room size [m]	Transmitter coordinate [m]	Receiver coordinate [m]
Setup 1	$5 \times 5 \times 3$	$[2.5, 2.5, 3]$	$[2.5, 2.5, 0.75]$
Setup 2	$10 \times 10 \times 3$	$[2.5, 2.5, 3]$	$[7.5, 7.5, 0.75]$

For the magnitude response with high frequency (>50 MHz), the three curves are virtually identical.

B. Computational Time Evaluation

The calculation of (12), (27) and (41) requires solving only one or two 1-D numerical integrals. Therefore, the computational complexity of (45) is very low. In this section, the computation time of the proposed method is evaluated compared with that of the state-of-the-art methods. In this study, the numerical integrations in (45) are implemented based on the Trapezoidal rule, and the interval for each definite integral is divided into N bins. The greater the number of the bins, the more accurate the calculated result. Since θ is the variable in the integral (12), the number of bins in the integral (12) is defined as N_θ. Similarly, the numbers of bins in the calculation of (27) and (41) are defined as N_r and N_x (N_y), respectively. It has been empirically identified that $N_\theta = 50$, $N_r = 50$ and $N_x = N_y = 30$ offer reasonably accurate NLoS CIR results with a short computation time.

The impulse response of a channel is in the form of a continuous signal. In the actual CIR calculation, the result with a fixed time resolution is produced. By increasing the time resolution, a clearer view of the CIR can be obtained to characterise the channel with a wider frequency range. Two link setups are simulated to test the computation time while using three different methods. The configuration is listed in Table IV. The used half-power semi-angle is $\phi_{1/2} = 60°$, and the remaining parameters are the same as those listed in Table I. The first link considers a small room with a closely located transmitter and receiver in the centre. The second link considers a larger room with a distant separation between the transmitter and the receiver. Fig. 15 shows that the required computation time in Matlab

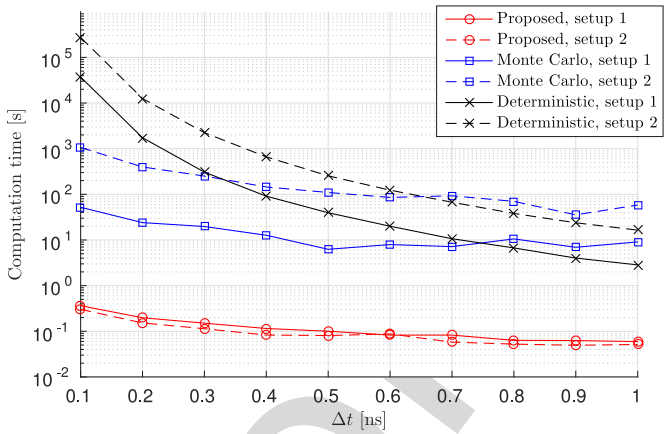

Fig. 15. NLoS CIR computation time with different calculation methods.

varies with the time resolution Δt. The considered calculation methods include the deterministic method proposed in [4], the Monte Carlo method proposed in [22] and the proposed method in this study. To ensure the fairness of the comparison, up to 2nd order reflections are considered in the deterministic method and Monte Carlo method. With the deterministic method, the block size is configured based on the time resolution as $A_e = 2c^2\Delta t^2$ [8]. With the Monte Carlo method, the ray-tracing process is repeated until the normalised mean square error (NMSE) of the CIR result is less than 2.5×10^{-3}. Calculating low time resolution CIR ($\Delta t > 0.7$ ns), the deterministic and Monte Carlo methods are able to calculate the results with a computation time in the range of a few seconds to about 100 s. With the same time resolution, the proposed method is able to finish the calculation with a computation time of less than 0.1 s. With the decrease of Δt, the required computation time for all three methods increases. The required time for the deterministic method increases significantly. In the case of $\Delta t = 0.1$ ns, the computation time for the deterministic method is in the range of several hours to more than three days. This is because the increased time resolution leads to a significantly increased number of blocks that are smaller in size. Since the deterministic method considers all possible propagation paths between blocks and their combinations, the increased number of blocks significantly increases the computational complexity. In addition, increasing the room size requires a greater number of blocks to fill the larger internal surface area. Therefore, for the deterministic method, the computation time also increases significantly with the increase in the room size. With the Monte Carlo method, the increase of computation time with the decrease of Δt is not as significant as that with the deterministic method. With $\Delta t = 0.1$ ns, several minutes are required to obtain an accurate CIR result. This increase in computation time is due to the time bin width getting narrower as the time resolution increases. A narrower bin width requires more samples to average out the noise caused by the random process. In setup 2, the receiver is further away from the transmitter. Consequently, the traced ray has a lower probability to reach the region close to the receiver. Therefore, more computation time is required for the Monte Carlo method if the separation between the transmitter

IEEE Proof

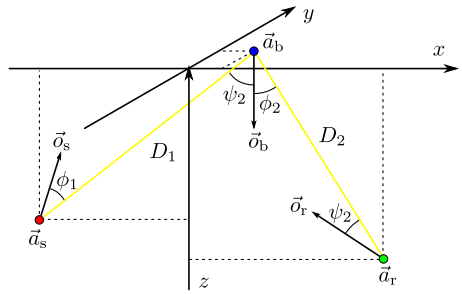

Fig. 16. Single reflection channel in Cartesian coordinates.

and receiver increases. In contrast, the computation time for the proposed method increases slightly with the decrease of Δt. With a time resolution of $\Delta t = 0.1$ ns, the computation time for the proposed method is still less than a second. Furthermore, the required computation time varies slightly for different link setups.

VI. Conclusions

In this paper, a computationally efficient analytical method was proposed to calculate the NLoS CIR in typical VLC deployments. The CIR results calculated using the proposed method are compared with those generated by using the Monte Carlo method in [9] and the deterministic ray-tracing method in [4]. In comparison with the benchmark methods, the proposed method can provide accurate CIR results for NLoS channels with up to 2nd order reflections. Furthermore, the required time for the proposed method is significantly shorter than the benchmarks (typically less than a second). This method is useful for research that requires a large number of channel samples considering NLoS components, such as VLC MIMO [14] or system level studies of networked VLC [23].

Appendix A
Derivation of Proposition 1

Firstly, we place the setup shown in Fig. 2 in a Cartesian coordinate system. As shown in Fig. 16, the locations of the source element and the receiving element are defined in the coordinates as $\vec{a}_s = [-L_s L_b/(L_s + L_r), 0, -L_s]$ and $\vec{a}_r = [L_r L_b/(L_s + L_r), 0, -L_r]$, respectively. The orientations of the source element and the receiving element are defined as $\vec{o}_s = [\tilde{x}_s, \tilde{y}_s, \tilde{z}_s]$ and $\vec{o}_r = [\tilde{x}_r, \tilde{y}_r, \tilde{z}_r]$. All orientation vectors have a unity modulus. Considering the amount of light power incident to a point on the reflector at $\vec{a}_b = [x, y, 0]$, the Euclidean distance between the source and this point is D_1 and the Euclidean distance between the receiver and this point is D_2. The orientation of the reflector $\vec{o}_b$ is opposite to the direction of the z-axis. According to [21], the calculus of the path loss via $\vec{a}_b$ can be calculated as:

$$\mathrm{d}G = \frac{\rho(m+1)A_r \mathrm{d}A}{2\pi^2 D_1^2 D_2^2} \mathbf{1}_{\mathrm{FoV}} \cos^m \phi_1 \cos\psi_1 \cos\phi_2 \cos\psi_2, \tag{A.1}$$

where ϕ_1 and ψ_1 denote the radiant angle and incident angle from the light source and to the point at $\vec{a}_b$ on the reflector, respectively; ϕ_2 and ψ_2 denote the radiant angle and incident angle from the the point at $\vec{a}_b$ on the reflector to the receiving element, respectively; $\mathrm{d}A$ denotes the differential of the physical area of the reflecting point; and $\mathbf{1}_{\mathrm{FoV}}$ is the indicator function showing whether the path is within the FoV of the receiver and within the coverage of the source. This leads to:

$$\mathbf{1}_{\mathrm{FoV}} = \begin{cases} 1 & : \cos\psi_1 \geq 0 \ \& \ \cos\psi_2 \geq \cos\psi_{\mathrm{FoV}} \\ 0 & : \text{otherwise} \end{cases}. \tag{A.2}$$

The relevant terms in (A.1) can be calculated as [4]:

$$D_1 = \sqrt{\left(x + \frac{L_s L_b}{L_s + L_r}\right)^2 + y^2 + L_s^2},$$

$$D_2 = \sqrt{\left(x - \frac{L_r L_b}{L_s + L_r}\right)^2 + y^2 + L_r^2},$$

$$\cos\phi_1 = \frac{\vec{o}_s \left(\vec{a}_b - \vec{a}_s\right)^T}{D_1} = \frac{\tilde{x}_s \left(x + \frac{L_s L_b}{L_s + L_r}\right) + \tilde{y}_s y + \tilde{z}_s L_s}{D_1},$$

$$\cos\psi_1 = \frac{\vec{o}_b \left(\vec{a}_s - \vec{a}_b\right)^T}{D_1} = \frac{L_s}{D_1},$$

$$\cos\phi_2 = \frac{\vec{o}_b \left(\vec{a}_r - \vec{a}_b\right)^T}{D_2} = \frac{L_r}{D_2},$$

$$\cos\psi_2 = \frac{\vec{o}_r \left(\vec{a}_b - \vec{a}_r\right)^T}{D_2} = \frac{\tilde{x}_r \left(x - \frac{L_r L_b}{L_s + L_r}\right) + \tilde{y}_r y + \tilde{z}_r L_r}{D_2}.$$

Thus, (A.1) can be rewritten as:

$$\mathrm{d}G(x, y) = \frac{\rho(m+1)A_r L_s L_r}{2\pi^2} \mathfrak{f}(x, y) \mathrm{d}x \mathrm{d}y \tag{A.3}$$

$$\begin{aligned} \mathfrak{f}(x, y) = \mathbf{1}_{\mathrm{FoV}} &\left(\tilde{x}_s \left(x + \frac{L_s L_b}{L_s + L_r}\right) + \tilde{y}_s y + L_s \tilde{z}_s\right)^m \\ &\times \left(\tilde{x}_r \left(x - \frac{L_r L_b}{L_s + L_r}\right) + \tilde{y}_r y + L_r \tilde{z}_r\right) \\ &\times \left(\left(x + \frac{L_s L_b}{L_s + L_r}\right)^2 + y^2 + L_s^2\right)^{-\frac{m+3}{2}} \\ &\times \left(\left(x - \frac{L_r L_b}{L_s + L_r}\right)^2 + y^2 + L_r^2\right)^{-2}. \end{aligned} \tag{A.4}$$

The total received signal power can be calculated by integrating (A.3) over the entire reflector.

However, channel impulse response is a quantity closely related to delay t. In order to make the received signal power involve the time delay, we firstly consider calculating the power of the received signal that experienced a delay of less than t. This amount of power is denoted as $\hat{P}_{\mathrm{opt},h}(t)$. The time delay is in conjunction with the length of the transmission path. With the given positions of the light source element and receiving element, all of the single reflection paths with a delay less than t are within an ellipsoid. The foci of this ellipsoid are located at the positions of light source and the receiving element as shown in Fig. 17. For the convenience of defining this ellipsoid, another Cartesian coordinate system x'-y'-z' is defined. In the x'-y'-z' system, the centre of the ellipsoid is placed at the origin

IEEE Proof

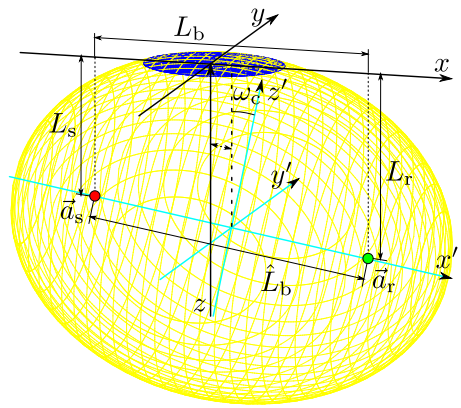

Fig. 17. Single reflection transmission geometry with considering the paths experiencing a delay less than a certain value t.

of the coordinates, and the two foci are placed on the x' axis with the coordinates of $[-\hat{L}_b/2, 0, 0]$ and $[\hat{L}_b/2, 0, 0]$, where $\hat{L}_b^2 = L_b^2 + (L_s - L_r)^2$. The equation for the ellipsoid can be written as:

$$\frac{x'^2}{(ct/2)^2} + \frac{y'^2}{(ct/2)^2 - \left(\hat{L}_b/2\right)^2} + \frac{z'^2}{(ct/2)^2 - \left(\hat{L}_b/2\right)^2} \leq 1,$$

With a given coordinate in x-y-z, the corresponding coordinate in x'-y'-z' can be obtained by carrying out a coordinate transformation as follows:

$$\begin{bmatrix} x' \\ y'z' \end{bmatrix} = \begin{bmatrix} \cos\omega_c & 0 & \sin\omega_c \\ 0 & 1 & 0 \\ -\sin\omega_c & 0 & \cos\omega_c \end{bmatrix} \begin{bmatrix} x \\ y \\ z \end{bmatrix} + \begin{bmatrix} \frac{2L_sL_r}{L_s+L_r}\sin\omega_c + \frac{\hat{L}_b(L_s-L_r)}{2(L_s+L_r)} \\ 0 \\ \frac{2L_sL_r}{L_s+L_r}\cos\omega_c \end{bmatrix}, \quad \text{(A.5)}$$

where ω_c is the rotation angle of the coordinates. It can be calculated using:

$$\omega_c = \arctan\left(\frac{L_s - L_r}{L_b}\right).$$

In conjunction with (A.5), the ellipsoid equation in the x-y-z system can be written as (A.6).

$$\frac{\left(x\cos\omega_c + z\sin\omega_c + \frac{2L_sL_r}{L_s+L_r}\sin\omega_c + \frac{\hat{L}_b(L_s-L_r)}{2(L_s+L_r)}\right)^2}{\left(\frac{ct}{2}\right)^2} + \frac{y^2}{\left(\frac{ct}{2}\right)^2 - \left(\frac{\hat{L}_b}{2}\right)^2} + \frac{\left(z\cos\omega_c - x\sin\omega_c + \frac{2L_sL_r}{L_s+L_r}\cos\omega_c\right)^2}{\left(\frac{ct}{2}\right)^2 - \left(\frac{\hat{L}_b}{2}\right)^2} \leq 1 \quad \text{(A.6)}$$

In the case that the signal is reflected by a single diffusing surface, all reflected points have to fulfil the condition $z = 0$, which leads to an ellipse on the x-y plane as:

$$\mathcal{W}_0(t): \left(1 - \frac{L_b^2}{c^2t^2}\right)x^2 + \left(\frac{L_b(L_s - L_r)\left(c^2t^2 - L_0^2\right)}{c^2t^2(L_s + L_r)}\right)x + y^2 - \frac{\left(c^2t^2 - L_0^2\right)^2}{(L_s + L_r)^2}\left(\frac{(L_s - L_r)^2}{4c^2t^2} + \frac{L_sL_r}{c^2t^2 - L_0^2}\right) \leq 0. \quad \text{(A.7)}$$

This ellipse defines the integration limits for x and y when calculating $\hat{P}_{\mathrm{opt},h}(t)$. Therefore, $\hat{P}_{\mathrm{opt},h}(t)$ can be calculated as:

$$\hat{P}_{\mathrm{opt},h}(t) = \iint_{\mathcal{W}_0(t)} \mathfrak{f}(x,y)\mathrm{d}x\mathrm{d}y.$$

Thus, the channel impulse response can be calculated as $\hbar(t) = \frac{\mathrm{d}\hat{P}_{\mathrm{opt},h}(t)}{\mathrm{d}t}$. For the convenience of calculating $\hbar(t)$, a polar coordinate system with a radius r and a polar angle θ is used. The polar coordinates can be calculated based on the following relationships:

$$x = r\cos\theta, \quad \text{(A.8)}$$

$$y = r\sin\theta. \quad \text{(A.9)}$$

By inserting (A.8) and (A.9) into (A.3), it gives:

$$\mathrm{d}G(r,\theta) = \frac{\rho(m+1)A_rL_sL_r}{2\pi^2}\mathfrak{f}(r,\theta)r\mathrm{d}r\mathrm{d}\theta,$$

where $\mathfrak{f}(r,\theta)$ can be found in (3). By inserting (A.8) and (A.9) into (A.7), it gives:

$$\mathcal{W}_0(t): \left(1 - \frac{L_b^2\cos^2\theta}{c^2t^2}\right)r^2 + \left(\frac{L_b(L_s - L_r)\left(c^2t^2 - L_0^2\right)\cos\theta}{c^2t^2(L_s + L_r)}\right)r - \frac{\left(c^2t^2 - L_0^2\right)^2}{(L_s + L_r)^2}\left(\frac{(L_s - L_r)^2}{4c^2t^2} + \frac{L_sL_r}{c^2t^2 - L_0^2}\right) \leq 0.$$

Thus, the channel impulse response can be decomposed into two one-dimensional integrals as:

$$\hbar(t) = \frac{\mathrm{d}}{\mathrm{d}t}\left(\frac{\rho(m+1)A_rL_sL_r}{2\pi^2}\int_0^{2\pi}\int_0^{\mathfrak{r}_\theta(t)}\mathfrak{f}(r,\theta)r\mathrm{d}r\mathrm{d}\theta\right),$$

where the value of the limit $\mathfrak{r}_\theta(t)$ can be calculated by evaluating the bound value of r in $\mathcal{W}_0(t)$. It is determined by making the inequality $\mathcal{W}_0(t)$ into an equality, and solving this equation with considering r as the unknown. Thus, this solution $\mathfrak{r}_\theta(t)$ can be concluded as (4). According to the Chain rule $\frac{\mathrm{d}}{\mathrm{d}t}\int_0^{g(t)} f(r)\mathrm{d}r = f(g(t))\frac{\mathrm{d}g(t)}{\mathrm{d}t}$, the CIR can be further simplified as (2).

Appendix B
Approximation in (18)

In this appendix, the approximation used in (18) is demonstrated, and the accuracy of the approximation with various parameters is evaluated. Firstly, the special case of (13) with

IEEE Proof

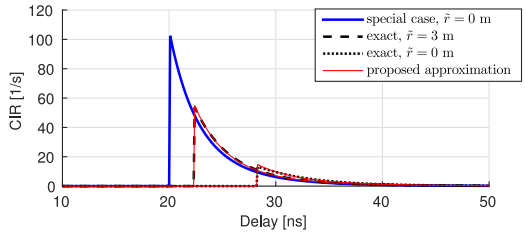

Fig. 18. An example of the comparison between the exact and approximated TFC CIR results with $\tilde{r}=0$, 3, 6 m.

$\tilde{r}=0$ m is considered. By making $\tilde{r}=0$, (13) can be rearranged as:

$$\begin{aligned}\mathrm{d}h^{\vec{a}_b}_{\mathrm{tfc},\tilde{r}=0}(t) &= \hbar^{[0,0,1],[0,0,1]}_{\{1,\mathrm{d}A,\rho_f,z_s,z_s,0,90^\circ\}}(t)\\ &= \frac{(m+1)\mathrm{d}A\rho_f z_s^{m+3}}{\pi(c/2)^{m+5}t^{m+6}},\end{aligned} \tag{B.1}$$

which is significantly simplified and in closed-form. It is worth noting that this is a special case of the result derived in [16]. An example of (B.1) is presented in Fig. 18. In this example, $\phi_{1/2}=60^\circ$ and the configuration of the remaining parameters are the same as those listed in Table I. Then, we calculate the CIR with $\tilde{r}=3$, 6 m using (13), which are also shown in Fig. 18. It can be observed that the shapes of the curves with different value of $\tilde{r}$ are similar. With the increase of $\tilde{r}$, the minimum delay of the response is longer due to the increased minimum transmission distance. In addition, the magnitude of the CIR is slightly increased compared to the special case of $\tilde{r}=0$ m. Therefore, we use a unit step function to control the minimum delay and a scaling factor to control the response magnitude in the approximated TFC CIR (18). The scaling factor $\mathcal{F}_{\mathrm{tfc}}$ only needs to vary with m and the ratio $\tilde{r}/z_s$ as the effects of the remaining parameters are preserved by (B.1). In Fig. 18, the approximated TFC CIR results are presented in addition to their corresponding exact results calculated using (13). It can be observed that (18) offers an accurate approximation to the exact TFC CIR expression (13).

Next, the accuracy of the approximation with various configurations is evaluated. The NMSE of the CIR approximation is calculated, which is defined as:

$$e_{\mathrm{nmse}} = \frac{\mathbb{E}_t\left[\left(\hat{h}(t)-h(t)\right)^2\right]}{\mathbb{E}_t\left[h^2(t)\right]}, \tag{B.2}$$

where $\hat{h}(t)$ denotes the approximated CIR result. Fig. 19 shows results of NMSE varies with $\tilde{r}/z_s$ and with $\phi_{1/2}$. It can be observed that with most of the configurations, the NMSE is negligible. With an increase of $\tilde{r}/z_s$ and a decrease of $\phi_{1/2}$, the resulting NMSE increases. In the case that $\phi_{1/2}$ is smaller than 30° and $\tilde{r}/z_s$ is greater than 2, the approximation becomes inaccurate. However, the magnitude of the CIR itself in this extreme case is significantly small. Consequently, these inaccurate components contribute little to the final TFCR calculation in (27). Therefore, this approximation error will not significantly affect the accuracy of the CIR calculation of the TFCR category.

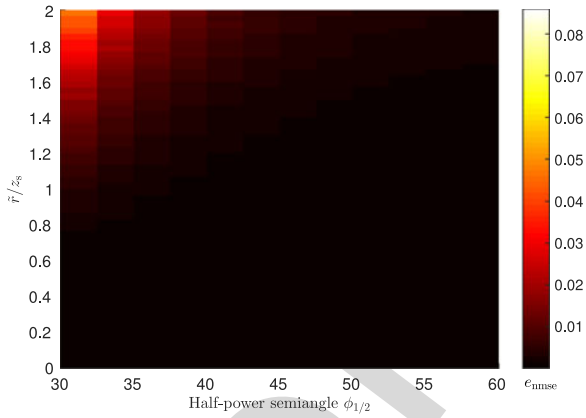

Fig. 19. NMSE of the approximation in (18) with various $\tilde{r}/z_s$ and $\phi_{1/2}$.

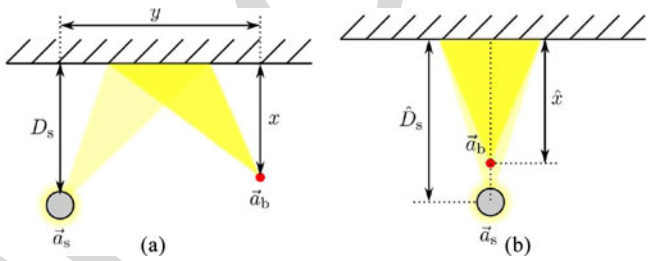

Fig. 20. (a) TWC channel geometry with $y\neq 0$ m. (b) Approximated TWC channel geometry with $y=0$ m, $\hat{D}_s$ and $\hat{x}$.

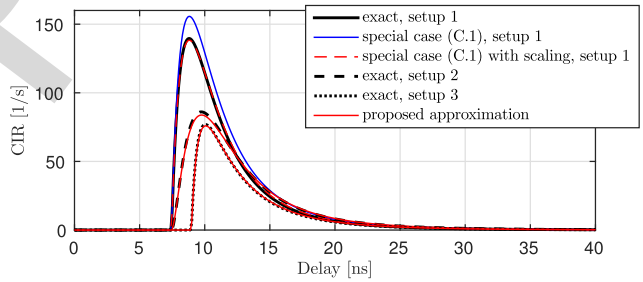

Fig. 21. An example of the comparison between the exact and approximated TWC CIR results. Setup 1: $D_s=1$ m, $x=1$ m, $y=1$ m, $\phi_{1/2}=60^\circ$. Setup 2: $D_s=1$ m, $x=1$ m, $y=1$ m, $\phi_{1/2}=40^\circ$. Setup 3: $D_s=2$ m, $x=0.5$ m, $y=1$ m, $\phi_{1/2}=60^\circ$. The results of the approximated curves are also shown in this figure. Setup 1 is used to demonstrate the approximation method.

APPENDIX C
APPROXIMATION IN (32)

In this appendix, the approximation used in (32) is demonstrated, and the accuracy of the approximation with various parameters is evaluated. Firstly, the spacial case of (28) with $y=0$ m is considered. By making $y=0$ m, (28) can be rearranged as:

$$\begin{aligned}\mathrm{d}h^{\vec{a}_b}_{\mathrm{twc},y=0}(t,D_s,x) &= \hbar^{[0,1,0],[0,1,0]}_{\{m,\mathrm{d}A,\rho_w,D_s,x,0,90^\circ\}}(t)\\ &= \frac{\rho_w D_s x\mathcal{B}\left(\frac{m+2}{2},\frac{m+2}{2}\right)2^m\mathfrak{r}^2_{\mathrm{twc}}(t)\mathrm{d}A\mathcal{U}\left(t-\frac{D_s+x}{c}\right)}{\frac{\pi^2 t}{m+1}\left(1+\frac{D_s^2}{\mathfrak{r}^2_{\mathrm{twc}}(t)}\right)^{\frac{m-1}{2}}\left(\frac{c^2t^2}{4}-\frac{(D_s^2-x^2)^2}{4c^2t^2}\right)^3},\end{aligned} \tag{C.1}$$

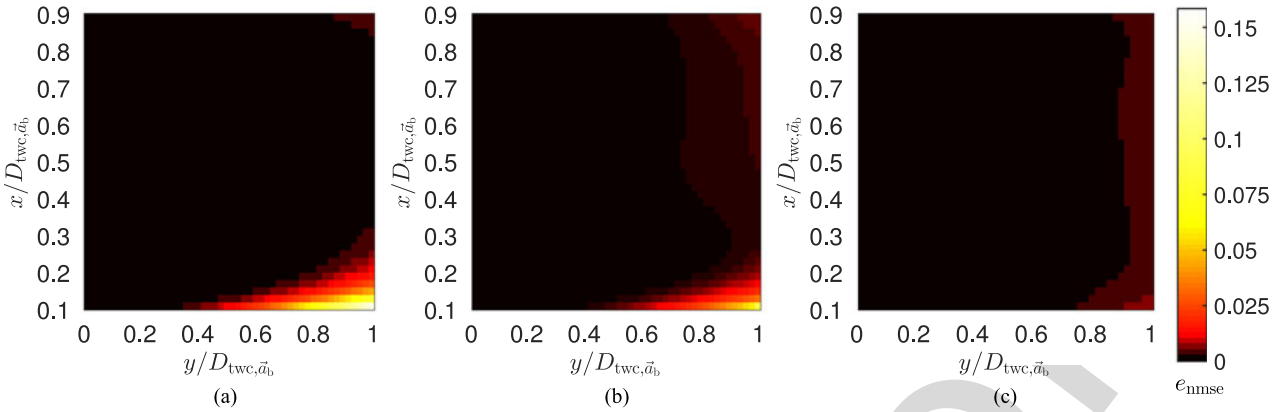

Fig. 22. NMSE of the approximation in (32) with various $y/D_{\mathrm{twc},\vec{a}_b}$ and $x/D_{\mathrm{twc},\vec{a}_b}$. (a) $\phi_{1/2} = 20°$. (b) $\phi_{1/2} = 40°$. (c) $\phi_{1/2} = 60°$.

where

$$\mathfrak{r}^2_{\mathrm{twc}}(t) = \frac{c^2t^2}{4} + \frac{\left(D_s^2 - x^2\right)^2}{4c^2t^2} - \frac{D_s^2 + x^2}{2}. \tag{C.2}$$

This special case expression (C.1) is significantly simplified and in closed form compared to the general case TWC CIR expression (28). Therefore, we use (C.1) as a base function to develop an expression to approximate (28). Considering a TWC channel in a general case with $y \neq 0$, the top view of the channel geometry is shown in Fig. 20(a). It is intuitive to find that the length of the shortest propagation path is $D_{\mathrm{twc},\vec{a}_b} = \sqrt{(D_s + x)^2 + y^2}$. Now we want to use the special case channel with $y = 0$ m to approximate the general case TWC channel as shown in Fig. 20(b). In order to achieve the correct minimum delay control, the minimum transmission distance in the approximated model should be the same as that in the original model, which means $D_{\mathrm{twc},\vec{a}_b} = \hat{D}_s + \hat{x}$ should be fulfilled. It has been found that by adjusting the values of $\hat{D}_s$ to $\hat{x}$, the curve shape of the function (C.1) can be manipulated to be similar to that of the corresponding exact TWC CIR (28). Due to the difference in the incident (radiant) angles to (from) the wall in the exact and approximated TWC channel, the magnitude of the approximated CIR is different from the exact result. Therefore, a scaling factor $\mathcal{F}_{\mathrm{twc}}$ is required. Thus, the approximated CIR can be written as:

$$\mathrm{d}h^{\vec{a}_b}_{\mathrm{twc}}(t) \approx \mathcal{F}_{\mathrm{twc}} \mathrm{d}h^{\vec{a}_b}_{\mathrm{twc},y=0}\left(t, \hat{D}_s, \hat{x}\right). \tag{C.3}$$

Next, we use an example to demonstrate the considered approximation. In this example, $D_s = 1$ m, $x = 1$ m, $y = 1$ m and $\phi_{1/2} = 60°$. The remaining parameters are the same as those listed in Table I. The CIR result calculated using (28) is shown in Fig. 21. In addition, the CIR result calculated using the base function (C.1) with $\hat{D}_s = 1.118$ m and $\hat{x} = 1.118$ m is presented. It can be observed that the two curves are similar in shape but with a slight difference in magnitude as shown in Fig. 21. By multiplying the CIR result calculated using (C.1) with a factor of 0.8882, the scaled result shows a very close approximation to the exact TWC CIR curve. This example shows the possibility of using the proposed expression (C.3) to achieve accurate approximation. Appropriate functions for the calculation of $\hat{D}_s$, $\hat{x}$ and $\mathcal{F}_{\mathrm{twc}}$ are important for the accuracy of the approximation. By using curve fitting tools, expressions (34), (35) and (36) have been found to provide acceptable accuracy. In Fig. 21, another two examples calculated using (32) are demonstrated. Both approximated results are close to the corresponding exact TWC CIR results calculated using (28).

Then, the accuracy of the approximation using (32) with various configurations is evaluated. The NMSE for various configurations defined by (B.2) in Appendix B is calculated. The results of NMSE varies with $y/D_{\mathrm{twc},\vec{a}_b}$ and $x/D_{\mathrm{twc},\vec{a}_b}$ in the case of $\phi_{1/2} = 20°, 40°, 60°$ are shown in Fig. 22. It shows that with majority of the configurations, the NMSE level is negligible. It is noted that in the case of $y/D_{\mathrm{twc},\vec{a}_b}$ is significant and $x/D_{\mathrm{twc},\vec{a}_b}$ is very close to zero, the NMSE starts to increase, especially when $\phi_{1/2}$ is small.

REFERENCES

[1] S. Dimitrov and H. Haas, *Principles of LED Light Communications: Towards Networked Li-Fi*. Cambridge , U.K.: Cambridge Univ. Press, 2015.
[2] D. Tsonev *et al.*, "A 3-Gb/s single-LED OFDM-based wireless VLC link using a gallium nitride μLED," *IEEE Photon. Technol. Lett.*, vol. 26, no. 7, pp. 637–640, Apr. 2014.
[3] A. M. Khalid, G. Cossu, R. Corsini, P. Choudhury, and E. Ciaramella, "1-Gb/s transmission over a phosphorescent white LED by using rate-adaptive discrete multitone modulation," *IEEE Photon. J.*, vol. 4, no. 5, pp. 1465–1473, Oct. 2012.
[4] J. Barry, J. Kahn, W. Krause, E. Lee, and D. Messerschmitt, "Simulation of multipath impulse response for indoor wireless optical channels," *IEEE J. Sel. Areas Commun.*, vol. 11, no. 3, pp. 367–379, Apr. 1993.
[5] G. R. Maccartney, T. S. Rappaport, S. Sun, and S. Deng, "Indoor office wideband millimeter-wave propagation measurements and channel models at 28 and 73 GHz for ultra-dense 5G wireless networks," *IEEE Access*, vol. 3, pp. 2388–2424, Oct. 2015.
[6] T. Komine and M. Nakagawa, "Fundamental analysis for visible-light communication system using LED lights," *IEEE Trans. Consum. Electron.*, vol. 50, no. 1, pp. 100–107, Feb. 2004.
[7] J. Grubor, S. Randel, K. Langer, and J. W. Walewski, "Broadband information broadcasting using LED-Based interior lighting," *IEEE J. Lightw. Technol.*, vol. 26, no. 24, pp. 3883–3892, Dec. 2008.
[8] F. J. Lopez-Hermandez and M. J. Betancor, "DUSTIN: Algorithm for calculation of impulse response on IR wireless indoor channels," *Electron. Lett.*, vol. 33, no. 21, pp. 1804–1806, Oct. 1997.
[9] F. Lopez-Hernandez, R. Perez-Jimenez, and A. Santamaria, "Ray-tracing algorithms for fast calculation of the impulse response on diffuse IR-wireless indoor channels," *Opt. Eng.*, vol. 39, no. 10, pp. 2775–2780, Oct. 2000.

IEEE PROOF

[10] V. Jungnickel, V. Pohl, S. Nonnig, and C. von Helmolt, "A physical model of the wireless infrared communication channel," *IEEE J. Sel. Areas Commun.*, vol. 20, no. 3, pp. 631–640, Apr. 2002.
[11] K. Lee, H. Park, and J. Barry, "Indoor channel characteristics for visible light communications," *IEEE Commun. Lett.*, vol. 15, no. 2, pp. 217–219, Feb. 2011.
[12] P. Chvojka, S. Zvanovec, P. A. Haigh, and Z. Ghassemlooy, "Channel characteristics of visible light communications within dynamic indoor environment," *J. Lightw. Technol.*, vol. 33, no. 9, pp. 1719–1725, May 2015.
[13] F. Miramirkhani and M. Uysal, "Channel modeling and characterization for visible light communications," *IEEE J. Photon.*, vol. 7, no. 6, pp. 1–16, Dec. 2015.
[14] L. Zeng *et al.*, "High data rate multiple input multiple output (MIMO) optical wireless communications using white LED lighting," *IEEE J. Sel. Areas Commun.*, vol. 27, no. 9, pp. 1654–1662, Dec. 2009.
[15] Y. Wang, S. Videv, and H. Haas, "Dynamic load balancing with handover in hybrid Li-Fi and Wi-Fi networks," in *Proc. Symp. Pers. Indoor Mobile Radio Commun.*, Sep. 2014, pp. 548–552.
[16] J. B. Carruthers and J. M. Kahn, "Modeling of nondirected wireless infrared channels," *IEEE Trans. Commun.*, vol. 45, no. 10, pp. 1260–1268, Oct. 1997.
[17] C. Chen, D. Basnayaka, and H. Haas, "Non-line-of-sight channel impulse response characterisation in visible light communications," in *Proc. IEEE Int. Conf. Commun.*, Kuala Lumpur, Malaysia, May 2016, pp. 1–6.
[18] J. M. Kahn, W. J. Krause, and J. B. Carruthers, "Experimental characterization of non-directed indoor infrared channels," *IEEE Trans. Commun.*, vol. 43, no. 234, pp. 1613–1623, Feb.–Apr. 1995.
[19] *Lighting of Indoor Work Places*, European Standard EN 12464-1, Jan. 2009.
[20] "Kingbali high backlight reflective paper." [Online]. Available: http://www.kingbali.com
[21] F. R. Gfeller and U. Bapst, "Wireless in-house data communication via diffuse infrared radiation," *Proc. IEEE*, vol. 67, no. 11, pp. 1474–1486, Nov. 1979.
[22] F. J. Lopez-Hernandez, R. Perez-Jimenez, and A. Santamara, "Ray-tracing algorithms for fast calculation of the channel impulse response on diffuse IR wireless indoor channels," *Opt. Eng.*, vol. 39, no. 10, pp. 2775–2780, 2000.
[23] C. Chen, D. A. Basnayaka, and H. Haas, "Downlink performance of optical attocell networks," *J. Lightw. Technol.*, vol. 34, no. 1, pp. 137–156, Jan. 2016.

Cheng Chen received the B.Eng. degree in electronic and electrical engineering from the University of Strathclyde, Glasgow, U.K., in 2011, the M.Sc. degree in communications and signal processing from the Imperial College, London, U.K., in 2012, and the Ph.D. degree in electrical engineering from the University of Edinburgh, Edinburgh, U.K., in 2017. He is currently employed as a Research Associate with the Li-Fi Research and Development Centre, the University of Edinburgh and is working in the field of visible light communications.

Dushyantha A. Basnayaka (S'11–M'12) received the B.Sc. Eng. degree (Hons.) in 2006, and the Ph.D. degree in electrical and electronics engineering, in 2012. He is currently with the Institute for Digital Communications, the University of Edinburgh, Edinburgh, U.K. His current research interests include multiple-input multiple-output, index modulation, the physical layer aspects of internet-of-things (IoT), coordinated multipoint systems (CoMP), and visible light communication systems. He holds two patents (one granted and one pending) in CoMP, and IoT. He was a recipient of the University of Canterbury International Doctoral Scholarship from 2009 to 2012, and the Best Paper Award at the 2015 IEEE Vehicular Technology Conference.

Xiping Wu (S'11–M'14) received the B.Sc. degree from Southeast University, Nanjing, China, in 2008, the M.Sc. degree (Hons.) and the Ph.D. degree from the University of Edinburgh, Edinburgh, U.K., in 2011 and 2015, respectively. From 2011 to 2014, he was a Marie-Curie Early-Stage Researcher, funded by the European Unions Seventh Framework Program (FP7) Project GREENET. From 2013 to 2014, he was on secondment to the Department of Electrical and Information Engineering, University of LAquila, LAquila, Italy. He is currently a Research Associate with the Institute for Digital Communications with the University of Edinburgh, funded by the British Engineering and Physical Sciences Research Council Project TOUCAN. His main research interests include wireless communication theory, visible light communications, and wireless network management. He was a recipient of the Scotland Saltire Scholarship by the Scottish Government in 2010.

Harald Haas (S'98–AM'00–M'03–SM'17) received the Ph.D. degree from the University of Edinburgh, Edinburgh, U.K., in 2001. He currently holds the Chair of Mobile Communications, the University of Edinburgh, and is the initiator, cofounder, and Chief Scientific Officer with pureLiFi Ltd., as well as the Director of the LiFi Research and Development Center, the University of Edinburgh. His main research interests include optical wireless communications, hybrid optical wireless and RF communications, spatial modulation, and interference coordination in wireless networks. He first introduced and coined spatial modulation and LiFi. LiFi was listed among the 50 best inventions in TIME Magazine 2011. He was an invited speaker at TED Global 2011, and his talk: Wireless Data from Every Light Bulb has been watched online more than 2.4 million times. He gave a second TED Global lecture in 2015 on the use of solar cells as LiFi data detectors and energy harvesters. This has been viewed online more than 1.8 million times. He authored or coauthored more than 400 conference and journal papers including a paper in Science. He coauthors a book entitled: *Principles of LED Light Communications Towards Networked Li-Fi* (Cambridge University Press, 2015). He is the Editor of the IEEE TRANSACTIONS ON COMMUNICATIONS and IEEE JOURNAL OF LIGHTWAVE TECHNOLOGIES. He was corecipient of recent best paper awards at VTC-Fall, 2013, VTC-Spring 2015, ICC 2016, and ICC 2017. He was corecipient of the EURASIP Best Paper Award for the *Journal on Wireless Communications and Networking* in 2015, and corecipient of the Jack Neubauer Memorial Award of the IEEE Vehicular Technology Society. In 2012 and 2017, he was the recipient of the prestigious Established Career Fellowship from the EPSRC (Engineering and Physical Sciences Research Council) within Information and Communications Technology in U.K. In 2014, he was selected by EPSRC as one of ten RISE (Recognising Inspirational Scientists and Engineers) Leaders in U.K. In 2016, he received the outstanding achievement award from the International Solid State Lighting Alliance. He was elected a Fellow of the Royal Society of Edinburgh in 2017.

IEEE Proof

GENERAL INSTRUCTIONS

- Authors: When accessing and uploading your corrections at the Author Gateway, please note we cannot accept new source files as corrections for your paper. Do not send new Latex, Word, or PDF files, as we cannot simply "overwrite" your paper. Please submit your corrections as an annotated PDF or as clearly written list of corrections, with location in paper, using line numbers provided on your proof. You can also upload revised graphics to the Gateway.
- Authors: Please note that once you click "approve with no changes," the proofing process is now complete and your paper will be sent for final publication and printing. Once your paper is posted on Xplore, it is considered final and the article of record. No further changes will be allowed at this point so please ensure scrutiny of your final proof.
- Authors: Unless invited or otherwise informed, overlength page charges of $260 per page are mandatory for each page in excess of seven printed pages and are required for publication. If you have any questions regarding overlength page charges, need an invoice, or have any other billing questions, please contact reprints@ieee.org as they handle these billing requests.

QUERIES

Q1. Author: There was a discrepancy between source file and pdf. We have followed the source file.

Q2. Author: Please provide the year for Ref. [20].

IEEE Proof

Efficient Analytical Calculation of Non-Line-of-Sight Channel Impulse Response in Visible Light Communications

Cheng Chen, *Student Member, IEEE*, Dushyantha A. Basnayaka, *Member, IEEE*, Xiping Wu, *Member, IEEE*, and Harald Haas, *Senior Member, IEEE*

***Abstract*—This study provides an analytical method to calculate the non-line-of-sight (NLoS) channel impulse response (CIR) in visible light communication (VLC) systems based on intensity modulation and direct detection (IM/DD). In this method, the NLoS channel is decomposed into a number of components with different propagation categories. These propagation categories are defined according to the number of reflections and the reflective surfaces that the light undergoes. The CIR corresponding to each light propagation category is analysed, and the overall NLoS CIR is approximated by the combination of the calculated CIR components in different propagation categories. The proposed method poses the major advantage of offering accurate results with very low computational complexity. Typically, a NLoS CIR with a time resolution of 0.1 ns can be generated within a second in MATLAB. Furthermore, the derived analytical results could be used as an analytical tool for the VLC channel characterisation study in future research.**

***Index Terms*—Channel impulse response, computational complexity, non-line-of-sight channel (NLoS), visible light communications.**

I. Introduction

With the emergence of 'smart' devices and the increase in wireless Internet access demand, the existing radio frequency (RF) spectrum resources will no longer fulfil the requirement of the future wireless data traffic. In order to avoid the potential spectrum crisis, many technologies using higher frequency spectrum resources have been considered by researchers. Visible light communication (VLC) is one such technique. The main idea of VLC is to convert the existing light sources into wireless access points to provide wireless communication functionality [1]. Many experimental studies have demonstrated that single-link light-emitting diode (LED)-based VLC systems can achieve data rates in the scope of Gbps [2], [3]. In addition to the feature of high transmission capability, many unique characteristics of VLC, such as improved security, license-free spectrum, make it a promising technology for various future applications.

Many studies on indoor optical wireless have shown that the effects of a non-line-of-sight (NLoS) channel also plays an important role in VLC systems [4]. In RF communications (microwave, millimetre-wave), the NLoS paths are normally formed by the effects of specular reflections, diffractions by surrounding objects. Therefore, the channel impulse response (CIR) of the signal via these NLoS paths shows multiple 'spikes' with discrete delays. The strength of these 'spikes' is dominated by the transmitter-receiver separation, which can normally be characterised by a free-space path loss (FSPL)-based model [5]. In contrast, the NLoS channels in VLC systems are normally caused by diffused reflections due to the smaller wavelength of visible light. This phenomenon creates a countless number of reflection paths, and the corresponding CIR shows as a continuous waveform. The characteristics of this continuous CIR depends not only on transmitter-receiver separation, but also on many other parameters such as orientation and reflectivity. Consequently, a simple FSPL model is unable to characterise the NLoS channel.

Low-cost LEDs and photodiodes (PDs) are typically used in both wireless infrared (IR) communication systems and VLC systems. In addition, the signal propagation characteristics in wireless IR and VLC systems are similar as both systems use adjacent optical spectrum. Consequently, a number of methods developed for simulating wireless IR communication channels can be used for VLC studies [6], [7]. A widely used deterministic NLoS CIR calculation method has been proposed in [4]. In this method, a cuboid room with internal surfaces causing diffused reflections is considered. The internal surfaces are divided into a large number of small reflecting elements. With the given locations and orientations of the transmitter and receiver, an accurate CIR result can be obtained by calculating the interaction between each pair of elements. The main drawback of this approach is its extremely high computational complexity. It takes several days to calculate a CIR result for a small room considering up to 3rd order reflections with a moderate time resolution. In order to reduce the computation time, improved methods based on the DUSTIN algorithm [8] and the Monte Carlo simulation [9] have been proposed. Both methods reduce the computation time significantly. Especially for

Manuscript received August 26, 2016; revised June 27, 2017 and November 15, 2017; accepted December 2, 2017. This work was supported by the Engineering and Physical Sciences Research Council (EPSRC) under Grant EP/L020009/1: Towards Ultimate Convergence of All Networks (TOUCAN). The work of H. Haas was supported by EPSRC under Established Career Fellowship Grant EP/K008757/1. *(Corresponding author: Cheng Chen.)*

The authors are with the Li-Fi Research and Development Centre, Institute for Digital Communications, The University of Edinburgh, Edinburgh EH9 3JL, U.K. (e-mail: cheng.chen@ed.ac.uk; d.basnayaka@ed.ac.uk; xiping.wu@ed.ac.uk; h.haas@ed.ac.uk).

Color versions of one or more of the figures in this paper are available online at http://ieeexplore.ieee.org.

Digital Object Identifier 10.1109/JLT.2017.2786459

IEEE Proof

0733-8724 © 2017 IEEE. Personal use is permitted, but republication/redistribution requires IEEE permission.
See http://www.ieee.org/publications_standards/publications/rights/index.html for more information.

the Monte Carlo method, an accurate CIR result can be obtained within a period of several minutes. A physical model of the IR channel using a sphere environment approximation has been proposed in [10] to approximate the frequency response of NLoS channels. It has been pointed out in [11] that since a typical incoherent visible light source has a broad optical spectrum, the methods developed in wireless IR communications cannot be directly used in VLC channel calculation. The dependency on light wavelength is considered in the deterministic CIR calculation method for the CIR calculation in VLC [11]. User mobility is taken into account in [12]. VLC channel characterisations based on the commercial optical design software Zemax is considered in [13]. Most of the aforementioned studies of VLC channel modelling offer results for special configurations, where generalisations are not straightforward.

In some VLC studies, such as multiple-input multiple-output (MIMO) in VLC [14] or networked VLC [15], a large number of channel samples are required to evaluate the system performance. If the deterministic or Monte Carlo method is used to generate the channel with NLoS components, it would take a considerable amount of time over many years. The channel model considering only line-of-sight (LoS) propagation is widely used because the VLC channel is generally dominated by the LoS path and the calculation has a very low computational complexity. An analytical closed-form expression for a NLoS CIR with a ceiling-bounce model in a diffused IR link has been derived in [16]. Motivated by this approach, in this study, we extend the work in [16] and propose an analytical method to calculate the NLoS CIR for VLC links. The current paper is an extended version of the previous study in [17]. Firstly, we decompose the complicated NLoS channel into a number of components with less-complicated light propagation categories. These propagation categories are defined according to the number of reflections and the reflective surfaces that the light undergoes. Secondly, the analysis of the channel with each category is carried out, and the corresponding CIR analytical expressions are obtained. Finally, the overall CIR is approximated as a superposition of these CIRs for each category. It is shown in this paper that the proposed method provides an efficient tight approximation for NLoS VLC CIRs considering up to 2nd order reflections.

The remainder of this paper is arranged as follows. The analysis methodology presented in this study is introduced in Section II. A preliminary single reflection CIR calculation is introduced in Section III. The detailed analysis of the component NLoS CIRs and the corresponding analytical results are presented in Section IV. The final approximated overall NLoS CIR calculation is presented in Section V. In addition, the calculation accuracy and computation time is evaluated and compared with the state-of-the-art method in this section. Conclusions are drawn in Section VI.

II. Non-Line-of-Sight Channel Analysis Methodology

In this section, the methodology of the proposed approach to analyse the NLoS channel in typical indoor environments such as cuboid rooms is presented. Multi-path reflections caused by internal surfaces inflict major NLoS channel components. It is assumed that the room's internal surfaces cause diffused reflections with fixed reflectance. In addition, a transmitter and a receiver are defined with specified locations. In this study, we are interested in calculating the normalised optical CIR. In the CIR calculation, we consider the detected optical power at each time instant on the receiver PD detector with a unity optical power radiated from the transmitter optical source. Without loss of generality, the optical CIR is normalised by time. This metric has also been used in many other publications [4], [18]. Note that an incoherent light source is assumed to be used. Therefore, the power of the optical signals can be incoherently added in the CIR calculation as the phases of optical signals are uncorrelated.

For the convenience of analysis, the entire NLoS CIR can be decomposed into multiple components with respect to the number of reflections occurred as:

$$h_{\mathrm{NLoS}}(t) = \sum_{\mathrm{i}=1}^{\infty} h^{[\mathrm{i}]}(t), \tag{1}$$

where $h^{[\mathrm{i}]}(t)$ represents the component CIR with light undergoing exactly i reflections. Despite the decomposition according to the number of reflections, the complexity of each component is still too high to conduct tractable analysis. In order to further decrease the analytical complexity, each component CIR $h^{[i]}(t)$ is further decomposed according to the light propagation category. A number of major light propagation categories are considered in this study.

In the case of $h^{[1]}(t)$, there is only one propagation category: light travels from the transmitter to one of the four walls, and after the reflection it continues to propagate to the receiver, as shown in Fig. 1(a). This light propagation category is called the transmitter-to-wall-to-receiver (TWR). For the channel of this category, the signal only interacts with a single surface. Consequently, the relationship between the geometric characteristics and the time delay characteristics of the channel is tractable for analysis as demonstrated in [16]. In the case of $h^{[2]}(t)$, light propagation between different surfaces exists. The different combinations of these propagations between different surfaces lead to four light propagation categories as shown in Fig. 1(b), (c), (d) and (e). For example, in one of the categories, the emitted light from the transmitter propagates via the floor and ceiling and incidents to the receiver. For convenience, this category is called the transmitter-to-floor-to-ceiling-to-receiver (TFCR). Similarly, the other three categories are the transmitter-to-wall-to-ceiling-to-receiver (TWCR), the transmitter-to-wall-to-wall-to-receiver (TWWR) and the transmitter-to-floor-to-wall-to-receiver (TFWR) categories. The analytical complexity of these categories is higher than that of TWR as the CIR calculation of these categories requires integrations over two surfaces. However, it is demonstrated that via appropriate approximations and simplifications, analytical CIR expressions can be obtained for several dominant categories. The resulting expressions have one or two one-dimensional (1-D) integrations with finite limits. The channel categories due to higher order reflections can also be defined in a similar manner, but are omitted due to the exponential growth of analytical complexity as the order of

IEEE Proof

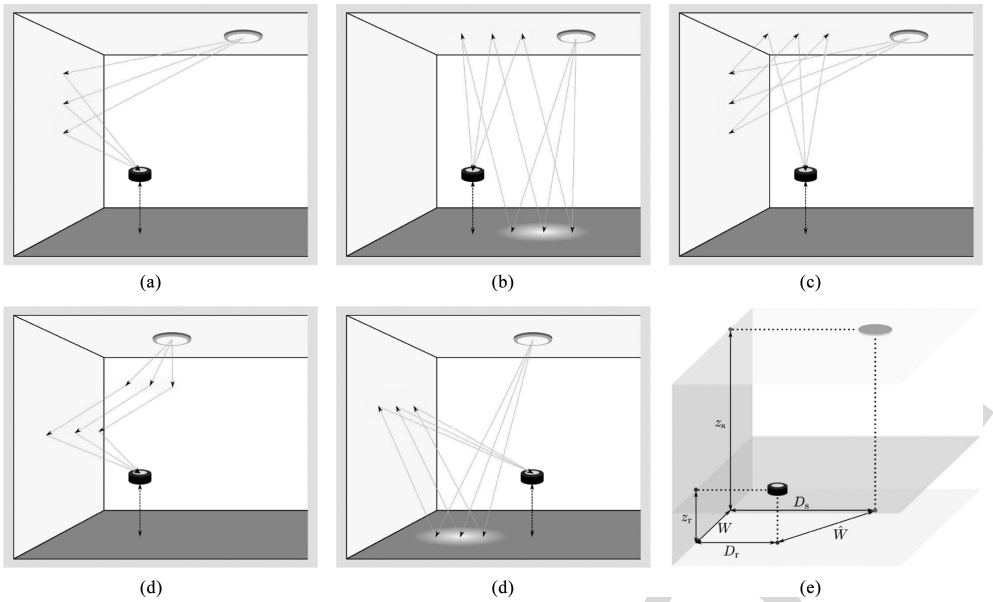

Fig. 1. (a) Light propagation in transmitter-to-wall-to-receiver case. (b) Light propagation in transmitter-to-floor-to-ceiling-to-receiver case. (c) Light propagation in transmitter-to-wall-to-ceiling-to-receiver case. (d) Light propagation in transmitter-to-wall-to-wall-to-receiver case. (e) Light propagation in transmitter-to-floor-to-wall-to-receiver case. (f) The notations of important geometric parameters.

reflections increases. Fortunately, it is shown in the final results that the omission of these higher order reflection components causes an acceptable loss in accuracy.

Ideally, the entire NLoS CIR should be the superposition of the CIR components considering all propagation categories. However, the channel with some categories is so complex that the corresponding expression is unavailable. Therefore, the superposition of the CIRs with part of the categories that dominate the NLoS channel is used to approximate the overall NLoS CIR. In this paper, the expressions for the CIR with TWR, TFCR and TWCR categories are derived and used to estimate the NLoS CIR. For the case of TFWR, the channel interacts with the wall and the floor. Therefore, the CIR is only perceivable when the link is next to one of the walls. In addition, the reflectivity of floor is typically low (0.2 to 0.4 [19]), which further decreases the significance of the channel of TFWR category. For the case of TWWR, the CIR is only perceivable when the link is next to one of the room corners. As long as the room is not small, this condition can be treated as a minor case. The power of the channels caused by high order reflections is expected to be low due to the significant path loss. Because of these reasons, the omission of the TFWR channel, the TWWR channel and other channels due to higher order reflections are expected to cause minor error in the NLoS CIR estimation. The analysis of the reflection and obstruction caused by other opaque objects, such as human bodies or furniture, is complicated, and many characteristics of these effects have not been investigated yet. Therefore, the impact of these issues are not considered.

III. Preliminary

In this section, a NLoS channel with a single diffused reflection by an infinite plane is considered. A closed-form expression for calculating the impulse response of this link in a special case is presented in [16]. However, the CIR analytical result for the general case will be frequently used in the CIR analysis of various categories in Section IV in this paper. For the convenience of the following analysis, we extend the work in [16] and present the expression for the general case here.

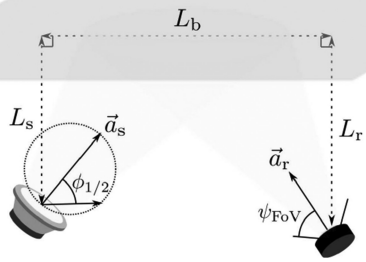

Fig. 2. The deployment of a single reflection light propagation channel.

Fig. 2 shows the setup for a single reflection channel. A light source with a Lambertian emission order of m and an orientation of $\vec{o}_s = [\tilde{x}_s, \tilde{y}_s, \tilde{z}_s]$ is L_s away from the plane. The Lambertian emission order m determines the radiation pattern of the light source, which is related to the light source half-power semiangle $\phi_{1/2}$ by $m = -1/\log_2(\cos(\phi_{1/2}))$. A receiving element with a physical area of A_r and an orientation of $\vec{o}_r = [\tilde{x}_r, \tilde{y}_r, \tilde{z}_r]$ is L_r away from the plane. Both the light source and the receiving element have the projection points on the plane. The distance between the two projection points is L_b. The effective reflectivity of the surface is ρ. The field of view (FoV) of the receiving element is ψ_FoV. The CIR for this single reflection link is concluded in the following proposition.

Proposition 1: With specified values for m, A_r, ρ, L_s, L_r, L_b, $\vec{o}_s$, $\vec{o}_r$ and ψ_FoV, the impulse response for a single reflection

channel can be calculated as:

$$\hbar^{\vec{o}_s,\vec{o}_r}_{\{m,A_r,\rho,L_s,L_r,L_b,\psi_{\rm FoV}\}}(t) = \frac{\rho(m+1)L_sL_rA_r}{2\pi^2} \times \mathcal{U}\left(t-\frac{L_0}{c}\right)\int_0^{2\pi} \mathfrak{r}_\theta(t)\mathfrak{f}(\mathfrak{r}_\theta(t),\theta)\frac{\mathrm{d}\mathfrak{r}_\theta(t)}{\mathrm{d}t}\mathrm{d}\theta, \quad (2)$$

where

$$\mathfrak{f}(r,\theta) = \left(r\left(\tilde{x}_s\cos\theta+\tilde{y}_s\sin\theta\right)+\frac{L_sL_b\tilde{x}_s}{L_s+L_r}+L_s\tilde{z}_s\right)^m \times \left(r\left(\tilde{x}_r\cos\theta+\tilde{y}_r\sin\theta\right)-\frac{L_rL_b\tilde{x}_r}{L_s+L_r}+L_r\tilde{z}_r\right)\mathbf{1}_{\rm FoV} \times \left(r^2+\frac{2L_sL_br\cos\theta}{L_s+L_r}+L_s^2+\frac{L_s^2L_b^2}{(L_s+L_r)^2}\right)^{-\frac{m+3}{2}} \times \left(r^2-\frac{2L_rL_br\cos\theta}{L_s+L_r}+L_r^2+\frac{L_r^2L_b^2}{(L_s+L_r)^2}\right)^{-2}, \quad (3)$$

$$\mathfrak{r}_\theta(t) = \frac{ct\sqrt{\mathfrak{c}_\theta(t)}-\left(c^2t^2-L_0^2\right)(L_s-L_r)L_b\cos\theta}{2\left(c^2t^2-L_b^2\cos^2\theta\right)(L_s+L_r)}, \quad (4)$$

$$\frac{\mathrm{d}\mathfrak{r}_\theta(t)}{\mathrm{d}t} = \frac{2c^2tL_b\cos\theta(L_s-L_r)\left(L_b^2\cos^2\theta-L_0^2\right)}{2(L_s+L_r)\left(c^2t^2-L_b^2\cos^2\theta\right)^2} - \frac{c\left(c^2t^2+L_b^2\cos^2\theta\right)\sqrt{\mathfrak{c}_\theta(t)}}{2(L_s+L_r)\left(c^2t^2-L_b^2\cos^2\theta\right)^2} + \frac{c^3t^2(L_s-L_r)^2\left(c^2t^2-L_0^2\right)}{(L_s+L_r)\left(c^2t^2-L_b^2\cos^2\theta\right)\sqrt{\mathfrak{c}_\theta(t)}} + \frac{2c^3t^2L_sL_r\left(2c^2t^2-L_0^2-L_b^2\cos^2\theta\right)}{(L_s+L_r)\left(c^2t^2-L_b^2\cos^2\theta\right)\sqrt{\mathfrak{c}_\theta(t)}}, \quad (5)$$

$$L_0 = \sqrt{L_b^2+(L_s+L_r)^2}, \quad (6)$$

$$\mathfrak{c}_\theta(t) = 4L_sL_r\left(c^2t^2-L_b^2\cos^2\theta\right)\left(c^2t^2-L_0^2\right) + (L_s-L_r)^2\left(c^2t^2-L_0^2\right)^2. \quad (7)$$

Proof: The basic idea of this proposition is given as follows. Each light ray is reflected by a point on the reflection plane. The location of the point is defined by a polar coordinate system (r,θ). Firstly, the differential of the channel gain via each path is calculated. Then, the light signals via the paths with the same length arrive at the receiver at the same time. The accumulation of these signals form the response at a certain time delay. The expression (3) is proportional to the channel gain via each path. The expression (4) corresponds to the reflection points that lead to the paths with the same time delay. Expression (6) corresponds to the shortest reflection path. More details about the derivation of Proposition 1 is given in Appendix A.

In Proposition 1, c represents the speed of light, $\mathcal{U}(u)$ is the the unit step function, and $\mathbf{1}_{\rm FoV}$ is an indicator function, which guarantees only the signals propagating within the FoV of receiver and light source coverage contribute to the CIR. The indicator function $\mathbf{1}_{\rm FoV}$ equals 1 if it satisfies the following conditions:

$$\frac{r(\tilde{x}_r\cos\theta+\tilde{y}_r\sin\theta)-\frac{\tilde{x}_rL_rL_b}{L_s+L_r}+\tilde{z}_rL_r}{\sqrt{r^2-\frac{2L_rL_br\cos\theta}{L_s+L_r}+L_r^2+\frac{L_r^2L_b^2}{(L_s+L_r)^2}}} \geq \cos\psi_{\rm FoV}, \quad (8)$$

$$r(\tilde{x}_r\cos\theta+\tilde{y}_r\sin\theta)+\frac{\tilde{x}_sL_sL_b}{L_s+L_r}+\tilde{z}_sL_s \geq 0, \quad (9)$$

where (8) is the condition that the incident angle is within the receiver FoV and (9) is the condition that the radiant angle is within the coverage of the light source. Note that the orientation vectors $\vec{o}_s$ and $\vec{o}_r$ are defined based on a reflection plane orientation of $[0,0,-1]$ as shown in Fig. 16 in Appendix A.

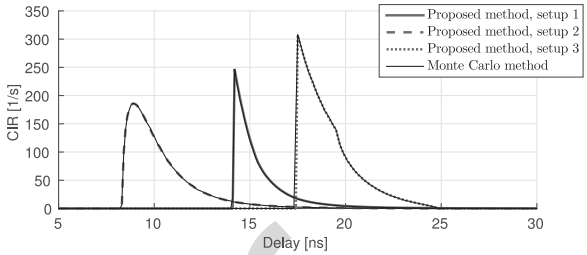

Fig. 3. Single reflection CIR results calculated using (2) and the Monte Carlo method. Configurations: $A_r = 1$ cm^2, $\rho = 0.65$. Setup 1: $\phi_{1/2} = 60°$, $\psi_{\rm FoV} = 90°$ $L_s = 2$ m, $L_r = 1$ m, $L_b = 3$ m, $\vec{o}_s = [1,0,0]$ and $\vec{o}_r = [-1,0,0]$. Setup 2: $\phi_{1/2} = 40°$, $\psi_{\rm FoV} = 90°$ $L_s = 1$ m, $L_r = 1$ m, $L_b = 1.5$ m, $\vec{o}_s = [0,0,1]$ and $\vec{o}_r = [0,1,0]$. Setup 3: $\phi_{1/2} = 60°$, $\psi_{\rm FoV} = 45°$ $L_s = 3$ m, $L_r = 2$ m, $L_b = 1.5$ m, $\vec{o}_s = [0,0,1]$ and $\vec{o}_r = [0,0,1]$.

A. Comparison With Monte Carlo Simulation Results

Fig. 3 shows three example CIRs calculated using the proposed method (2) and that using the Monte Carlo method [9] with various configurations. In the Monte-Carlo simulation, 5×10^7 iterations have been carried out for each result in this study, which is sufficient to obtain accurate results [9]. The size and the reflectance of the environment is defined in a way that is similar to the ideal condition specified for the analytical model. For example, in the single reflection channel model defined in this section, a single reflective plane with infinite size is assumed. In order to approximate this condition, a sufficiently large ceiling plane of size 50 m $\times$ 50 m is defined and the reflectivity of the remaining surfaces are set to zero. The agreement between the curves generated using (2) and that simulated using the Monte Carlo method proved the calculation accuracy of the proposed method with various link configurations.

B. Comparison With Experimental Results

In this subsection, an experiment is presented to validate the single reflection CIR analytical result. In this experiment, a LED torch (light source) and a positive-intrinsic-negative (PIN) diode detector (receiving element) are deployed next to a large board with light reflective paper causing diffused reflections, as shown in Fig. 4. Note that the measurement system used has a limited power budget to overcome the effects of noise at the detector. Therefore, we tried to adjust the experiment setup geometry to achieve a NLoS link with a higher channel gain. Both the light

IEEE Proof

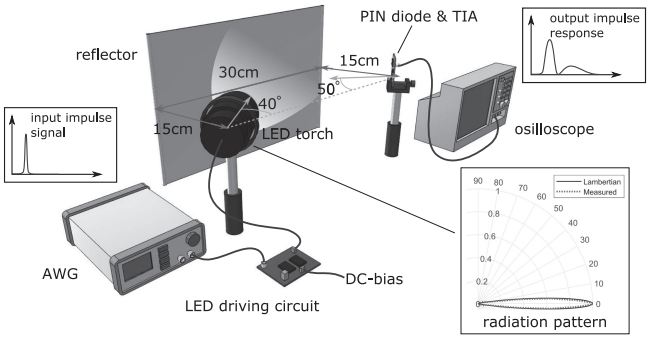

Fig. 4. Single reflection CIR calculation validation experiment setup.

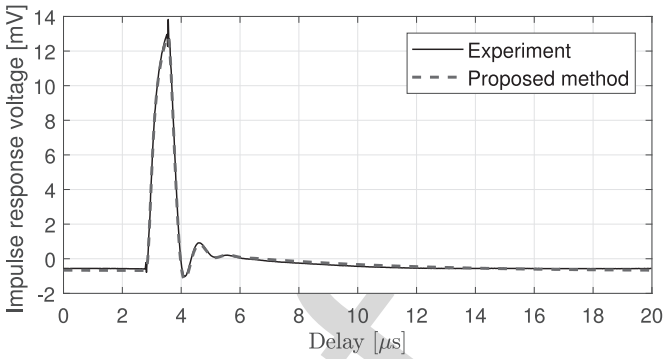

Fig. 5. Single reflection CIR results calculated using (2) and obtained in the experiment. The result calculated using (2) has been convolved with the impulse response of the measurement system.

source and the detector are positioned 15 cm away from the reflector ($L_s = L_s = 0.15$ m). The separation between the source and detector projections on the reflector is 30 cm ($L_b = 0.3$ m). The source and the detector are orientated to the same area on the reflector. Specifically, the angle between the source orientation vector $\vec{o}_s = [0.766, 0, 0.643]$ and the source / detector LoS path is 40°, as shown in Fig. 4. The angle between the detector orientation vector $\vec{o}_r = [-0.643, 0, 0.766]$ and the LoS path is 50°. The reflectance of the paper board used is 0.97 [20]. The used LED torch has a narrow beamwidth. The measured radiation pattern is presented in the bottom-right sub-plot in Fig. 4. A Lambertian pattern with a half-power semiangle of $\phi_{1/2} = 5.3°$ offers a good approximation to the measured pattern as shown in Fig. 4. Due to the use of an optical concentrator, the FoV of the PIN diode detector is decreased to 20°. Despite the fact that there is no obstruction between the source and the detector, there is no LoS transmission path in this setup due to the narrow beam of the source and the small FoV of the detector. In the experiment, an arbitrary waveform generator (AWG) is used to generate an analogue impulse signal with a pulse width of 800 ns. Via a LED driving circuit, the impulse signal is amplified and converted to a positive unipolar waveform. After the electrical-to-optical conversion via the light source and transmission through the NLoS channel, the optical signal is received by the detector and converted to a current signal. Afterwards, the current signal is amplified by a transimpedance amplifier (TIA) and the impulse response waveform is captured by an oscilloscope.

The experimental result of the single reflection channel is presented in Fig. 5. In order to mitigate the effect of noise, the oscilloscope is operated in the averaging mode. This means that the presented result is the average of 16384 detected responses. Note that the obtained experimental result also includes the impulse response of the measurement system (AWG, LED, PD, TIA). Therefore, when comparing the experimental result with the analytical result, the CIR calculated using (2) should be convolved with the impulse response of the measurement system. The measurement system impulse response can be obtained via the following process: 1) firstly, we conduct a LoS CIR measurement with the source and the detector facing each other. The separation between the source and the detector is 30 cm. The measured CIR result is denoted as $\hbar_{\mathrm{LoS}}(t)$. 2) then, we analytically calculate the LoS path loss G_{LoS}. 3) finally, the measurement system impulse response can be found as: $\hbar_{\mathrm{ms}}(t) = \hbar_{\mathrm{LoS}}(t)/G_{\mathrm{LoS}}$. The convolution of $\hbar_{\mathrm{ms}}(t)$ and the analytical result calculated using (2) is also shown in Fig. 5. It shows a close match with the experimental result, which validates the proposed method using (2). Also note that the presented results in Fig. 5 are the captured voltage signal in the AC coupling mode, where the DC component is removed from the captured signal. Therefore, the results have negative values.

IV. Detailed Analysis of Component Non-Line-of-Sight Channel Impulse Response

In this section, the CIR analysis for the channel with TWR, TFCR and TWCR categories are presented. A cuboid room with a size of $l_x \times l_y \times l_z$ is defined. The considered orientation of the light source in this study is towards the floor as this is the most common light deployment in practice. The considered orientation of the receiver PD detector is towards the ceiling. The reason for this is two-fold. Firstly, the proposed method aims at providing an efficient CIR calculation for other VLC research, and a detector orientation of directing upwards is used in many VLC studies. In addition, this configuration leads to CIR results with reasonable complexity, which is one of the research objective of this study. In practice, the fixed direction of PD detector can be achieved by using a mechanical design or by installing multiple PD detectors with different orientations on the receiver.

For the convenience of description, a number of parameters related to the positions of the transmitter and the receiver are defined. As shown in Fig. 1(f), the ceiling, the floor and one of the walls are used as references. z_s denotes the distance from the transmitter (ceiling) to the floor plane; z_r denotes the distance from the receiver to the floor plane; D_s denotes the distance from the transmitter to the wall plane; D_r denotes the distance from the receiver to the wall plane; the transmitter and the receiver have projections on the line where the floor plane and the wall plane intersect, and the distance between these two projection points is denoted as W; considering the projections of the transmitter and the receiver on the floor plane, the distance between these two projection points are denoted as $\hat{W}$. These parameters are also illustrated in Fig. 1(f).

IEEE Proof

TABLE I
DEFAULT CONFIGURATION OF THE SYSTEM PARAMETERS

Parameter	Symbol	Value
PD area / receiving area	$A_{\rm pd}$ / $A_{\rm r}$	1 $\rm cm^2$
Wall effective reflectance	$\rho_{\rm w}$	0.65
Ceiling effective reflectance	$\rho_{\rm c}$	0.8
Floor effective reflectance	$\rho_{\rm f}$	0.3
Room height	$z_{\rm s}$	3 m
Time delay step	Δt	0.1 ns

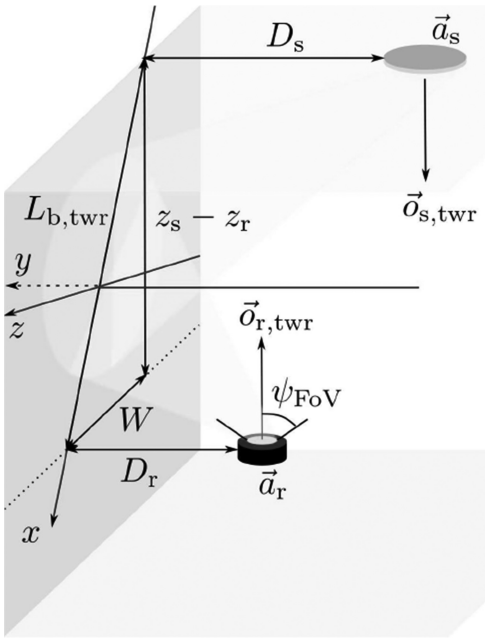

Fig. 6. Light propagation geometry in TWR category. Setup 1

The configurations of the parameters listed in Table I are used if they are not specified. Note that the selected reflectivity is based on the requirement on the reflectance of indoor internal surfaces, which is specified in [19].[1]

A. Transmitter-to-Wall-to-Receiver Channel Impulse Response (TWR)

The channel with TWR category undergoes a single reflection bounced by a wall plane, which can be treated as a special case single reflection channel as shown in Fig. 6. Therefore, the CIR of TWR category is a direct application of Proposition 1 and can be readily calculated using (2). Fig. 6 shows that the input values for L_s, L_r and L_b should be D_s, D_r and $L_{b,\rm twr}=\sqrt{W^2+(z_s-z_r)^2}$, respectively. By comparing the geometry shown in Fig. 6 and that shown in Fig. 2, it can be found that the segment between the projections of the transmitter and the receiver is tilted relative to the floor plane. As described in Section III, the orientation vectors of the transmitter and the receiver is defined based on the Cartesian coordinate system with the x direction parallel to that segment. Therefore, this tilting leads to a transformation of the transmitter and receiver orientation vectors. Note that both the orientations of the transmitter and the receiver are parallel to the wall plane. In addition,

[1]Ceiling: 0.7 to 0.9, walls 0.5 to 0.8, floor: 0.2 to 0.4.

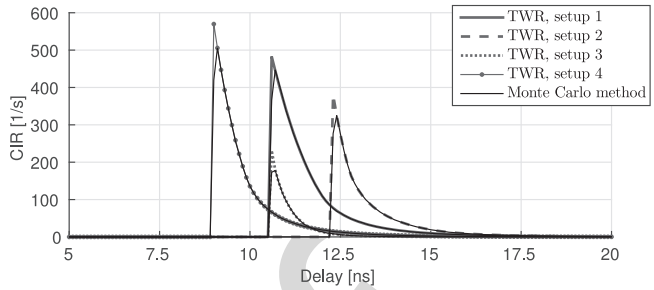

Fig. 7. NLoS CIR results with TWR category. Setup 1: $\phi_{1/2}=60^\circ$, $\psi_{\rm FoV}=90^\circ$, $D_s=1$ m, $D_r=1$ m, $W=1$ m and $z_r=0.75$ m. Compared to the configuration in setup 1, D_s, D_r, W are modified to 0.5, 2, 1.5 m in setup 2, $\phi_{1/2}$, $\psi_{\rm FoV}$ are modified to 40°, 45° in setup 3, and z_r is modified to 0.75 m in setup 4.

the tilting of the orientations depends on the ratio between W and z_s-z_r. Consequently, the transformed orientation vectors should be:

$$\vec{o}_{s,\rm twr}=\left[\frac{z_s-z_r}{L_{b,\rm twr}},\frac{W}{L_{b,\rm twr}},0\right], \tag{10}$$

$$\vec{o}_{r,\rm twr}=\left[-\frac{z_s-z_r}{L_{b,\rm twr}},-\frac{W}{L_{b,\rm twr}},0\right]. \tag{11}$$

Therefore, the expression for the CIR with TWR category can be calculated as:

$$h^{[1]}_{\rm twr}(t)=\hbar^{\vec{o}_{s,\rm twr},\vec{o}_{r,\rm twr}}_{\{m,A_{\rm pd},\rho_w,D_s,D_r,L_{b,\rm twr},\psi_{\rm FoV}\}}(t), \tag{12}$$

where ρ_w denotes the reflectance of the wall and $A_{\rm pd}$ denotes the physical area of the receiver PD detector.

Fig. 7 shows a number of CIRs in the TWR category with different setups calculated using (12). The corresponding CIR results generated using the Monte Carlo method are also presented in Fig. 7. The agreement between the CIR results generated by different methods validates the CIR calculation expression in TWR category (12).

B. Transmitter-to-Floor-to-Ceiling-to-Receiver Channel Impulse Response (TFCR)

In the TFCR channel category, the light undergoes two reflections bounced by ceiling and floor, respectively. In order to find the CIR expression for this NLoS category, a point located at $\vec{a}_b$ on the ceiling is considered as shown in Fig. 8. For the convenience of calculation, the whole space is defined by a three-dimensional (3-D) cylinder coordinate system r-θ-z. The origin is defined at the point right below the receiver on the floor. Thus, the coordinates of the point $\vec{a}_b$ can be defined as $[r,\theta,z_s]$. Firstly, we treat point $\vec{a}_b$ as a 'detector' and consider a single reflection channel from the transmitter bounced by the floor to point $\vec{a}_b$, which is defined as transmitter-to-floor-to-ceiling point (TFC) channel. In this case, the 'detector' is facing the floor and has an infinitely small physical area of $\mathrm{d}A$. Intuitively, the differential of the TFC CIR can be calculated using (2) as:

$$\mathrm{d}h^{\vec{a}_b}_{\rm tfc}(t)=\hbar^{[0,0,1],[0,0,1]}_{\{m,\mathrm{d}A,\rho_f,z_s,z_s,\tilde{r},90^\circ\}}(t), \tag{13}$$

where ρ_f denotes the reflectance of the floor and $\tilde{r}$ is the length of the segment between the projections of transmitter and receiver

IEEE Proof

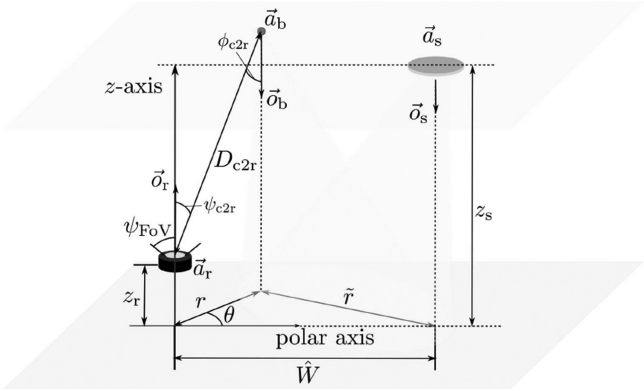

Fig. 8. Light propagation geometry in TFCR channel.

on the floor, which can be calculated using the law of Cosine as:

$$\tilde{r} = \sqrt{r^2 + \hat{W}^2 - 2r\hat{W}\cos\theta}. \tag{14}$$

the area differential $\mathrm{d}A$ can be converted to $r\mathrm{d}r\mathrm{d}\theta$ in a cylinder coordinate system. Assume that the reflectivity of the ceiling is ρ_c. After the light signal reaches point $\vec{a}_b$, ρ_c of the incident optical power is reflected and a fraction of the reflected power is incident to the receiver. In addition, the transmission from point $\vec{a}_b$ to the receiver leads to a further delay of $\tau_{c2r}^{\vec{a}_b}$. Therefore, the CIR from the transmitter bounced by the floor and ceiling point $\vec{a}_b$ to the receiver can be found as:

$$\mathrm{d}h_{\mathrm{tfcr}}^{\vec{a}_b}(t) = \rho_c G_{c2r}^{\vec{a}_b} \mathrm{d}h_{\mathrm{tfc}}^{\vec{a}_b}\left(t - \tau_{c2r}^{\vec{a}_b}\right), \tag{15}$$

where $G_{c2r}^{\vec{a}_b}$ corresponds to path loss of the transmission from point $\vec{a}_b$ to the receiver. In conjunction with the receiver position of $(0, 0, z_r)$, the path loss can be found as [21]:

$$G_{c2r}^{\vec{a}_b} = \frac{A_{\mathrm{pd}}\mathbf{1}_{\mathrm{FoV}}^{c2r}\cos\phi_{c2r}\cos\psi_{c2r}}{\pi D_{c2r}^2} = \frac{(z_s - z_r)^2 A_{\mathrm{pd}}\mathbf{1}_{\mathrm{FoV}}^{c2r}}{\pi D_{c2r}^4}, \tag{16}$$

where D_{c2r} is the Euclidean distance between point $\vec{a}_b$ and the receiver, and the indicator function $\mathbf{1}_{\mathrm{FoV}}^{c2r}$ determines whether the incident signal is within the FoV of the receiver. It is defined that $\mathbf{1}_{\mathrm{FoV}}^{c2r} = 1$, if the incident angle ψ_{c2r} to the receiver is smaller than the receiver FoV, which corresponds to the condition that $\cos\psi_{c2r} = (z_s - z_r)/D_{c2r} \geq \cos\psi_{\mathrm{FoV}}$. Otherwise, $\mathbf{1}_{\mathrm{FoV}}^{c2r} = 0$. With the defined coordinate system, the distance D_{c2r} can be calculated as $D_{c2r} = \sqrt{r^2 + (z_s - z_r)^2}$. Then, the delay can be calculated as $\tau_{c2r}^{\vec{a}_b} = D_{c2r}/c$. Note that (15) only accounts for the channel via point $\vec{a}_b$. In order to get the entire CIR for the TFCR category, the channels via all points on the ceiling should be considered. This leads to an integration over the whole ceiling plane. By inserting (13), (16) into (15) and carrying out the integration over the ceiling plane, the CIR for the TFCR category can be found as:

$$h_{\mathrm{tfcr}}^{[2]}(t) = \int_{-\pi}^{\pi}\int_{0}^{\infty} \frac{\rho_c (z_s - z_r)^2 A_{\mathrm{pd}}\mathbf{1}_{\mathrm{FoV}}^{c2r}}{\pi D_{c2r}^4} \times \hbar_{\{m, r\mathrm{d}r\mathrm{d}\theta, \rho_f, z_s, z_s, \tilde{r}, 90^\circ\}}^{[0,0,1],[0,0,1]}\left(t - \frac{D_{c2r}}{c}\right), \tag{17}$$

which can be directly calculated using the standard numerical method. However, the computation complexity is very high as it requires solving three numerical integrations.

In order to reduce the computational complexity of the CIR calculation, a simpler approximated expression can be used as a substitution of the exact expression with a minor loss in accuracy. In a special case of $\tilde{r} = 0$, expression (13) can be significantly simplified. It has been found that expression (13) can be approximated by this simplified spacial case expression with appropriate scaling as:

$$\begin{aligned}\mathrm{d}h_{\mathrm{tfc}}^{\vec{a}_b}(t) &\approx \mathcal{F}_{\mathrm{tfc}}\mathcal{U}\left(t - \frac{D_{\mathrm{tfc},\vec{a}_b}}{c}\right)\hbar_{\{m, r\mathrm{d}r\mathrm{d}\theta, \rho_f, z_s, z_s, 0, 90^\circ\}}^{[0,0,1],[0,0,1]}(t) \\ &= \frac{(m+1)r\mathrm{d}r\mathrm{d}\theta\rho_f z_s^{m+3}\mathcal{F}_{\mathrm{tfc}}}{\pi(c/2)^{m+5}t^{m+6}}\mathcal{U}\left(t - \frac{D_{\mathrm{tfc},\vec{a}_b}}{c}\right),\end{aligned} \tag{18}$$

where $D_{\mathrm{tfc},\vec{a}_b} = \sqrt{4z_s^2 + \tilde{r}^2}$ is the length of the shortest path in the single reflection channel from transmitter via the floor to point $\vec{a}_b$, the unit step function is used to make sure the CIR has non-zero value only after the minimum delay and $\mathcal{F}_{\mathrm{fcr}}$ represents the scaling factor. Many potential functions for $\mathcal{F}_{\mathrm{tfc}}$ can be found by using curve-fitting tool. Here, we have chosen the following function for the scaling factor:

$$\mathcal{F}_{\mathrm{fcr}} = \beta_{\mathrm{tfc}}\frac{\tilde{r}^2}{z_s^2} + 1, \tag{19}$$

where the factor β_{tfc} is related to the Lambertian emission order m, and a suitable function for β_{tfc} is found to be $0.006242(m + 0.2578)^2 + 0.1328$. The approximation by using the scaling factor (19) is found to be accurate in the region of interest. In addition, this scaling factor provide an opportunity to further simplify the final CIR expression, which will be shown in the following derivations. The details and accuracy of this approximation has been demonstrated in Appendix B. By inserting (18) into (17), the CIR expression for the TFCR category can be simplified as:

$$h_{\mathrm{tfcr}}^{[2]}(t) = \int_{-\pi}^{\pi}\int_{0}^{\infty} \frac{2^{m+5}A_{\mathrm{pd}}c\rho_f\rho_c(m+1)z_s^{m+3}r}{\pi^2(z_s - z_r)^{-2}\left(r^2 + (z_s - z_r)^2\right)^2} \times \frac{\mathcal{F}_{\mathrm{tfc}}\mathbf{1}_{\mathrm{FoV}}^{c2r}\mathcal{U}\left(t - \frac{D_{\mathrm{tfcr},\vec{a}_b}}{c}\right)\mathrm{d}r\mathrm{d}\theta}{\left(ct - \sqrt{r^2 + (z_s - z_r)^2}\right)^{m+6}}, \tag{20}$$

where the term $D_{\mathrm{tfcr},\vec{a}_b}$ denotes the length of the shortest propagation path via point $\vec{a}_b$ in the TFCR channel. Its value can be calculated as:

$$\begin{aligned}D_{\mathrm{tfcr},\vec{a}_b} = &\sqrt{4z_s^2 + r^2 + \hat{W}^2 - 2r\hat{W}\cos\theta} \\ &+ \sqrt{r^2 + (z_s - z_r)^2}.\end{aligned} \tag{21}$$

The term with unit step function in (20) indicates that $h_{\mathrm{tfcr}}^{[2]}(t)$ is non-zero only when $ct \geq D_{\mathrm{tfcr},\vec{a}_b}$, which leads to the following

IEEE Proof

inequality:

$$\left(c^2t^2-\hat{W}^2\cos^2\theta\right)r^2+c^2t^2\left(z_s-z_r\right)^2 -\left(c^2t^2-\hat{W}^2-\left(z_s+z_r\right)\left(3z_s-z_r\right)\right)\hat{W}\cos\theta r -\frac{1}{4}\left(c^2t^2-\hat{W}^2-\left(z_s+z_r\right)\left(3z_s-z_r\right)\right)^2\leq 0. \quad (22)$$

With the satisfaction of (22), the integration limits in (20) can be changed to finite values, and the unit step function in (20) can be changed to $\mathcal{U}(t-D_{\mathrm{tfcr,min}}/c)$, where $D_{\mathrm{tfcr,min}}=\sqrt{(3z_s-z_r)^2+\hat{W}^2}$. Thus, (20) can be further modified as:

$$h^{[2]}_{\mathrm{tfcr}}(t)=\int_{\mathfrak{r}_1}^{\mathfrak{r}_2}\int_0^{\vartheta} \frac{2^{m+6}A_{\mathrm{pd}}c\rho_f\rho_c(m+1)z_s^{m+3}r\mathcal{F}_{\mathrm{tfc}}\mathbf{1}^{c2r}_{\mathrm{FoV}}}{\pi^2(z_s-z_r)^{-2}\left(ct-\sqrt{r^2+(z_s-z_r)^2}\right)^{m+6}} \times\frac{\mathcal{U}\left(t-\frac{D_{\mathrm{tfcr,min}}}{c}\right)\mathrm{d}\theta\mathrm{d}r}{\left(r^2+(z_s-z_r)^2\right)^2}. \quad (23)$$

Note that in the modification (23), the expression is multiplied by a factor of 2, and the lower limit of the integral with θ is change to 0. This is because expression (20) is reflection symmetric with respect to the x-axis. The integration limits $\mathfrak{r}_1$ and $\mathfrak{r}_2$ in (23) can be calculated by solving the inequality (22) with r as the unknown variable. The boundary values of r can be found as:

$$r_1=\frac{\hat{W}\left(c^2t^2-\mathfrak{c}_{\mathrm{tfcr},1}\right)-ct\sqrt{\mathfrak{c}_{\mathrm{tfcr},2}}}{2\left(c^2t^2-\hat{W}^2\right)}, \quad (24)$$

$$r_2=\frac{\hat{W}\left(c^2t^2-\mathfrak{c}_{\mathrm{tfcr},1}\right)+ct\sqrt{\mathfrak{c}_{\mathrm{tfcr},2}}}{2\left(c^2t^2-\hat{W}^2\right)}, \quad (25)$$

where $\mathfrak{c}_{\mathrm{tfcr},1}=\hat{W}^2+(z_s+z_r)(3z_s-z_r)$ and $\mathfrak{c}_{\mathrm{tfcr},2}=(c^2t^2-\mathfrak{c}_{\mathrm{tfcr},1})^2-4(z_s-z_r)^2(c^2t^2-\hat{W}^2)$. Then, the solution to the integration limits are $\mathfrak{r}_1=\max(r_1,0)$ and $\mathfrak{r}_2=r_2$. The integration limit ϑ can also be calculated by solving the same equation originated from (22) with θ as the unknown. The solution to the limit ϑ is found as:

$$\vartheta=\begin{cases}\arccos\left(\dfrac{2ct\sqrt{r^2+(z_s-z_r)^2}-c^2t^2+\mathfrak{c}_{\mathrm{tfcr},1}}{2r\hat{W}}\right) & : r\geq -r_1\\ \pi & : r<-r_1\end{cases}, \quad (26)$$

The approximation in (18) makes (23) a simple function of θ. This creates an opportunity to solve the integral with respect to θ, thereby further simplifying (23). Therefore, the final CIR expression for the TFCR category can be written in a form with a 1-D integral as (27).

$$h^{[2]}_{\mathrm{tfcr}}(t)=\frac{2^{m+6}cA_{\mathrm{pd}}\rho_f\rho_c(m+1)}{\pi^2\left(z_s-z_r\right)^{-2}z_s^{-m-1}}\mathcal{U}\left(t-\frac{D_{\mathrm{tfcr,min}}}{c}\right) \int_{\mathfrak{r}_1}^{\mathfrak{r}_2}\frac{\vartheta\left(\beta_{\mathrm{tfc}}\left(r^2+\hat{W}^2-\frac{2r\hat{W}\sin\vartheta}{\vartheta}\right)+z_s^2\right)r\mathbf{1}^{c2r}_{\mathrm{FoV}}\mathrm{d}r}{\left(r^2+(z_s-z_r)^2\right)^2\left(ct-\sqrt{r^2+(z_s-z_r)^2}\right)^{m+6}} \quad (27)$$

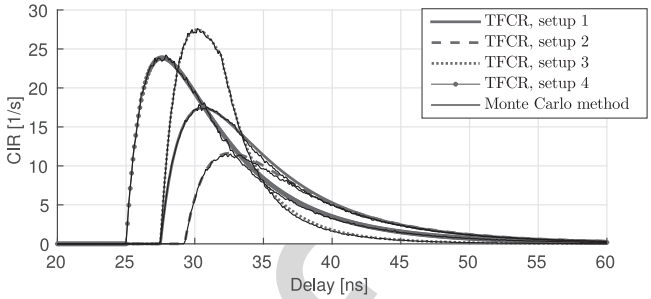

Fig. 9. NLoS CIR results with TFCR category. Setup 1: $\phi_{1/2}=60°$, $\psi_{\mathrm{FoV}}=90°$, $\hat{W}=0$ m and $z_r=0.75$ m. Compared to the configuration in setup 1, $\hat{W}$ is modified to 3 m in setup 2, $\phi_{1/2}$, ψ_{FoV} are modified to $40°$, $45°$ in setup 3, and z_r is modified to 1.5 m in setup 4, respectively. The configuration of the remaining parameters are listed in Table I.

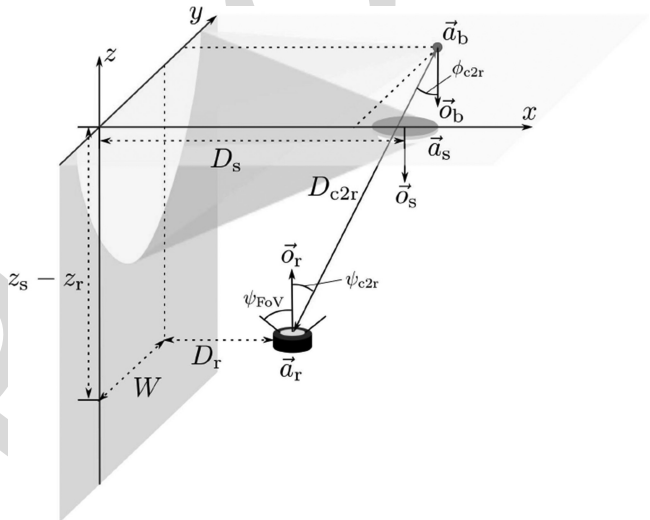

Fig. 10. Light propagation geometry in TWCR channel.

Fig. 9 shows a number of CIRs of the TFCR category with different setups calculated using (27). In addition, the corresponding CIR results generated using the Monte Carlo method are also presented in Fig. 9. The agreement between the CIR results generated by different methods validate the CIR calculation expression in TFCR category (27).

C. Transmitter-to-Wall-to-Ceiling-to-Receiver Channel Impulse Response (TWCR)

In the TWCR category, the ceiling and wall are considered as shown in Fig. 10. The boundary of the ceiling and wall planes is the line of their intersection, and these two planes extend

infinitely to other directions. Again, a point located at $\vec{a}_b$ on the ceiling is considered, as shown in Fig. 10. This time the space is defined by a 3-D Cartesian coordinate system x-y-z. The origin is defined at the projection point of the transmitter on the wall plane. Thus, the coordinate of the ceiling point $\vec{a}_b$ is defined at $(x, y, 0)$. Similar to the CIR calculation for the TFCR category, a single reflection channel from the transmitter to the ceiling point $\vec{a}_b$ is considered, except that the channel is resulted from the reflection by the wall plane. It is defined as transmitter-to-wall-to-ceiling point (TWC) channel. Again the corresponding CIR can be calculated using (2) as:

$$\mathrm{d}h^{\vec{a}_b}_{\mathrm{twc}}(t) = \hbar^{[0,1,0],[0,1,0]}_{\{m,\mathrm{d}A,\rho_w,D_s,x,|y|,90^\circ\}}(t). \tag{28}$$

In a Cartesian coordinate system, the detection area differential $\mathrm{d}A$ can be converted to $\mathrm{d}x\mathrm{d}y$. Next, the LoS transmission from the ceiling bouncing point $\vec{a}_b$ to the receiver is considered, which introduces a further attenuation and an extra delay on top of the TWC channel. The resulting CIR can be found as:

$$\mathrm{d}h^{\vec{a}_b}_{\mathrm{twcr}}(t) = \rho_c G^{\vec{a}_b}_{c2r}\mathrm{d}h^{\vec{a}_b}_{\mathrm{twc}}\left(t-\tau^{\vec{a}_b}_{c2r}\right), \tag{29}$$

which is the same as (15) except the category of the single reflection channel. The LoS path loss $G^{\vec{a}_b}_{c2r}$ is again calculated using (16). The additional delay is again $\tau^{\vec{a}_b}_{c2r} = D_{c2r}/c$. However, due to the use of a different coordinate system, the calculation of the Euclidean distance follows the expression below:

$$D_{c2r} = \sqrt{(z_s - z_r)^2 + (x - D_r)^2 + (y - W)^2}. \tag{30}$$

In order to calculate the final CIR for the TWCR category, all of the paths reflected by the ceiling are considered, which leads to an integration of (29) over the ceiling plane as:

$$h^{[2]}_{\mathrm{twcr}}(t) = \int_{-\infty}^{\infty}\int_{0}^{\infty} \frac{\rho_c (z_s - z_r)^2 A_{\mathrm{pd}} \mathbf{1}^{c2r}_{\mathrm{FoV}}}{\pi D^4_{c2r}} \times \hbar^{[0,1,0],[0,1,0]}_{\{m,\mathrm{d}x\mathrm{d}y,\rho_w,D_s,x,|y|,90^\circ\}}\left(t-\frac{D_{c2r}}{c}\right). \tag{31}$$

In order to reduce the complexity of (31), we can use a simpler approximated expression for (28). It has been found that the special case of $y = 0$ m in the calculation of (28) leads to a simpler and closed form expression. Similar to the approximation in (18), the following expression with magnitude scaling and minimum delay control is used to approximate the exact CIR (28):

$$\mathrm{d}h^{\vec{a}_b}_{\mathrm{twc}}(t) \approx \mathcal{F}_{\mathrm{twc}}\hbar^{[0,1,0],[0,1,0]}_{\{m,\mathrm{d}x\mathrm{d}y,\rho_w,\hat{D}_s,\hat{x},0,90^\circ\}} = \frac{\rho_w \hat{D}_s \hat{x}\mathcal{B}\left(\frac{m+2}{2},\frac{m+2}{2}\right)\mathfrak{r}^2_{\mathrm{twc}}(t)\mathcal{F}_{\mathrm{twc}}\mathcal{U}\left(t-\frac{D_{\mathrm{twc},\vec{a}_b}}{c}\right)\mathrm{d}x\mathrm{d}y}{\frac{\pi^2 t}{2^m(m+1)}\left(1+\frac{\hat{D}_s^2}{\mathfrak{r}^2_{\mathrm{twc}}(t)}\right)^{\frac{m-1}{2}}\left(\frac{c^2t^2}{4}-\frac{\left(\hat{D}_s^2-\hat{x}^2\right)^2}{4c^2t^2}\right)^3}, \tag{32}$$

where $D_{\mathrm{twc},\vec{a}_b} = \sqrt{(D_s + x)^2 + y^2}$ is the length of the shortest path in the single reflection channel from the transmitter via the wall to point $\vec{a}_b$, $\mathcal{B}(u_1, u_2)$ is the β-function that is defined as: $\mathcal{B}(u_1, u_2) = \int_0^1 v^{u_1-1}(1-v)^{u_2-1}\mathrm{d}v$, and

$$\mathfrak{r}^2_{\mathrm{twc}}(t) = \frac{c^2t^2}{4} + \frac{\left(\hat{D}_s^2 - \hat{x}^2\right)^2}{4c^2t^2} - \frac{\hat{D}_s^2 + \hat{x}^2}{2}. \tag{33}$$

In the approximated expression (32), $\mathcal{F}_{\mathrm{twc}}$ is the scaling factor. Suitable functions for $\mathcal{F}_{\mathrm{twc}}$ can be obtained by using curve fitting tools. The following function is one of them:

$$\mathcal{F}_{\mathrm{twc}} = \left(1 + \frac{y^2 + \beta_{\mathrm{twc},1}\frac{y^3|x-D_s|^3}{(x+D_s)^4}}{(x+\beta_{\mathrm{twc},2}D_s)^2}\right)^{-\frac{1}{2}}, \tag{34}$$

where $\beta_{\mathrm{twc},1} = 0.8125$ and $\beta_{\mathrm{twc},2} = 0.8088\mathrm{e}^{-0.6878m} + 0.5304\mathrm{e}^{-0.007006m}$ are found to provide an accurate approximation. Note that expression (2) has been used in both (28) and (32). The values for L_s and L_r are D_s and x in (28). However, they have been substituted with $\hat{D}_s$ and $\hat{x}$ in (32). This is because a simple linear scaling by $\mathcal{F}_{\mathrm{twc}}$ cannot provide an approximation with sufficient accuracy. The values for L_s and L_r have to be manipulated based on the parameter D_s, x, y and m in order to achieve an accurate approximation. In addition, the minimum delay control is realised by this step. The following functions for $\hat{D}_s$ and $\hat{x}$ are found to provide accurate approximations:

$$\hat{D}_s = \beta_{\mathrm{twc},3}D_{\mathrm{twc},\vec{a}_b}, \tag{35}$$

$$\hat{x} = (1-\beta_{\mathrm{twc},3})D_{\mathrm{twc},\vec{a}_b}, \tag{36}$$

where $\beta_{\mathrm{twc},3} = D_s((D_s + x)^2 + 4y^2(m^{0.045} - 1))^{-\frac{1}{2}}$ is found to provide an accurate approximation. Note that the approximation in (32) is more complex than that in (18). This is because the factors in approximation (32) are functions of four parameters D_s, x, y and m. In contrast, the factors in (18) are functions of two parameters m and $\tilde{r}$ only. The details and accuracy of the approximation (32) are provided in Appendix C.

Thus, by inserting (32) into (31), the CIR expression for the TWCR category can be calculated as:

$$h^{[2]}_{\mathrm{twcr}}(t) = \int_{-\infty}^{\infty}\int_{0}^{\infty} \frac{2^m\rho_w\rho_c A_{\mathrm{pd}}\hat{D}_s\hat{x}\mathcal{B}\left(\frac{m+2}{2},\frac{m+2}{2}\right)\mathbf{1}^{c2r}_{\mathrm{FoV}}}{\frac{\pi^3 D^4_{c2r}\left(t-\frac{D_{c2r}}{c}\right)}{(m+1)(z_s-z_r)^2}\left(1+\frac{\hat{D}_s^2}{\mathfrak{r}^2_{\mathrm{twc}}\left(t-\frac{D_{c2r}}{c}\right)}\right)^{\frac{m-1}{2}}} \times \frac{\mathfrak{r}^2_{\mathrm{twc}}\left(t-\frac{D_{c2r}}{c}\right)\mathcal{F}_{\mathrm{twc}}\mathcal{U}\left(t-\frac{D_{\mathrm{twcr},\vec{a}_b}}{c}\right)\mathrm{d}x\mathrm{d}y}{\left(\frac{(ct-D_{c2r})^2}{4}-\frac{\left(\hat{D}_s^2-\hat{x}^2\right)^2}{4(ct-D_{c2r})^2}\right)^3}, \tag{37}$$

where $D_{\mathrm{twcr},\vec{a}_b}$ denotes the length of the shortest propagation path via point $\vec{a}_b$ in the TWCR channel. Its value can be calculated as:

$$D_{\mathrm{twcr},\vec{a}_b} = \sqrt{(z_s - z_r)^2 + (x - D_r)^2 + (y - W)^2} + \sqrt{(D_s + x)^2 + y^2}. \tag{38}$$

The unit step function in (37) indicates that $h^{[2]}_{\mathrm{twcr}}(t)$ is non-zero only when $ct \geq D_{\mathrm{twcr},\vec{a}_b}$, which leads to the following

IEEE Proof

inequality:

$$\left(c^2t^2-W^2\right)y^2-W\left(c^2t^2+2\left(D_s+D_r\right)x-\left(z_s-z_r\right)^2-W^2-D_r^2+D_s^2\right)y+c^2t^2\left(D_s+x\right)^2-\frac{1}{4}\left(c^2t^2-W^2+2\left(D_s+D_r\right)x-\left(z_s-z_r\right)^2-D_r^2+D_s^2\right)^2\geq 0. \quad (39)$$

With the satisfaction of (39), the integration limits in (37) should be changed to finite values, and the term with the unit step function in (37) can be replaced by $\mathcal{U}(t-D_{\mathrm{twcr,min}}/c)$, where $D_{\mathrm{twcr,min}}$ is the length of the shortest propagation path in the TWCR channel. It can be calculated as:

$$D_{\mathrm{twcr,min}}=\sqrt{W^2+\left(D_s+\sqrt{\left(z_s-z_r\right)^2+D_r^2}\right)^2}. \quad (40)$$

Thus, (37) can be further modified as (41) shown at bottom of this page. The integration limits $\mathfrak{y}_1$ and $\mathfrak{y}_2$ in (41) can be calculated by solving the equation originated from inequality (39) with y as the unknown variable. The solutions to $\mathfrak{y}_1$ and $\mathfrak{y}_2$ can be found as:

$$\mathfrak{y}_2=\frac{W\left(c^2t^2-\mathfrak{c}_{\mathrm{twcr},1}+2\left(D_s+D_r\right)x\right)+ct\sqrt{\mathfrak{c}_{\mathrm{twcr},2}}}{2\left(c^2t^2-W^2\right)}, \quad (42)$$

$$\mathfrak{y}_1=\frac{W\left(c^2t^2-\mathfrak{c}_{\mathrm{twcr},1}+2\left(D_s+D_r\right)x\right)-ct\sqrt{\mathfrak{c}_{\mathrm{twcr},2}}}{2\left(c^2t^2-W^2\right)}, \quad (43)$$

where $\mathfrak{c}_{\mathrm{twcr},1}=(z_s-z_r)^2+W^2+D_r^2-D_s^2$ and $\mathfrak{c}_{\mathrm{twcr},2}=(c^2t^2-\mathfrak{c}_{\mathrm{twcr},1}+2(D_s+D_r)x)^2-4(c^2t^2-W^2)(D_s+x)^2$. To ensure the existence of the real-value solution to $\mathfrak{y}_1$ and $\mathfrak{y}_2$, the term $\mathfrak{c}_{\mathrm{twcr},2}$ have to be greater than zero, which leads to the solution to the integration limit $\mathfrak{x}$:

$$\mathfrak{x}=\frac{\left(\sqrt{c^2t^2-W^2}-D_s\right)^2-\left(z_s-z_r\right)^2-D_r^2}{2\left(\sqrt{c^2t^2-W^2}-D_s-D_r\right)}. \quad (44)$$

Fig. 11 shows a number of CIRs of the TWCR category with different configurations calculated using (41). In addition, the corresponding results generated using the Monte Carlo method are also provided for comparison. The agreement between the CIR results generated by different methods validate the CIR calculation expression for the TWCR category (41).

V. Overall Non-Line-of-Sight Channel Impulse Response

In conjunction with the analytical results for component CIRs in different light propagation categories, the overall CIR can be accurately approximated. Note that the TWR, TWCR component CIRs are with respect to a single wall. Since there are four walls in a typical room, the overall NLoS is the superposition of four TWR, four TWCR and one TFCR component CIRs. In order to calculate each component CIR, the related geometric parameters should be calculated based on the given information. The known information includes the room dimension $l_x\times l_y\times l_z$, the position of the transmitter $\vec{a}_s=[x_s,y_s,z_s]$ and the position of the receiver $\vec{a}_r=[x_r,y_r,z_r]$, as shown in Fig. 12. The geometric parameters that requires calculation include $D_{s,n}, D_{r,n}, W_n, \hat{W}$. Note that the subscript $n=1,2,3,4$ is used to distinguish the same type of parameters with respect to different walls. The cases with $n=1$ and $n=2$ correspond to the wall with $y=0$ and $y=l_y$, respectively. The cases with $n=3$ and $n=4$ correspond to the wall with $x=0$ and $x=l_x$, respectively. The calculation of these parameters can be straightforwardly inferred from Fig. 12 using Euclidean geometry. The equations for the calculation are concluded in Table II.

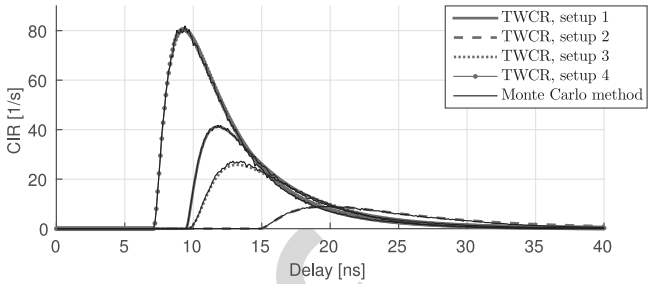

Fig. 11. NLoS CIR results with TWCR category. Setup 1: $\phi_{1/2}=60^\circ$, $\psi_{\mathrm{FoV}}=90^\circ$, $D_s=0.5$ m, $D_r=0.5$ m, $W=0.5$ m and $z_r=0.75$ m. Compared to the configuration in setup 1, D_s, D_r, W are modified to 1, 2, 2 m in setup 2, $\phi_{1/2}$, ψ_{FoV} are modified to 40°, 45° in setup 3, and z_r is modified to 1.5 m in setup 4, respectively. The configuration of the remaining parameters are listed in Table I.

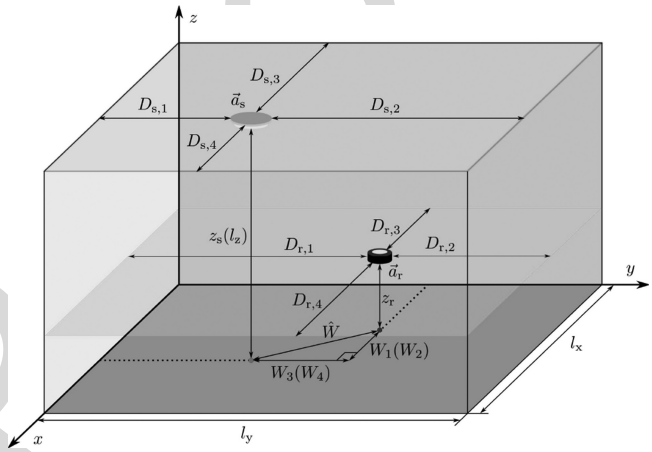

Fig. 12. A cuboid room of size $l_x\times l_y\times l_z$ with transmitter and receiver location of $\vec{a}_s$ and $\vec{a}_r$, respectively.

$$h^{[2]}_{\mathrm{twcr}}(t)=\frac{2^m\rho_w\rho_c A_{\mathrm{pd}}\mathcal{B}\left(\frac{m+2}{2},\frac{m+2}{2}\right)}{\pi^3(m+1)^{-1}\left(z_s-z_r\right)^{-2}}\int_{\mathfrak{y}_1}^{\mathfrak{y}_2}\int_0^{\mathfrak{x}}\frac{\mathbf{1}^{c2r}_{\mathrm{FoV}}\hat{D}_s\hat{x}\mathfrak{r}^2_{\mathrm{twc}}\left(t-\frac{D_{c2r}}{c}\right)\mathcal{F}_{\mathrm{twc}}\mathcal{U}\left(t-\frac{D_{\mathrm{twcr,min}}}{c}\right)\mathrm{d}x\mathrm{d}y}{D^4_{c2r}\left(t-\frac{D_{c2r}}{c}\right)\left(1+\frac{\hat{D}_s^2}{\mathfrak{r}^2_{\mathrm{twc}}\left(t-\frac{D_{c2r}}{c}\right)}\right)^{\frac{m-1}{2}}\left(\frac{(ct-D_{c2r})^2}{4}-\frac{\left(\hat{D}_s^2-\hat{x}^2\right)^2}{4(ct-D_{c2r})^2}\right)^3} \quad (41)$$

IEEE Proof

TABLE II
CALCULATION OF GEOMETRIC PARAMETERS

n	1	2	3	4
$D_{\mathrm{s},n}$	y_{s}	$l_{\mathrm{y}}-y_{\mathrm{s}}$	x_{s}	$l_{\mathrm{x}}-x_{\mathrm{s}}$
$D_{\mathrm{r},n}$	y_{r}	$l_{\mathrm{y}}-y_{\mathrm{r}}$	x_{r}	$l_{\mathrm{x}}-x_{\mathrm{r}}$
W_n	$\lvert x_{\mathrm{s}}-x_{\mathrm{r}}\rvert$		$\lvert y_{\mathrm{s}}-y_{\mathrm{r}}\rvert$	
$\hat{W}$	$\sqrt{(x_{\mathrm{s}}-x_{\mathrm{r}})^2+(y_{\mathrm{s}}-y_{\mathrm{r}})^2}$			

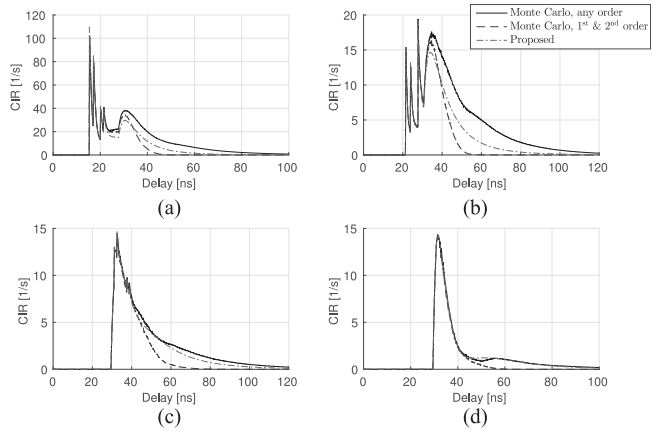

Fig. 13. NLoS CIR results with different configurations. The sub-plot (a), (b), (c) and (d) correspond to the link setup 1, 2, 3 and 4, respectively. In addition to the results generated using the proposed method, those generated using the Monte Carlo method considering any order of reflections and considering 1st and 2nd order reflections are also presented.

TABLE III
LINK CONFIGURATIONS CORRESPOND TO THE NLoS CIR RESULTS SHOWN IN FIG. 13

Parameter	Room size [m]	Transmitter coordinate [m]	Receiver coordinate [m]
Setup 1	$5\times5\times3$	$[2.5, 2.5, 3]$	$[2\ 1.5\ 0.75]$
Setup 2	$5\times8\times3$	$[2, 2, 3]$	$[2.5, 6, 0.75]$
Setup 3	$10\times10\times3$	$[4, 4, 3]$	$[5, 7, 0.75]$
Setup 4	$10\times10\times3$	$[4, 4, 3]$	$[5, 7, 0.75]$

Then, the overall NLoS CIR can be calculated as the sum of the nine component CIRs as:

$$h_{\mathrm{NLoS}}(t)\approx\sum_{n=1}^{4}h_{\mathrm{twr}}^{[1],\{D_{s,n},D_{r,n},W_n\}}(t)+h_{\mathrm{tfcr}}^{[2],\{\hat{W}\}}(t)+\sum_{n=1}^{4}h_{\mathrm{twcr}}^{[2],\{D_{s,n},D_{r,n},W_n\}}(t), \tag{45}$$

where $h_{\mathrm{twr}}^{[1],\{D_{s,n},D_{r,n},W_n\}}(t)$, $h_{\mathrm{tfcr}}^{[2],\{\hat{W}\}}(t)$ and $h_{\mathrm{twcr}}^{[2],\{D_{s,n},D_{r,n},W_n\}}(t)$ can be calculated using (12), (27) and (41), respectively.

A. Channel Impulse Response and Frequency Response Results

Fig. 13 shows the NLoS CIR results based on (45) in comparison to the results from using the Monte Carlo method. The setups of the analytical calculations and corresponding simulations are listed in Table III. A small square room and a longer rectangular room are considered in setup 1 and setup 2, respectively. A much larger room is considered in setup 3 and setup 4. A half-power semi-angle of $\phi_{1/2}=60^\circ$ and a receiver FoV of $\psi_{\mathrm{FoV}}=90^\circ$ are used in setup 1, 2 and 3. In setup 4, $\phi_{1/2}=40^\circ$ and $\psi_{\mathrm{FoV}}=45^\circ$. In setup 1, the transmitter and the receiver are close to each other, the size of the room is relatively small, and the link is sufficiently close to the walls. Consequently, the overall magnitude of the NLoS CIR is relatively higher, and the responses due to 1st order reflections dominate the NLoS CIR, especially for the responses with short delays. In setup 2, the increased indoor space and the increased transmitter receiver separation leads to a NLoS CIR with a decreased magnitude. In setups 3 and 4, the considered transmitter/receiver positions are further away from the walls. Consequently, the magnitude of the CIRs due to 1st order reflections decreases significantly. Compared to setup 3, smaller transmitter half-power semiangle $\phi_{1/2}$ and receiver FoV ψ_{FoV} are used in setup 4. Consequently, the magnitude of responses with longer delays is decreased. This is because the majority of the detected signal with a long delay is launched from the transmitter in a very large radiant angle, and very little optical power is radiated in the side directions of the transmitter with a small $\phi_{1/2}$. In addition, a signal with a long delay is also likely to reach the receiver with a very large incident angle, which cannot be detected by a receiver with a small ψ_{FoV}.

The accuracy of the approximation using the proposed method varies with the time delay. For the responses with short delays (roughly the first 10 ns), the proposed method offers excellent accuracy. For the responses with medium delay (roughly another 10 ns after the short delay), the proposed method underestimates the CIR due to the omission of the response caused by part of the 2nd reflections with TWWR, TFWR categories and higher order reflections. For the responses with a long delay, the proposed method over-estimate the CIR compared to the results generated using the Monte Carlo method considering the 1st and 2nd order reflections. This is because the proposed CIR calculation method with each propagation category omits the effects of the boundary of the surfaces, which introduces extra responses with a long delay. However, this over-estimation is lower than the responses caused by higher order reflections. From a different point of view, it slightly compensates the omission of the higher order reflections. In addition, the approximation accuracy is also related to the size of the room. The proposed method offers a better approximation in a large indoor environment (setup 3 and setup 4) compared to the cases in a smaller indoor environment (setup 3 and setup 4).

Fig. 14 shows the corresponding magnitude response of the NLoS channels. It can be observed that with the presence of a LoS path between the transmitter and the receiver, the accuracy of the approximation using the proposed method varies with frequency. For the magnitude response with extremely low frequency (<5 MHz), the proposed method underestimates the response relative to the case with the Monte Carlo method considering any order of reflections. However, comparing with the Monte Carlo method considering the 1st and 2nd order reflections, the proposed method offers a similar magnitude response. For the magnitude response with low frequency (5–50 MHz), the three curves are close to each other with a slight mismatch.

IEEE Proof

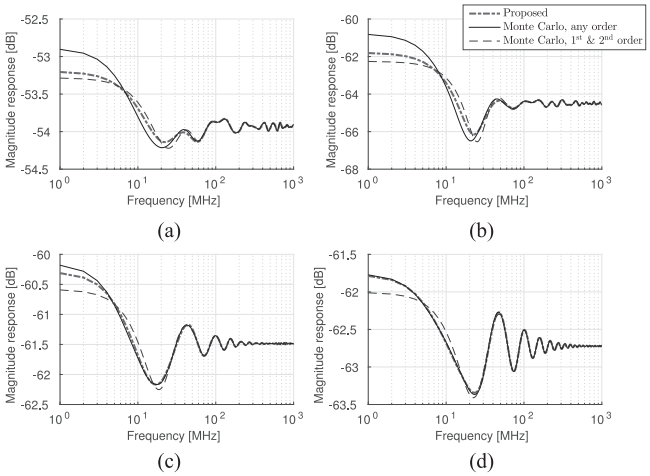

Fig. 14. NLoS magnitude response results with different configurations. The sub-plot (a), (b), (c) and (d) correspond to the link setup 1, 2, 3 and 4, respectively.

TABLE IV
SETUP CONFIGURATIONS IN THE COMPUTATION TIME EVALUATION

Parameter	Room size [m]	Transmitter coordinate [m]	Receiver coordinate [m]
Setup 1	$5 \times 5 \times 3$	$[2.5, 2.5, 3]$	$[2.5, 2.5, 0.75]$
Setup 2	$10 \times 10 \times 3$	$[2.5, 2.5, 3]$	$[7.5, 7.5, 0.75]$

For the magnitude response with high frequency (>50 MHz), the three curves are virtually identical.

B. Computational Time Evaluation

The calculation of (12), (27) and (41) requires solving only one or two 1-D numerical integrals. Therefore, the computational complexity of (45) is very low. In this section, the computation time of the proposed method is evaluated compared with that of the state-of-the-art methods. In this study, the numerical integrations in (45) are implemented based on the Trapezoidal rule, and the interval for each definite integral is divided into N bins. The greater the number of the bins, the more accurate the calculated result. Since θ is the variable in the integral (12), the number of bins in the integral (12) is defined as N_θ. Similarly, the numbers of bins in the calculation of (27) and (41) are defined as N_r and N_x (N_y), respectively. It has been empirically identified that $N_\theta = 50$, $N_r = 50$ and $N_x = N_y = 30$ offer reasonably accurate NLoS CIR results with a short computation time.

The impulse response of a channel is in the form of a continuous signal. In the actual CIR calculation, the result with a fixed time resolution is produced. By increasing the time resolution, a clearer view of the CIR can be obtained to characterise the channel with a wider frequency range. Two link setups are simulated to test the computation time while using three different methods. The configuration is listed in Table IV. The used half-power semi-angle is $\phi_{1/2} = 60^\circ$, and the remaining parameters are the same as those listed in Table I. The first link considers a small room with a closely located transmitter and receiver in the centre. The second link considers a larger room with a distant separation between the transmitter and the receiver. Fig. 15 shows that the required computation time in Matlab

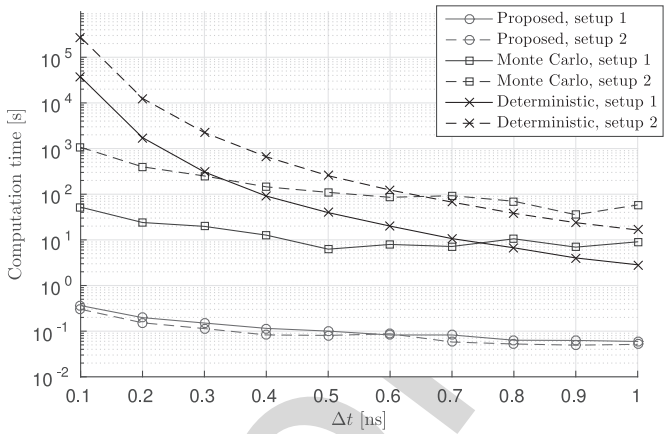

Fig. 15. NLoS CIR computation time with different calculation methods.

varies with the time resolution Δt. The considered calculation methods include the deterministic method proposed in [4], the Monte Carlo method proposed in [22] and the proposed method in this study. To ensure the fairness of the comparison, up to 2nd order reflections are considered in the deterministic method and Monte Carlo method. With the deterministic method, the block size is configured based on the time resolution as $A_e = 2c^2\Delta t^2$ [8]. With the Monte Carlo method, the ray-tracing process is repeated until the normalised mean square error (NMSE) of the CIR result is less than 2.5×10^{-3}. Calculating low time resolution CIR ($\Delta t > 0.7$ ns), the deterministic and Monte Carlo methods are able to calculate the results with a computation time in the range of a few seconds to about 100 s. With the same time resolution, the proposed method is able to finish the calculation with a computation time of less than 0.1 s. With the decrease of Δt, the required computation time for all three methods increases. The required time for the deterministic method increases significantly. In the case of $\Delta t = 0.1$ ns, the computation time for the deterministic method is in the range of several hours to more than three days. This is because the increased time resolution leads to a significantly increased number of blocks that are smaller in size. Since the deterministic method considers all possible propagation paths between blocks and their combinations, the increased number of blocks significantly increases the computational complexity. In addition, increasing the room size requires a greater number of blocks to fill the larger internal surface area. Therefore, for the deterministic method, the computation time also increases significantly with the increase in the room size. With the Monte Carlo method, the increase of computation time with the decrease of Δt is not as significant as that with the deterministic method. With $\Delta t = 0.1$ ns, several minutes are required to obtain an accurate CIR result. This increase in computation time is due to the time bin width getting narrower as the time resolution increases. A narrower bin width requires more samples to average out the noise caused by the random process. In setup 2, the receiver is further away from the transmitter. Consequently, the traced ray has a lower probability to reach the region close to the receiver. Therefore, more computation time is required for the Monte Carlo method if the separation between the transmitter

IEEE Proof

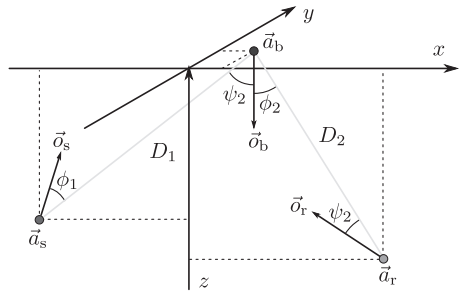

Fig. 16. Single reflection channel in Cartesian coordinates.

and receiver increases. In contrast, the computation time for the proposed method increases slightly with the decrease of Δt. With a time resolution of $\Delta t = 0.1$ ns, the computation time for the proposed method is still less than a second. Furthermore, the required computation time varies slightly for different link setups.

VI. Conclusions

In this paper, a computationally efficient analytical method was proposed to calculate the NLoS CIR in typical VLC deployments. The CIR results calculated using the proposed method are compared with those generated by using the Monte Carlo method in [9] and the deterministic ray-tracing method in [4]. In comparison with the benchmark methods, the proposed method can provide accurate CIR results for NLoS channels with up to 2nd order reflections. Furthermore, the required time for the proposed method is significantly shorter than the benchmarks (typically less than a second). This method is useful for research that requires a large number of channel samples considering NLoS components, such as VLC MIMO [14] or system level studies of networked VLC [23].

Appendix A
Derivation of Proposition 1

Firstly, we place the setup shown in Fig. 2 in a Cartesian coordinate system. As shown in Fig. 16, the locations of the source element and the receiving element are defined in the coordinates as $\vec{a}_s = [-L_s L_b/(L_s+L_r), 0, -L_s]$ and $\vec{a}_r = [L_r L_b/(L_s+L_r), 0, -L_r]$, respectively. The orientations of the source element and the receiving element are defined as $\vec{o}_s = [\tilde{x}_s, \tilde{y}_s, \tilde{z}_s]$ and $\vec{o}_r = [\tilde{x}_r, \tilde{y}_r, \tilde{z}_r]$. All orientation vectors have a unity modulus. Considering the amount of light power incident to a point on the reflector at $\vec{a}_b = [x, y, 0]$, the Euclidean distance between the source and this point is D_1 and the Euclidean distance between the receiver and this point is D_2. The orientation of the reflector $\vec{o}_b$ is opposite to the direction of the z-axis. According to [21], the calculus of the path loss via $\vec{a}_b$ can be calculated as:

$$\mathrm{d}G = \frac{\rho(m+1)A_r \mathrm{d}A}{2\pi^2 D_1^2 D_2^2} \mathbf{1}_{\mathrm{FoV}} \cos^m \phi_1 \cos\psi_1 \cos\phi_2 \cos\psi_2, \tag{A.1}$$

where ϕ_1 and ψ_1 denote the radiant angle and incident angle from the light source and to the point at $\vec{a}_b$ on the reflector, respectively; ϕ_2 and ψ_2 denote the radiant angle and incident angle from the the point at $\vec{a}_b$ on the reflector to the receiving element, respectively; $\mathrm{d}A$ denotes the differential of the physical area of the reflecting point; and $\mathbf{1}_{\mathrm{FoV}}$ is the indicator function showing whether the path is within the FoV of the receiver and within the coverage of the source. This leads to:

$$\mathbf{1}_{\mathrm{FoV}} = \begin{cases} 1 & : \cos\psi_1 \geq 0 \ \& \ \cos\psi_2 \geq \cos\psi_{\mathrm{FoV}} \\ 0 & : \text{otherwise} \end{cases}. \tag{A.2}$$

The relevant terms in (A.1) can be calculated as [4]:

$$D_1 = \sqrt{\left(x + \frac{L_s L_b}{L_s+L_r}\right)^2 + y^2 + L_s^2},$$

$$D_2 = \sqrt{\left(x - \frac{L_r L_b}{L_s+L_r}\right)^2 + y^2 + L_r^2},$$

$$\cos\phi_1 = \frac{\vec{o}_s\left(\vec{a}_b - \vec{a}_s\right)^T}{D_1} = \frac{\tilde{x}_s\left(x + \frac{L_s L_b}{L_s+L_r}\right) + \tilde{y}_s y + \tilde{z}_s L_s}{D_1},$$

$$\cos\psi_1 = \frac{\vec{o}_b\left(\vec{a}_s - \vec{a}_b\right)^T}{D_1} = \frac{L_s}{D_1},$$

$$\cos\phi_2 = \frac{\vec{o}_b\left(\vec{a}_r - \vec{a}_b\right)^T}{D_2} = \frac{L_r}{D_2},$$

$$\cos\psi_2 = \frac{\vec{o}_r\left(\vec{a}_b - \vec{a}_r\right)^T}{D_2} = \frac{\tilde{x}_r\left(x - \frac{L_r L_b}{L_s+L_r}\right) + \tilde{y}_r y + \tilde{z}_r L_r}{D_2}.$$

Thus, (A.1) can be rewritten as:

$$\mathrm{d}G(x,y) = \frac{\rho(m+1)A_r L_s L_r}{2\pi^2} \mathfrak{f}(x,y)\mathrm{d}x\mathrm{d}y \tag{A.3}$$

$$\begin{aligned}\mathfrak{f}(x,y) = \mathbf{1}_{\mathrm{FoV}} &\left(\tilde{x}_s\left(x + \frac{L_s L_b}{L_s+L_r}\right) + \tilde{y}_s y + L_s\tilde{z}_s\right)^m \\ &\times \left(\tilde{x}_r\left(x - \frac{L_r L_b}{L_s+L_r}\right) + \tilde{y}_r y + L_r\tilde{z}_r\right) \\ &\times \left(\left(x + \frac{L_s L_b}{L_s+L_r}\right)^2 + y^2 + L_s^2\right)^{-\frac{m+3}{2}} \\ &\times \left(\left(x - \frac{L_r L_b}{L_s+L_r}\right)^2 + y^2 + L_r^2\right)^{-2}.\end{aligned} \tag{A.4}$$

The total received signal power can be calculated by integrating (A.3) over the entire reflector.

However, channel impulse response is a quantity closely related to delay t. In order to make the received signal power involve the time delay, we firstly consider calculating the power of the received signal that experienced a delay of less than t. This amount of power is denoted as $\hat{P}_{\mathrm{opt},h}(t)$. The time delay is in conjunction with the length of the transmission path. With the given positions of the light source element and receiving element, all of the single reflection paths with a delay less than t are within an ellipsoid. The foci of this ellipsoid are located at the positions of light source and the receiving element as shown in Fig. 17. For the convenience of defining this ellipsoid, another Cartesian coordinate system x'-y'-z' is defined. In the x'-y'-z' system, the centre of the ellipsoid is placed at the origin

IEEE Proof

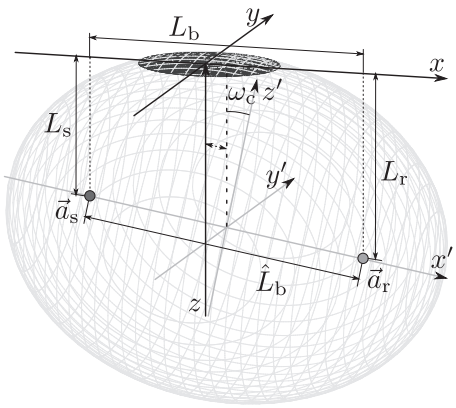

Fig. 17. Single reflection transmission geometry with considering the paths experiencing a delay less than a certain value t.

of the coordinates, and the two foci are placed on the x' axis with the coordinates of $[-\hat{L}_b/2, 0, 0]$ and $[\hat{L}_b/2, 0, 0]$, where $\hat{L}_b^2 = L_b^2 + (L_s - L_r)^2$. The equation for the ellipsoid can be written as:

$$\frac{x'^2}{(ct/2)^2} + \frac{y'^2}{(ct/2)^2 - \left(\hat{L}_b/2\right)^2} + \frac{z'^2}{(ct/2)^2 - \left(\hat{L}_b/2\right)^2} \leq 1,$$

With a given coordinate in x-y-z, the corresponding coordinate in x'-y'-z' can be obtained by carrying out a coordinate transformation as follows:

$$\begin{bmatrix} x' \\ y'z' \end{bmatrix} = \begin{bmatrix} \cos\omega_c & 0 & \sin\omega_c \\ 0 & 1 & 0 \\ -\sin\omega_c & 0 & \cos\omega_c \end{bmatrix} \begin{bmatrix} x \\ y \\ z \end{bmatrix} + \begin{bmatrix} \frac{2L_sL_r}{L_s+L_r}\sin\omega_c + \frac{\hat{L}_b(L_s-L_r)}{2(L_s+L_r)} \\ 0 \\ \frac{2L_sL_r}{L_s+L_r}\cos\omega_c \end{bmatrix}, \quad \text{(A.5)}$$

where ω_c is the rotation angle of the coordinates. It can be calculated using:

$$\omega_c = \arctan\left(\frac{L_s - L_r}{L_b}\right).$$

In conjunction with (A.5), the ellipsoid equation in the x-y-z system can be written as (A.6).

$$\frac{\left(x\cos\omega_c + z\sin\omega_c + \frac{2L_sL_r}{L_s+L_r}\sin\omega_c + \frac{\hat{L}_b(L_s-L_r)}{2(L_s+L_r)}\right)^2}{\left(\frac{ct}{2}\right)^2} + \frac{y^2}{\left(\frac{ct}{2}\right)^2 - \left(\frac{\hat{L}_b}{2}\right)^2} + \frac{\left(z\cos\omega_c - x\sin\omega_c + \frac{2L_sL_r}{L_s+L_r}\cos\omega_c\right)^2}{\left(\frac{ct}{2}\right)^2 - \left(\frac{\hat{L}_b}{2}\right)^2} \leq 1 \quad \text{(A.6)}$$

In the case that the signal is reflected by a single diffusing surface, all reflected points have to fulfil the condition $z = 0$, which leads to an ellipse on the x-y plane as:

$$\mathcal{W}_0(t): \left(1 - \frac{L_b^2}{c^2t^2}\right)x^2 + \left(\frac{L_b(L_s - L_r)\left(c^2t^2 - L_0^2\right)}{c^2t^2(L_s + L_r)}\right)x + y^2 - \frac{\left(c^2t^2 - L_0^2\right)^2}{(L_s + L_r)^2}\left(\frac{(L_s - L_r)^2}{4c^2t^2} + \frac{L_sL_r}{c^2t^2 - L_0^2}\right) \leq 0. \quad \text{(A.7)}$$

This ellipse defines the integration limits for x and y when calculating $\hat{P}_{\mathrm{opt},h}(t)$. Therefore, $\hat{P}_{\mathrm{opt},h}(t)$ can be calculated as:

$$\hat{P}_{\mathrm{opt},h}(t) = \iint_{\mathcal{W}_0(t)} \mathfrak{f}(x,y)\mathrm{d}x\mathrm{d}y.$$

Thus, the channel impulse response can be calculated as $\hbar(t) = \frac{\mathrm{d}\hat{P}_{\mathrm{opt},h}(t)}{\mathrm{d}t}$. For the convenience of calculating $\hbar(t)$, a polar coordinate system with a radius r and a polar angle θ is used. The polar coordinates can be calculated based on the following relationships:

$$x = r\cos\theta, \quad \text{(A.8)}$$

$$y = r\sin\theta. \quad \text{(A.9)}$$

By inserting (A.8) and (A.9) into (A.3), it gives:

$$\mathrm{d}G(r,\theta) = \frac{\rho(m+1)A_rL_sL_r}{2\pi^2}\mathfrak{f}(r,\theta)r\mathrm{d}r\mathrm{d}\theta,$$

where $\mathfrak{f}(r,\theta)$ can be found in (3). By inserting (A.8) and (A.9) into (A.7), it gives:

$$\mathcal{W}_0(t): \left(1 - \frac{L_b^2\cos^2\theta}{c^2t^2}\right)r^2 + \left(\frac{L_b(L_s - L_r)\left(c^2t^2 - L_0^2\right)\cos\theta}{c^2t^2(L_s + L_r)}\right)r - \frac{\left(c^2t^2 - L_0^2\right)^2}{(L_s + L_r)^2}\left(\frac{(L_s - L_r)^2}{4c^2t^2} + \frac{L_sL_r}{c^2t^2 - L_0^2}\right) \leq 0.$$

Thus, the channel impulse response can be decomposed into two one-dimensional integrals as:

$$\hbar(t) = \frac{\mathrm{d}}{\mathrm{d}t}\left(\frac{\rho(m+1)A_rL_sL_r}{2\pi^2}\int_0^{2\pi}\int_0^{\mathfrak{r}_\theta(t)}\mathfrak{f}(r,\theta)r\mathrm{d}r\mathrm{d}\theta\right),$$

where the value of the limit $\mathfrak{r}_\theta(t)$ can be calculated by evaluating the bound value of r in $\mathcal{W}_0(t)$. It is determined by making the inequality $\mathcal{W}_0(t)$ into an equality, and solving this equation with considering r as the unknown. Thus, this solution $\mathfrak{r}_\theta(t)$ can be concluded as (4). According to the Chain rule $\frac{\mathrm{d}}{\mathrm{d}t}\int_0^{g(t)} f(r)\mathrm{d}r = f(g(t))\frac{\mathrm{d}g(t)}{\mathrm{d}t}$, the CIR can be further simplified as (2).

Appendix B
Approximation in (18)

In this appendix, the approximation used in (18) is demonstrated, and the accuracy of the approximation with various parameters is evaluated. Firstly, the special case of (13) with

IEEE Proof

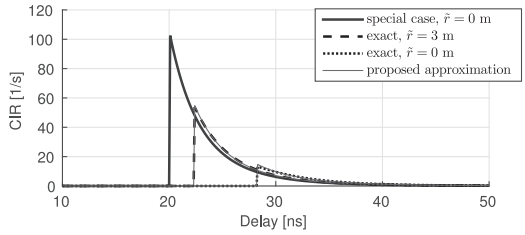

Fig. 18. An example of the comparison between the exact and approximated TFC CIR results with $\tilde{r}=0$, 3, 6 m.

$\tilde{r}=0$ m is considered. By making $\tilde{r}=0$, (13) can be rearranged as:

$$\begin{aligned}\mathrm{d}h^{\vec{a}_b}_{\mathrm{tfc},\tilde{r}=0}(t) &= \hbar^{[0,0,1],[0,0,1]}_{\{1,\mathrm{d}A,\rho_f,z_s,z_s,0,90^\circ\}}(t)\\ &= \frac{(m+1)\mathrm{d}A\rho_f z_s^{m+3}}{\pi(c/2)^{m+5}t^{m+6}},\end{aligned} \tag{B.1}$$

which is significantly simplified and in closed-form. It is worth noting that this is a special case of the result derived in [16]. An example of (B.1) is presented in Fig. 18. In this example, $\phi_{1/2}=60^\circ$ and the configuration of the remaining parameters are the same as those listed in Table I. Then, we calculate the CIR with $\tilde{r}=3$, 6 m using (13), which are also shown in Fig. 18. It can be observed that the shapes of the curves with different value of $\tilde{r}$ are similar. With the increase of $\tilde{r}$, the minimum delay of the response is longer due to the increased minimum transmission distance. In addition, the magnitude of the CIR is slightly increased compared to the special case of $\tilde{r}=0$ m. Therefore, we use a unit step function to control the minimum delay and a scaling factor to control the response magnitude in the approximated TFC CIR (18). The scaling factor $\mathcal{F}_{\mathrm{tfc}}$ only needs to vary with m and the ratio $\tilde{r}/z_s$ as the effects of the remaining parameters are preserved by (B.1). In Fig. 18, the approximated TFC CIR results are presented in addition to their corresponding exact results calculated using (13). It can be observed that (18) offers an accurate approximation to the exact TFC CIR expression (13).

Next, the accuracy of the approximation with various configurations is evaluated. The NMSE of the CIR approximation is calculated, which is defined as:

$$e_{\mathrm{nmse}} = \frac{\mathbb{E}_t\left[\left(\hat{h}(t)-h(t)\right)^2\right]}{\mathbb{E}_t\left[h^2(t)\right]}, \tag{B.2}$$

where $\hat{h}(t)$ denotes the approximated CIR result. Fig. 19 shows results of NMSE varies with $\tilde{r}/z_s$ and with $\phi_{1/2}$. It can be observed that with most of the configurations, the NMSE is negligible. With an increase of $\tilde{r}/z_s$ and a decrease of $\phi_{1/2}$, the resulting NMSE increases. In the case that $\phi_{1/2}$ is smaller than 30° and $\tilde{r}/z_s$ is greater than 2, the approximation becomes inaccurate. However, the magnitude of the CIR itself in this extreme case is significantly small. Consequently, these inaccurate components contribute little to the final TFCR calculation in (27). Therefore, this approximation error will not significantly affect the accuracy of the CIR calculation of the TFCR category.

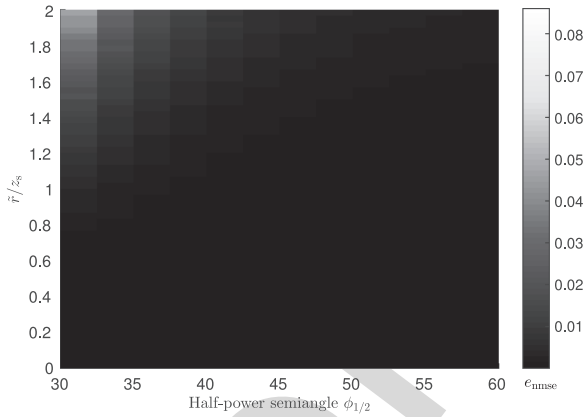

Fig. 19. NMSE of the approximation in (18) with various $\tilde{r}/z_s$ and $\phi_{1/2}$.

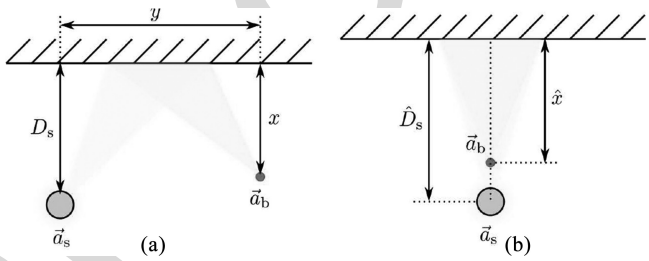

Fig. 20. (a) TWC channel geometry with $y\neq 0$ m. (b) Approximated TWC channel geometry with $y=0$ m, $\hat{D}_s$ and $\hat{x}$.

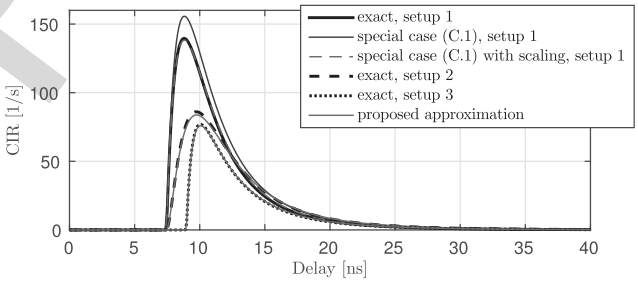

Fig. 21. An example of the comparison between the exact and approximated TWC CIR results. Setup 1: $D_s=1$ m, $x=1$ m, $y=1$ m, $\phi_{1/2}=60^\circ$. Setup 2: $D_s=1$ m, $x=1$ m, $y=1$ m, $\phi_{1/2}=40^\circ$. Setup 3: $D_s=2$ m, $x=0.5$ m, $y=1$ m, $\phi_{1/2}=60^\circ$. The results of the approximated curves are also shown in this figure. Setup 1 is used to demonstrate the approximation method.

APPENDIX C
APPROXIMATION IN (32)

In this appendix, the approximation used in (32) is demonstrated, and the accuracy of the approximation with various parameters is evaluated. Firstly, the spacial case of (28) with $y=0$ m is considered. By making $y=0$ m, (28) can be rearranged as:

$$\begin{aligned}&\mathrm{d}h^{\vec{a}_b}_{\mathrm{twc},y=0}(t,D_s,x) = \hbar^{[0,1,0],[0,1,0]}_{\{m,\mathrm{d}A,\rho_w,D_s,x,0,90^\circ\}}(t)\\ &= \frac{\rho_w D_s x\mathcal{B}\left(\frac{m+2}{2},\frac{m+2}{2}\right)2^m\mathfrak{r}^2_{\mathrm{twc}}(t)\mathrm{d}A\mathcal{U}\left(t-\frac{D_s+x}{c}\right)}{\frac{\pi^2 t}{m+1}\left(1+\frac{D_s^2}{\mathfrak{r}^2_{\mathrm{twc}}(t)}\right)^{\frac{m-1}{2}}\left(\frac{c^2t^2}{4}-\frac{(D_s^2-x^2)^2}{4c^2t^2}\right)^3},\end{aligned} \tag{C.1}$$

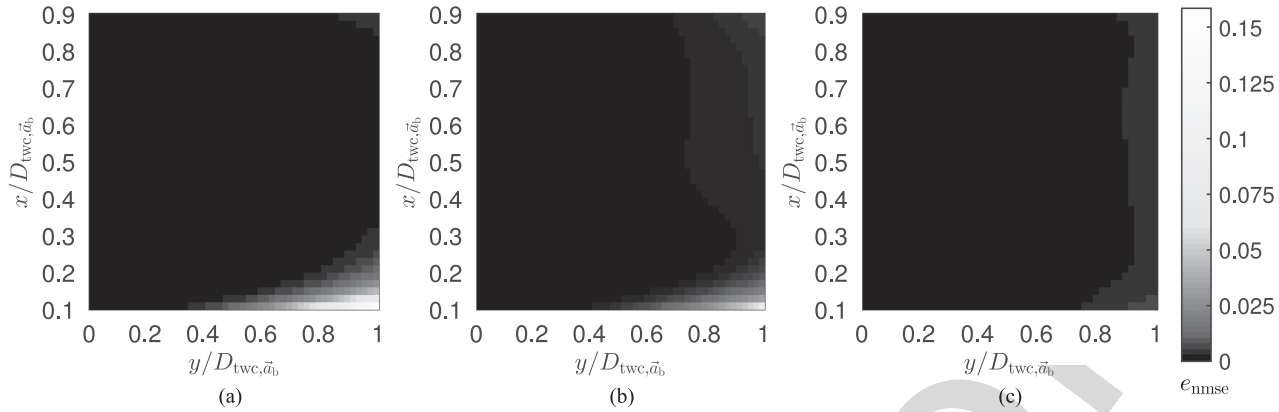

Fig. 22. NMSE of the approximation in (32) with various $y/D_{\mathrm{twc},\vec{a}_b}$ and $x/D_{\mathrm{twc},\vec{a}_b}$. (a) $\phi_{1/2} = 20°$. (b) $\phi_{1/2} = 40°$. (c) $\phi_{1/2} = 60°$.

where

$$\mathfrak{r}^2_{\mathrm{twc}}(t) = \frac{c^2t^2}{4} + \frac{\left(D_s^2 - x^2\right)^2}{4c^2t^2} - \frac{D_s^2 + x^2}{2}. \tag{C.2}$$

This special case expression (C.1) is significantly simplified and in closed form compared to the general case TWC CIR expression (28). Therefore, we use (C.1) as a base function to develop an expression to approximate (28). Considering a TWC channel in a general case with $y \neq 0$, the top view of the channel geometry is shown in Fig. 20(a). It is intuitive to find that the length of the shortest propagation path is $D_{\mathrm{twc},\vec{a}_b} = \sqrt{(D_s + x)^2 + y^2}$. Now we want to use the special case channel with $y = 0$ m to approximate the general case TWC channel as shown in Fig. 20(b). In order to achieve the correct minimum delay control, the minimum transmission distance in the approximated model should be the same as that in the original model, which means $D_{\mathrm{twc},\vec{a}_b} = \hat{D}_s + \hat{x}$ should be fulfilled. It has been found that by adjusting the values of $\hat{D}_s$ to $\hat{x}$, the curve shape of the function (C.1) can be manipulated to be similar to that of the corresponding exact TWC CIR (28). Due to the difference in the incident (radiant) angles to (from) the wall in the exact and approximated TWC channel, the magnitude of the approximated CIR is different from the exact result. Therefore, a scaling factor $\mathcal{F}_{\mathrm{twc}}$ is required. Thus, the approximated CIR can be written as:

$$\mathrm{d}h^{\vec{a}_b}_{\mathrm{twc}}(t) \approx \mathcal{F}_{\mathrm{twc}} \mathrm{d}h^{\vec{a}_b}_{\mathrm{twc},y=0}\left(t, \hat{D}_s, \hat{x}\right). \tag{C.3}$$

Next, we use an example to demonstrate the considered approximation. In this example, $D_s = 1$ m, $x = 1$ m, $y = 1$ m and $\phi_{1/2} = 60°$. The remaining parameters are the same as those listed in Table I. The CIR result calculated using (28) is shown in Fig. 21. In addition, the CIR result calculated using the base function (C.1) with $\hat{D}_s = 1.118$ m and $\hat{x} = 1.118$ m is presented. It can be observed that the two curves are similar in shape but with a slight difference in magnitude as shown in Fig. 21. By multiplying the CIR result calculated using (C.1) with a factor of 0.8882, the scaled result shows a very close approximation to the exact TWC CIR curve. This example shows the possibility of using the proposed expression (C.3) to achieve accurate approximation. Appropriate functions for the calculation of $\hat{D}_s$, $\hat{x}$ and $\mathcal{F}_{\mathrm{twc}}$ are important for the accuracy of the approximation. By using curve fitting tools, expressions (34), (35) and (36) have been found to provide acceptable accuracy. In Fig. 21, another two examples calculated using (32) are demonstrated. Both approximated results are close to the corresponding exact TWC CIR results calculated using (28).

Then, the accuracy of the approximation using (32) with various configurations is evaluated. The NMSE for various configurations defined by (B.2) in Appendix B is calculated. The results of NMSE varies with $y/D_{\mathrm{twc},\vec{a}_b}$ and $x/D_{\mathrm{twc},\vec{a}_b}$ in the case of $\phi_{1/2} = 20°, 40°, 60°$ are shown in Fig. 22. It shows that with majority of the configurations, the NMSE level is negligible. It is noted that in the case of $y/D_{\mathrm{twc},\vec{a}_b}$ is significant and $x/D_{\mathrm{twc},\vec{a}_b}$ is very close to zero, the NMSE starts to increase, especially when $\phi_{1/2}$ is small.

REFERENCES

[1] S. Dimitrov and H. Haas, *Principles of LED Light Communications: Towards Networked Li-Fi*. Cambridge , U.K.: Cambridge Univ. Press, 2015.
[2] D. Tsonev *et al.*, "A 3-Gb/s single-LED OFDM-based wireless VLC link using a gallium nitride μLED," *IEEE Photon. Technol. Lett.*, vol. 26, no. 7, pp. 637–640, Apr. 2014.
[3] A. M. Khalid, G. Cossu, R. Corsini, P. Choudhury, and E. Ciaramella, "1-Gb/s transmission over a phosphorescent white LED by using rate-adaptive discrete multitone modulation," *IEEE Photon. J.*, vol. 4, no. 5, pp. 1465–1473, Oct. 2012.
[4] J. Barry, J. Kahn, W. Krause, E. Lee, and D. Messerschmitt, "Simulation of multipath impulse response for indoor wireless optical channels," *IEEE J. Sel. Areas Commun.*, vol. 11, no. 3, pp. 367–379, Apr. 1993.
[5] G. R. Maccartney, T. S. Rappaport, S. Sun, and S. Deng, "Indoor office wideband millimeter-wave propagation measurements and channel models at 28 and 73 GHz for ultra-dense 5G wireless networks," *IEEE Access*, vol. 3, pp. 2388–2424, Oct. 2015.
[6] T. Komine and M. Nakagawa, "Fundamental analysis for visible-light communication system using LED lights," *IEEE Trans. Consum. Electron.*, vol. 50, no. 1, pp. 100–107, Feb. 2004.
[7] J. Grubor, S. Randel, K. Langer, and J. W. Walewski, "Broadband information broadcasting using LED-Based interior lighting," *IEEE J. Lightw. Technol.*, vol. 26, no. 24, pp. 3883–3892, Dec. 2008.
[8] F. J. Lopez-Hermandez and M. J. Betancor, "DUSTIN: Algorithm for calculation of impulse response on IR wireless indoor channels," *Electron. Lett.*, vol. 33, no. 21, pp. 1804–1806, Oct. 1997.
[9] F. Lopez-Hernandez, R. Perez-Jimenez, and A. Santamaria, "Ray-tracing algorithms for fast calculation of the impulse response on diffuse IR-wireless indoor channels," *Opt. Eng.*, vol. 39, no. 10, pp. 2775–2780, Oct. 2000.

IEEE PROOF

[10] V. Jungnickel, V. Pohl, S. Nonnig, and C. von Helmolt, "A physical model of the wireless infrared communication channel," *IEEE J. Sel. Areas Commun.*, vol. 20, no. 3, pp. 631–640, Apr. 2002.
[11] K. Lee, H. Park, and J. Barry, "Indoor channel characteristics for visible light communications," *IEEE Commun. Lett.*, vol. 15, no. 2, pp. 217–219, Feb. 2011.
[12] P. Chvojka, S. Zvanovec, P. A. Haigh, and Z. Ghassemlooy, "Channel characteristics of visible light communications within dynamic indoor environment," *J. Lightw. Technol.*, vol. 33, no. 9, pp. 1719–1725, May 2015.
[13] F. Miramirkhani and M. Uysal, "Channel modeling and characterization for visible light communications," *IEEE J. Photon.*, vol. 7, no. 6, pp. 1–16, Dec. 2015.
[14] L. Zeng *et al.*, "High data rate multiple input multiple output (MIMO) optical wireless communications using white LED lighting," *IEEE J. Sel. Areas Commun.*, vol. 27, no. 9, pp. 1654–1662, Dec. 2009.
[15] Y. Wang, S. Videv, and H. Haas, "Dynamic load balancing with handover in hybrid Li-Fi and Wi-Fi networks," in *Proc. Symp. Pers. Indoor Mobile Radio Commun.*, Sep. 2014, pp. 548–552.
[16] J. B. Carruthers and J. M. Kahn, "Modeling of nondirected wireless infrared channels," *IEEE Trans. Commun.*, vol. 45, no. 10, pp. 1260–1268, Oct. 1997.
[17] C. Chen, D. Basnayaka, and H. Haas, "Non-line-of-sight channel impulse response characterisation in visible light communications," in *Proc. IEEE Int. Conf. Commun.*, Kuala Lumpur, Malaysia, May 2016, pp. 1–6.
[18] J. M. Kahn, W. J. Krause, and J. B. Carruthers, "Experimental characterization of non-directed indoor infrared channels," *IEEE Trans. Commun.*, vol. 43, no. 234, pp. 1613–1623, Feb.–Apr. 1995.
[19] *Lighting of Indoor Work Places*, European Standard EN 12464-1, Jan. 2009.
[20] "Kingbali high backlight reflective paper." [Online]. Available: http://www.kingbali.com
[21] F. R. Gfeller and U. Bapst, "Wireless in-house data communication via diffuse infrared radiation," *Proc. IEEE*, vol. 67, no. 11, pp. 1474–1486, Nov. 1979.
[22] F. J. Lopez-Hernandez, R. Perez-Jimenez, and A. Santamara, "Ray-tracing algorithms for fast calculation of the channel impulse response on diffuse IR wireless indoor channels," *Opt. Eng.*, vol. 39, no. 10, pp. 2775–2780, 2000.
[23] C. Chen, D. A. Basnayaka, and H. Haas, "Downlink performance of optical attocell networks," *J. Lightw. Technol.*, vol. 34, no. 1, pp. 137–156, Jan. 2016.

Cheng Chen received the B.Eng. degree in electronic and electrical engineering from the University of Strathclyde, Glasgow, U.K., in 2011, the M.Sc. degree in communications and signal processing from the Imperial College, London, U.K., in 2012, and the Ph.D. degree in electrical engineering from the University of Edinburgh, Edinburgh, U.K., in 2017. He is currently employed as a Research Associate with the Li-Fi Research and Development Centre, the University of Edinburgh and is working in the field of visible light communications.

Dushyantha A. Basnayaka (S'11–M'12) received the B.Sc. Eng. degree (Hons.) in 2006, and the Ph.D. degree in electrical and electronics engineering, in 2012. He is currently with the Institute for Digital Communications, the University of Edinburgh, Edinburgh, U.K. His current research interests include multiple-input multiple-output, index modulation, the physical layer aspects of internet-of-things (IoT), coordinated multipoint systems (CoMP), and visible light communication systems. He holds two patents (one granted and one pending) in CoMP, and IoT. He was a recipient of the University of Canterbury International Doctoral Scholarship from 2009 to 2012, and the Best Paper Award at the 2015 IEEE Vehicular Technology Conference.

Xiping Wu (S'11–M'14) received the B.Sc. degree from Southeast University, Nanjing, China, in 2008, the M.Sc. degree (Hons.) and the Ph.D. degree from the University of Edinburgh, Edinburgh, U.K., in 2011 and 2015, respectively. From 2011 to 2014, he was a Marie-Curie Early-Stage Researcher, funded by the European Unions Seventh Framework Program (FP7) Project GREENET. From 2013 to 2014, he was on secondment to the Department of Electrical and Information Engineering, University of LAquila, LAquila, Italy. He is currently a Research Associate with the Institute for Digital Communications with the University of Edinburgh, funded by the British Engineering and Physical Sciences Research Council Project TOUCAN. His main research interests include wireless communication theory, visible light communications, and wireless network management. He was a recipient of the Scotland Saltire Scholarship by the Scottish Government in 2010.

Harald Haas (S'98–AM'00–M'03–SM'17) received the Ph.D. degree from the University of Edinburgh, Edinburgh, U.K., in 2001. He currently holds the Chair of Mobile Communications, the University of Edinburgh, and is the initiator, cofounder, and Chief Scientific Officer with pureLiFi Ltd., as well as the Director of the LiFi Research and Development Center, the University of Edinburgh. His main research interests include optical wireless communications, hybrid optical wireless and RF communications, spatial modulation, and interference coordination in wireless networks. He first introduced and coined spatial modulation and LiFi. LiFi was listed among the 50 best inventions in TIME Magazine 2011. He was an invited speaker at TED Global 2011, and his talk: Wireless Data from Every Light Bulb has been watched online more than 2.4 million times. He gave a second TED Global lecture in 2015 on the use of solar cells as LiFi data detectors and energy harvesters. This has been viewed online more than 1.8 million times. He authored or coauthored more than 400 conference and journal papers including a paper in Science. He coauthors a book entitled: *Principles of LED Light Communications Towards Networked Li-Fi* (Cambridge University Press, 2015). He is the Editor of the IEEE TRANSACTIONS ON COMMUNICATIONS and IEEE JOURNAL OF LIGHTWAVE TECHNOLOGIES. He was corecipient of recent best paper awards at VTC-Fall, 2013, VTC-Spring 2015, ICC 2016, and ICC 2017. He was corecipient of the EURASIP Best Paper Award for the *Journal on Wireless Communications and Networking* in 2015, and corecipient of the Jack Neubauer Memorial Award of the IEEE Vehicular Technology Society. In 2012 and 2017, he was the recipient of the prestigious Established Career Fellowship from the EPSRC (Engineering and Physical Sciences Research Council) within Information and Communications Technology in U.K. In 2014, he was selected by EPSRC as one of ten RISE (Recognising Inspirational Scientists and Engineers) Leaders in U.K. In 2016, he received the outstanding achievement award from the International Solid State Lighting Alliance. He was elected a Fellow of the Royal Society of Edinburgh in 2017.

IEEE Proof

GENERAL INSTRUCTIONS

- Authors: When accessing and uploading your corrections at the Author Gateway, please note we cannot accept new source files as corrections for your paper. Do not send new Latex, Word, or PDF files, as we cannot simply "overwrite" your paper. Please submit your corrections as an annotated PDF or as clearly written list of corrections, with location in paper, using line numbers provided on your proof. You can also upload revised graphics to the Gateway.
- Authors: Please note that once you click "approve with no changes," the proofing process is now complete and your paper will be sent for final publication and printing. Once your paper is posted on Xplore, it is considered final and the article of record. No further changes will be allowed at this point so please ensure scrutiny of your final proof.
- Authors: Unless invited or otherwise informed, overlength page charges of $260 per page are mandatory for each page in excess of seven printed pages and are required for publication. If you have any questions regarding overlength page charges, need an invoice, or have any other billing questions, please contact reprints@ieee.org as they handle these billing requests.

QUERIES

Q1. Author: There was a discrepancy between source file and pdf. We have followed the source file.

Q2. Author: Please provide the year for Ref. [20].

IEEE Proof